



저작자표시-비영리-변경금지 2.0 대한민국

이용자는 아래의 조건을 따르는 경우에 한하여 자유롭게

- 이 저작물을 복제, 배포, 전송, 전시, 공연 및 방송할 수 있습니다.

다음과 같은 조건을 따라야 합니다:



저작자표시. 귀하는 원저작자를 표시하여야 합니다.



비영리. 귀하는 이 저작물을 영리 목적으로 이용할 수 없습니다.



변경금지. 귀하는 이 저작물을 개작, 변형 또는 가공할 수 없습니다.

- 귀하는, 이 저작물의 재이용이나 배포의 경우, 이 저작물에 적용된 이용허락조건을 명확하게 나타내어야 합니다.
- 저작권자로부터 별도의 허가를 받으면 이러한 조건들은 적용되지 않습니다.

저작권법에 따른 이용자의 권리는 위의 내용에 의하여 영향을 받지 않습니다.

이것은 [이용허락규약\(Legal Code\)](#)을 이해하기 쉽게 요약한 것입니다.

[Disclaimer](#)

공학박사 학위논문

**Design and Analysis of Organic
Molecules for Lithium Metal and
Aluminum Complex Ion Batteries**

리튬 금속 및 알루미늄 복합 이온 전지를 위한
유기 분자 설계 및 분석

2020년 8월

서울대학교 대학원
화학생물공학부

유 동 주

Abstract

Design and Analysis of Organic Molecules for Lithium Metal and Aluminum Complex Ion Batteries

Dong-Joo, Yoo

School of Chemical and Biological Engineering

The Graduate School

Seoul National University

Lithium-ion batteries (LIBs), composed of lithium-containing oxide cathodes and graphite anodes, have powered the most mobile devices due to their high power and energy density compared to other battery types. Since the advent of LIBs, there is growing demand for even higher energy density to power mobile devices with increased power consumption and to extend the driving mileage of electric vehicles (EVs). More importantly, as the commercialization of EVs is rapidly accelerated in recent years, the development of LIBs with advanced performance is the most urgent project to enable the longer driving mileage of EVs. Although battery suppliers have endeavored to increase the energy density of LIBs for past decades, the practical energy density of LIBs is reaching the theoretical limit based on the active materials.

A dramatic increase in the energy density requires new redox chemistries beyond the conventional ‘intercalation’ mechanism. The redox behaviors caused by new chemistries are distinct from those in the conventional host materials, leading to uncontrolled side reactions and short lifetime. The primary factors responsible for the low reversibility are instabilities during the redox reaction of active materials and uncontrolled reactions at the electrode/electrolyte interface. This implies that the novel

active materials and electrolyte solutions should be developed to enable the realization of post-LIBs. In this thesis, I cover the development and analysis of novel organic materials for Li metal batteries and Al batteries.

In *Chapter 2*, I revealed the role of toluene as a co-solvent of carbonate-based electrolytes for Li metal anodes. The electron donating nature of the methyl group of toluene shifts the reduction of toluene prior to that of commonly used carbonate solvents, resulting in a more uniform and rigid SEI layer. Moreover, the polymerization process of toluene induces the decomposition of the bis(fluorosulfonyl)imide (FSI) anion in LiFSI salt to yield uniform distribution of lithium fluoride (LiF), and thus lowers an onset salt concentration in realizing the so-called ‘high concentration effect’ to 3 molar concentration, instead of 5 molar concentration as in typical electrolyte cases. This investigation reveals the usefulness of aromatic compounds in improving the stability of the SEI layer in lithium metal anodes, particularly by tuning the electron density of the benzene ring.

In *Chapter 3*, I discovered a fluorinated aromatic compound, namely 1,2-difluorobenzene, for use as a diluent solvent in the electrolyte to realize the “high-concentration effect”. The low lowest unoccupied molecular orbital (LUMO) level, weak binding affinity for lithium ions, and high fluorine-donating power of 1,2-difluorobenzene jointly give rise to the high-concentration effect at a bulk salt concentration near 2 M while modifying the composition of the solid-electrolyte-interphase (SEI) layer to be rich in lithium fluoride (LiF). The employment of triple salts to prevent corrosion of the aluminum current collector further improves cycling performance. This study offers a design principle on how to achieve the local high-concentration effect at reasonably low bulk concentrations of salts.

In *Chapter 4*, I demonstrated a strategy for designing active materials for rechargeable Al batteries. This strategy entails the use of redox-active triangular phenanthrenequinone-based macrocycles which form layered superstructures resulting in the reversible insertion and extraction of cationic Al complex. This architecture exhibits an outstanding electrochemical performance with a reversible capacity of 110 mAh g⁻¹ along with a superior cyclability of up to 5000 cycles. Furthermore, electrodes composed of these macrocycles blended with graphite flakes results in higher specific

capacity, electronic conductivity, and areal loading. These findings constitute a major advance in the design of rechargeable Al batteries and represent a good starting point for addressing affordable large-scale energy storage.

In *Chapter 5*, I not only demonstrate the excellent rate and cycling performance of phenanthrenequinone (PQ), but also elucidate the origin of this extraordinary performance. Density functional theory (DFT) calculations and experimental analyses jointly revealed that the long-term cyclability of PQ arises from PQ-AlCl₂ complexation, which lessens the effective charge of PQ to mitigate its dissolution into the electrolyte. Moreover, the formation of AlCl₂⁺ without a separate desolvation step allows fast charge transfer, accelerating the AlCl₂⁺ insertion process. This work unveils the importance of aluminum coordination chemistry in determining the key electrochemical properties of aluminum batteries and forms the basis of a new research direction for the development of battery systems based on complex ions.

Keywords: Organic materials, Post lithium-ion battery, Electrolytes, Lithium metal batteries, Aluminum batteries

Student number: 2018-38876

Contents

Chapter 1. Introduction.....	1
1.1 Toward Next-Generation Rechargeable Batteries	1
1.2 Issues in Development for Lithium Metal Batteries	2
1.3 Issues in Development for Aluminum Batteries	4
1.4 Objectives	5
Chapter 2. Tuning the Reductive Polymerization of Aromatic Solvent for Stable Lithium Metal Batteries.....	8
2.1 Introduction	8
2.2 Results and discussion	11
2.3 Conclusion	23
2.4 Experimental	24
2.4.1 Electrolyte preparation	24
2.4.2 Electrochemical measurements	24
2.4.3 Characterization	24
2.4.4 Density Functional Theory (DFT) calculations	25
Chapter 3. Fluorinated Aromatic Diluent in Localized High-Concentration Electrolytes.....	26
3.1 Introduction	26
3.2 Results and discussion	29
3.3 Conclusion	40
3.4 Experimental	41
3.4.1 Electrolyte preparation	41
3.4.2 Electrochemical measurements	41
3.4.3 Characterization	42

3.4.4 Density Functional Theory (DFT) calculations	42
Chapter 4. Triangular Phenanthrenequinone-based Macrocycle for Aluminum Batteries.....	43
4.1 Introduction	43
4.2 Results and discussion	46
4.3 Conclusion	60
4.4 Experimental	61
4.4.1 Materials preparation and characterization	61
4.4.2 <i>ex-situ</i> Characterization of PQ- Δ electrodes	61
4.4.3 Preparation of ALB electrodes and measurements	62
Chapter 5. Elucidating the Extraordinary Behavior of Phenanthrenequinone in Aluminum Batteries	64
5.1 Introduction	64
5.2 Results and discussion	65
5.3 Conclusion	79
5.4 Experimental	80
5.4.1 Synthesis of materials	80
5.4.2 Electrochemical measurements	80
5.4.3 Characterization	81
5.4.4 Density Functional Theory (DFT) calculations	81
Chapter 6. Summary and Conclusions	83
Bibliography	85
국문초록	94

List of Tables

Table 3-1 LUMO levels, binding energies, and cyclability of cosolvents used in this study. Cyclability refers to the cycle number when the CE of a Li-Cu asymmetric cell drops below 90% when tested with a capacity of 0.5 mAh cm^{-2} at 0.5 mA cm^{-2}30

List of Figures

Fig. 1-1 Ragon plot of various battery types and energy storage diagram of commonly used LIBs.	1
Fig. 1-2 (a) Energy density diagram and (b) the main problems of Li metal batteries. .	3
Fig. 1-3 Capacities and reductive potential for various metal anodes.	4
Fig. 2-1 (a) Molecular structures of benzene, toluene, and trifluorotoluene with electron donating/withdrawing character denoted. (b) Linear sweep voltammetry profiles of three EC/DEC electrolytes containing Ben, Tol, and tfTol in addition to the EC/DEC standard case. (c) Cycling performance of the electrolytes in (b) under the Li-Cu cell configuration when measured at 0.5 mA cm^{-2} with 0.5 mAh cm^{-2}	11
Fig. 2-2 SEM images of deposited Li on Cu foil with different electrolyte solvents and current densities with 0.5 mAh cm^{-2} . 1 M LiTFSI in (a) EC/DEC or (b) EC/DEC/Tol when measured at 0.2 mA cm^{-2} . 1 M LiTFSI in (c) EC/DEC or (d) EC/DEC/Tol when measured at 0.5 mA cm^{-2}	13
Fig. 2-3 (a) Polymerization scheme of toluene. Energy diagrams along (b) initiation step and (c) propagation step. The black, white, and red balls represent carbon atoms, hydrogen atoms, and hydrogen radicals, respectively.	15
Fig. 2-4 XPS spectra of 1 M LiTFSI in EC/DEC/Tol in (a) C 1s and (b) F 1s branches. XPS spectra of 1 M LiTFSI in EC/DEC in (c) C 1s and (d) F 1s branches. The analyses were performed after one cycle at 0.5 mA cm^{-2} with 0.5 mAh cm^{-2}	16
Fig. 2-5 3-D AFM scanning images of the SEI layers formed on Cu foil when 1 M LiTFSI in (a) EC/DEC/Tol and (b) EC/DEC are used as electrolytes. The characterization was performed after discharging from OCV to 0 V at 0.01 mA cm^{-2} . SEM and EDX images for the same two electrodes.	17
Fig. 2-6 Top-view and cross-sectional SEM images of the SEI layer formed in 1 M LiTFSI in (a, b) EC/DEC/Tol or (c, d) EC/DEC.	18
Fig. 2-7 Cycling performance of Li-Cu asymmetric cells with different salt concentrations when measured at 0.5 mA cm^{-2} with 0.5 mAh cm^{-2} : (a) 3 M LiFSI; (b)	

5 M LiFSI. SEM images of deposited Li for both solvent compositions with (c, e) 3 M LiFSI and (d, f) 5 M LiFSI.	19
Fig. 2-8 Cross-sectional SEM images of deposited Li on Cu foil with different electrolytes and current densities when areal capacity is fixed at 0.5 mAh cm ⁻² . 1 M LiTFSI in (a) EC/DEC and (b) EC/DEC/Tol when measured at 0.2 mA cm ⁻² . 3 M LiFSI in (c) EC/DEC and (d) EC/DEC/Tol when measured at 0.5 mA cm ⁻²	21
Fig. 2-9 (a) Cycling performance of NCM523-Li full-cells with 3 M LiFSI in EC/DEC and EC/DEC/Tol. (b-c) Corresponding voltage profiles at different cycle numbers. The mass loading of the active material in the cathode is 9 mg cm ⁻² , and the thickness of the Li layer in the anode is 20 μm.	22
Fig. 3-1 (a) LUMO energy levels of DMC, BTFE, Ben, fBen, and 1,2-dfBen. (b) SEM image of Li metal after immersion in 1,2-dfBen for 1 day and its EDS mapping images with respect to carbon and fluorine. (Inset) Digital photograph of the same Li metal foil.	29
Fig. 3-2 XPS spectra of Li metal in (a) C 1s, (b) F 1s and (c) Li 1s branches after immersion in 1,2-dfBen for 1 day.	30
Fig. 3-3 Relative free energies of 1,2-dfBen and 1,3-dfBen along the reaction coordinate.	31
Fig. 3-4 (a) Binding energies of DMC, BTFE, Ben, fBen, and 1,2-dfBen with a Li ion. (b) Raman spectra of DMC, 2 M-DMC, 5.5 M-DMC, 2 M-DMC/BTFE, and 2 M-DMC/1,2-dfBen. (c) Schematic illustration of the mechanism of SEI layer formation of the conventional electrolyte and current LHCE.	32
Fig. 3-5 Cycling performance of Li-Cu asymmetric cells with different electrolytes with a capacity of 0.5 mAh cm ⁻² at (a) 0.5 mA cm ⁻² and (b) various current densities of 0.5, 1, 2, 5, and 10 mA cm ⁻² . SEM images of plated Li with (c) 5.5 M-DMC, (d) 2 M-DMC/BTFE, (e) 2 M-DMC/1,2-dfBen, and (f) triple-DMC/1,2-dfBen.	35
Fig. 3-6 XPS spectra of the SEI layers in the (a) C 1s and (b) F 1s branches in the presence of different electrolytes. The analyses were performed after three cycles of Li plating and stripping with a capacity of 0.5 mAh cm ⁻² at 0.5 mA cm ⁻²	36

Fig. 3-7 Cyclic voltammetry profiles of NCM523 cathodes at a scan rate of 1 mV s^{-1} with (a) 1 M LiPF_6 in EC/DEC, (b) 2 M-DMC/BTFE, (c) 2 M-DMC/1,2-dfBen, and (d) triple-DMC/1,2-dfBen.	38
Fig. 3-8 XPS spectra of the NCM523 cathodes in the (a) C 1s and (b) F 1s branches after 15 cycles when different electrolytes are used.	39
Fig. 3-9 (a) Cycling performance and (b) coulombic efficiencies of NCM523-Li full cells with different electrolytes. The mass loading of the active material in the cathode is 17 mg cm^{-2} , and the thickness of the Li foil in the anode is $40 \text{ }\mu\text{m}$	39
Fig. 4-1 Series of phenanthrenequinone (PQ) derivatives for rechargeable aluminium batteries (ALBs). (a) Structural formulae of three phenanthrenequinone compounds—the phenanthrenequinone monomer (PQ-Ref), the linear phenanthrenequinone trimer (PQ-Lin), and the phenanthrenequinone triangle (PQ- Δ). (b) Electrochemical redox chemistry of PQ- Δ (blue) and its schematic representation. Upon discharging, the macrocycle is reduced to its semiquinone state (PQ- $\Delta^{3\cdot-}$, purple), followed by interacting with the cationic chloroaluminates (AlCl_2^+ , yellow), which were generated by the asymmetric cleavage of dialuminium hexachloride, resulting in the formation of the tetracoordinate complex, (PQ- $\Delta^{3\cdot-}$) $\cdot 3\text{AlCl}_2$	45
Fig. 4-2 Synthesis of 3,6-dibromophenanthrenequinone and phenanthrenequinone triangle (PQ- Δ).	46
Fig. 4-3 Synthesis of PQ-Lin through Suzuki coupling.	46
Fig. 4-4 (a) TGA Curve and (b) FT-IR spectrm of PQ- Δ	47
Fig. 4-5 Powder X-ray diffraction results of (a) PQ-Ref, (b) PQ-Lin, and (c) PQ- Δ	48
Fig. 4-6 Cyclic voltammetry (CV) of pyrolytic graphite-based current collector at a) 0.7–1.75 V and b) 0.7–2.0 V voltage range.	48
Fig. 4-7 Electrochemical measurements of PQ derivatives. All of the electrochemical measurements were performed in the voltage range of 0.8–1.75 V vs Al/Al^{3+} . Compound colour code: PQ-Ref (Red), PQ-Lin (green), and PQ- Δ (blue). (a) Cyclic voltammetry of each of the PQ derivatives at a scan rate of 5 mV s^{-1} . (b) Comparison of the galvanostatic voltage profiles, and (c) cycling performances of PQ derivatives at a current rate of 0.2 A g^{-1} ($= 2\text{C}$). (d) Rate capability measurement of PQ- Δ . The initial	

30 cycles were measured at 1C and the current rate was increased every 20 cycles up to 100C. (e) Extended cycling test of PQ-Δ at a current rate of 2 A g ⁻¹ (= 20C). The Coulombic efficiency is defined on the right axis.	49
Fig. 4-8 CV results of (a) PQ-Ref, (b) PQ-Lin, and (c) PQ-Δ up to 200 cycles at 10 mV s ⁻¹ scan rate.	50
Fig. 4-9 <i>Ex-situ</i> characterisation of PQ-Δ. (a) Galvanostatic voltage profile of PQ-Δ and its schematic illustration for each <i>ex-situ</i> state. (b-d) Transmission electron microscopic (TEM) images of <i>ex-situ</i> electrodes and corresponding (inset) powder X-ray diffraction (PXRD) traces. (e) Energy-dispersive X-ray spectroscopy of the discharged state sample—carbon (red), oxygen (orange), aluminium (yellow), and chlorine (green).	52
Fig. 4-10 ToF-SIMS spectra of the discharged PQ-Δ electrode.	53
Fig. 4-11 XPS Spectra of pristine, discharged, and charged PQ-Δ electrodes in the regions of (a) O 1s and (b) Al 2p.....	54
Fig. 4-12 Voltage versus differential capacity plot of (a) graphite flake and (b) PQ-Δ-HY.	54
Fig. 4-13 Fabrication of the graphite flake-blended phenanthrenequinone triangle hybrid (PQ-Δ-HY) and its electrochemical performance. Equal weight (1:1 w/w) of PQ-Δ and graphite flakes were used to fabricate the PQ-Δ-HY. (a-b) SEM and TEM images which characterise the microstructures. (c) Galvanostatic voltage profile of PQ-Δ-HY and its electrochemical redox schematic. Specific energy contributed from PQ-Δ and graphite flakes are represented in blue and grey colour, respectively. (d) Cycling performance of PQ-Δ-HY at the current rate of 0.2 A g ⁻¹ (= 2C). (e) Rate capability measurement of PQ-Δ-HY.....	55
Fig. 4-14 Mechanical stability and electrochemical performance of the hybrid electrode. (a-b) SEM images and digital photographs (insets) of PQ-Δ and PQ-Δ-HY electrodes at their pristine states. The areal loadings of the active materials in a and b are 2 and 9 mg cm ⁻² , respectively. The electrode compositions in a and b are PQ-Δ: Denka black: PVDF = 4: 5: 1 and PQ-Δ-HY: graphite: Denka black: PVDF = 4: 4: 1, respectively. (c) Galvanostatic voltage profiles and d, rate capability measurement of PQ-Δ-HY electrodes with different mass loadings of 2 and 9 mg cm ⁻² at 0.1 A g ⁻¹ .	

(e) Cycling performance of the same electrodes at a current rate of 0.2 A g ⁻¹ (=2C).	58
Fig. 5-1 (a) Molecular structure of PQ. SEM images of (b) physical mixture of AC and PQ and (c) AC with melt-infused PQ. (d) Adsorption-desorption isotherms of pristine AC and AC(PQ), and (e) their XRD patterns. (f) FT-IR spectra of PQ, AC, and AC(PQ).	66
Fig. 5-2 (a) XRD patterns of PQ. Cycling performance of PQ with (b) 1M LiPF ₆ in EC/DEC and (c) (EMImCl) ₂ (AlCl ₃) ₃ at a current density of 100 mA g ⁻¹ , together with their voltage profiles (insets).	67
Fig. 5-3 (a) Redox reaction mechanism of PQ. CV profiles of AC(PQ) with 1M LiPF ₆ in EC/DEC in the voltage range of 1.7–3.3 V at a scan rate of (b) 0.1 mV s ⁻¹ and (c) 5 mV s ⁻¹ . (d) DFT calculations to present two reaction paths for binding with two Li ⁺ ions. (e) Binding energies of the Li ion for the different coordination states. (f) Cycling performance of AC(PQ) at a current density of 100 mA g ⁻¹ and (inset) CV profiles after a different number of cycles at a scan rate of 5 mV s ⁻¹	68
Fig. 5-4 (a) Cycling performance of bare AC with 1M LiPF ₆ in EC/DEC and (EMImCl) ₂ (AlCl ₃) ₃ . Their voltage profiles after a different number of cycles with (b) 1M LiPF ₆ in EC/DEC and (c) (EMImCl) ₂ (AlCl ₃) ₃	70
Fig. 5-5 CV profiles after a different number of cycles at a scan rate of 5 mV s ⁻¹ with (a) 1M LiPF ₆ in EC/DEC, (b) 1M LiTFSI in Pyr14TFSI, and (c) (EMImCl) ₂ (AlCl ₃) ₃ . (d) Optimized structures and atomic charges of PQ-ILi and PQ-AlCl ₂ . (e) Cycling performance of AC(PQ) with 1M LiPF ₆ in EC/DEC and 1M LiTFSI in Pyr14TFSI. (f) Rate capabilities of AC(PQ) with 1M LiTFSI in Pyr14TFSI and (EMImCl) ₂ (AlCl ₃) ₃ . (g) Extended cycling test of AC(PQ) with (EMImCl) ₂ (AlCl ₃) ₃ . The measurements of cells containing Li and Al electrolytes were performed in the voltage ranges of 2.5–3.3 V vs. Li/Li ⁺ and 0.5–1.7 V vs. Al/Al ³⁺ , respectively.	71
Fig. 5-6 ESR spectra of the pristine and discharged AC(PQ) with (EMImCl) ₂ (AlCl ₃) ₃	72
Fig. 5-7 Voltage profiles of discharge and charge after 6 hrs of rest at the discharged state: (a) 1M LiPF ₆ in EC/DEC, (b) 1M LiTFSI in Pyr14TFSI, and (c) (EMImCl) ₂ (AlCl ₃) ₃ . (Insets) Photographs of the separators after the dissolution test.	

.....	73
Fig. 5-8 Dependence of the CV on the scan rate with different electrolytes. (a) Potential polarization between the cathodic and anodic peaks in the CV curves. (b) $\log v$ - $\log I$ plots to extract b -values based on the relation $I_p = av^b$. (c) Binding energies for desolvation in different electrolytes.	74
Fig. 5-9 Voltage profiles of symmetric cells with different electrolytes at various current densities.	75
Fig. 5-10 Temperature-dependent Nyquist plots of AC(PQ) with (a) 1M LiPF ₆ in EC/DEC, (b) 1M LiTFSI in Pyr14TFSI, and (c) (EMImCl) ₂ (AlCl ₃) ₃ . Arrhenius plots of the resistance of (d) the electrolyte ($R_{\text{electrolyte}}$) and (e) charge transfer (R_{ct}). (f) Comparison of the resistance contributions at 25 °C.	77

Chapter 1. Introduction

1.1 Toward Next-Generation Rechargeable Batteries

Since the 1990s, lithium-ion batteries (LIBs), composed of lithium-containing oxide cathodes and graphite anodes, have powered the most mobile devices due to their high power and energy density compared to other battery types such as Ni-MH, alkaline or lead-acid battery (Fig. 1-1).¹ Since the advent of LIBs, there is growing demand for even higher energy density to power mobile devices with increased power consumption and to extend the driving mileage of electric vehicles (EVs). More importantly, as the commercialization of EVs is rapidly accelerated in recent years, the development of LIBs with advanced performance is the most urgent project to enable the longer driving mileage of EVs. Although battery suppliers have endeavored to increase the energy density of LIBs for past decades, the practical energy density of LIBs is reaching the theoretical limit based on the active materials.²

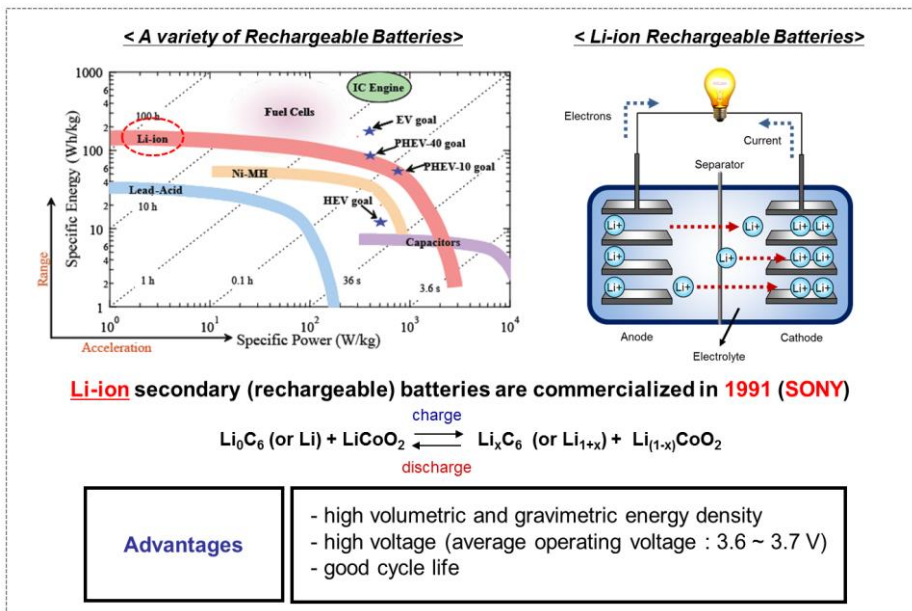


Fig. 1-1 Ragone plot of various battery types and energy storage diagram of commonly used LIBs.

Since the energy density of a battery is mainly determined by the specific capacities and operating voltages between the anode and the cathode, the main focus of research is on the development of active materials. The commercialized LIBs are operating by a ‘rocking chair’ mechanism in which Li ions from oxide-based cathodes move toward graphite anodes during charge and reverse reaction occurs during discharge (Fig. 1-1). These host materials guarantee the long-term stability and safety, but limit the theoretical energy density at the same time.³ In other words, a dramatic increase in the energy density requires new redox chemistries other than the ‘intercalation’ mechanism. For this reason, the materials based on the distinct solid-state reactions, such as conversion or plating, have attracted growing interest owing to their potentially high energy densities.

The redox behaviors caused by new chemistries are distinct from those in the conventional materials, resulting in uncontrolled side reactions and short lifetime. The primary factors responsible for the low reversibility are instabilities during the redox reaction of active materials and uncontrolled side reactions at the electrode/electrolyte interface.⁴ This means that the novel active materials and electrolyte solutions need to be developed and optimized to enable the realization of post-LIBs.

1.2 Issues in Development for Lithium Metal Batteries

Li metal has been considered as one of the most promising anode candidates for high-energy-density batteries due to its high theoretical specific capacity (3860 mAh g⁻¹ or 2060 mAh mL⁻¹) and low reduction potential (-3.04 V vs. standard hydrogen electrode). In general, the energy density can increase up to 200% compared with LIBs when graphite anode is replaced with Li metal anode. Practical Li metal batteries can deliver an energy density approaching 400 Wh kg⁻¹ and 1200 Wh L⁻¹ by integrating Li metal anode with nickel-rich layered oxide cathode, which is regarded as a promising advanced battery in the near future (Fig. 1-2).⁵

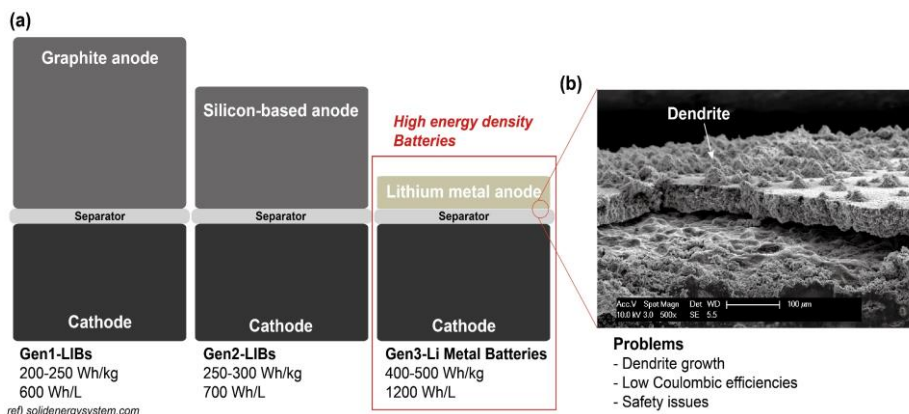


Fig. 1-2 (a) Energy density diagram and (b) the main problems of Li metal batteries

However, Li dendrite growth is the main problem hindering the commercialization of Li metal batteries. It is revealed that Li dendrites can grow under non-uniform solid-electrolyte interphase (SEI) layer which forms when Li contacts with organic electrolytes due to its low reduction potential. The formation of Li dendrites includes two important processes, i.e., the nucleation and growth of Li. The physical and chemical features of SEI layer play a crucial role in the nucleation and the growth of Li, thus causing different types of Li dendrites, such as mossy, whisker, and nodule-like Li.⁶ The growth of Li dendrites destroys fragile SEI layer with decreased coulombic efficiencies, inducing rapid battery decay by depletion of electrolyte or reversible Li metal. In the subsequent stripping process, parts of Li dendrites are isolated from bulk Li metal owing to uneven dissolution rate of Li ions through SEI layer and become irreversible dead Li.

Until now, numerous approaches have been suggested to suppress the dendrite growth including the various protective layers, electrode designs, electrolyte additives, and solid-state electrolytes.⁷ Among these efforts, electrolyte development has been highlighted markedly due to its ability of modifying the composition and morphology of the SEI layer. With regard to the composition of the SEI layer, lithium fluoride (LiF) was revealed as a prominent SEI component to regulate Li deposition behavior owing to its intrinsic properties of high mechanical strength, high surface energy at the Li-LiF

interface, and electrochemical stability.⁸ Therefore, great efforts have been still devoted to constructing fluorinated SEI layer in Li metal batteries.

1.3 Issues in Development for Aluminum Batteries

Rechargeable aluminum (Al) batteries have intrigued growing interest of battery research community in recent years, because Al has excellent theoretical specific capacity (2980 mAh g⁻¹) and volumetric capacity (8040 mAh cm⁻³) as a battery anode.⁹ However, high voltage Al batteries are challenging to achieve due to its relatively high anodic potential than Li (Fig. 1-3). The currently reported rechargeable Al batteries are composed of an Al metal anode, a deep eutectic solvent electrolyte, and a cathode capable of reversible electrochemical reaction with the Al-containing ions generated from the deep eutectic electrolyte. It is noteworthy that reaction with trivalent Al ion (Al³⁺) is extremely difficult due to its strong coulombic interaction with anionic frameworks of most conventional cathode materials.

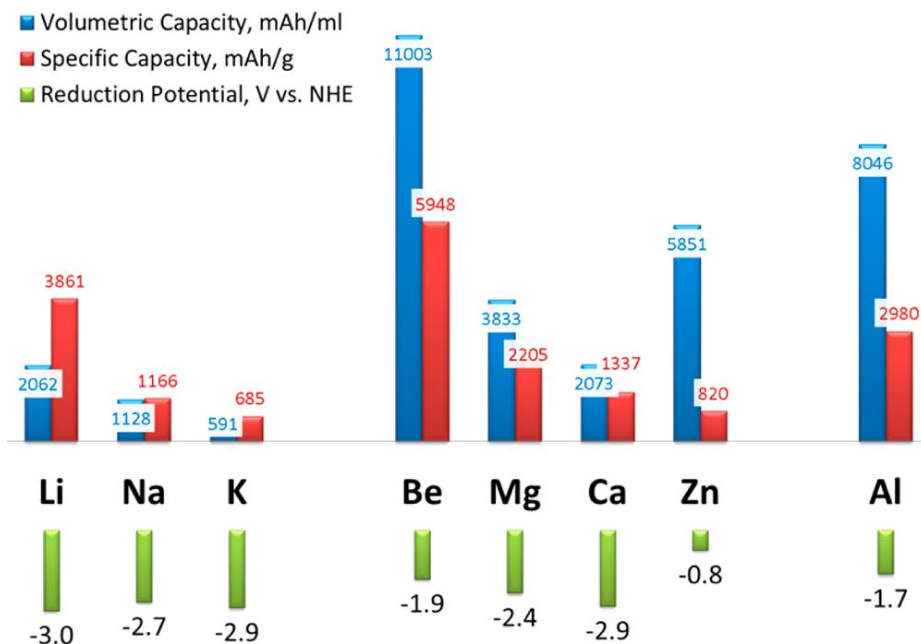


Fig. 1-3 Capacities and reductive potential for various metal anodes.¹⁰

To date, the only electrolytes that can enable reversible Al (de)plating are deep eutectic solvents composed of aluminum halides (AlCl_3 or AlBr_3) and the corresponding halides with various cations. It is well understood that only a Lewis acidic electrolyte, in which the molar ratio of AlCl_3 (or AlBr_3) to corresponding halide is higher than 1, can reversibly deposit and strip Al metal. The active species for Al deposition is the Lewis acidic chloroaluminate anion (Al_2Cl_7^-). The other major chloroaluminate anion paired in the electrolyte is AlCl_4^- , which is not active in Al deposition, but reported to be electrochemical active ions intercalating into the layers of graphite, which have attracted significant attention as the cathode material in rechargeable Al batteries.¹¹

The main research hurdle is on design of cathode materials because most conventional inorganic materials are destructed by Al^{3+} ions during discharge. In specific, the charge of Al^{3+} ions cannot be distributed by the anionic frameworks, thus preventing the Al intercalation. Furthermore, transition metals in the inorganic materials are not able to endure to pristine state within such acidic electrolytes. Therefore, great efforts have been devoted to finding reversible cathode materials with aluminum complex ions.

1.4 Objectives

Uncontrolled dendritic growth and resulting formation of a non-uniform solid-electrolyte-interface (SEI) layer constitute an ever-challenging obstacle in long-term cyclability and safety in Li metal batteries. So far, these drawbacks have been addressed mainly by using non-carbonate electrolytes based on their relatively mild decomposition under reductive environments. In chapter 2, I revealed the role of toluene as a co-solvent of carbonate-based electrolytes for lithium metal anodes.¹² The electron donating nature of the methyl group of toluene shifts the reduction of toluene prior to that of commonly used carbonate solvents, resulting in a more uniform and rigid SEI layer. Moreover, the polymerization process of toluene induces the decomposition of the bis(fluorosulfonyl)imide (FSI) anion in LiFSI salt to yield uniform distribution of lithium fluoride (LiF), and thus lowers an onset salt

concentration in realizing the so-called ‘high concentration effect’ to 3 molar concentration, instead of 5 molar concentration as in typical electrolyte cases. This investigation reveals the usefulness of aromatic compounds in improving the stability of the SEI layer in lithium metal anodes, particularly by tuning the electron density of the benzene ring.

In Li metal batteries, electrolytes containing high-concentration salts have demonstrated promising cyclability, but their practicality with respect to the cost of materials is yet to be guaranteed. In chapter 3, I report a fluorinated aromatic compound, namely 1,2-difluorobenzene, for use as a diluent solvent in the electrolyte to realize the “high-concentration effect”.¹³ The low lowest unoccupied molecular orbital (LUMO) level, weak binding affinity for lithium ions, and high fluorine-donating power of 1,2-difluorobenzene jointly give rise to the high-concentration effect at a bulk salt concentration near 2 M while modifying the composition of the solid-electrolyte-interphase (SEI) layer to be rich in lithium fluoride (LiF). The employment of triple salts to prevent corrosion of the aluminum current collector further improves cycling performance. This study offers a design principle on how to achieve the local high-concentration effect at reasonably low bulk concentrations of salts.

Since aluminum (Al) is the third most abundant element in the Earth’s crust, developing rechargeable Al batteries offers a heaven-sent opportunity for delivering cells with high energy-to-price ratios. Nevertheless, finding appropriate host electrodes for inserting Al (complex) ion remains a fundamental challenge. In chapter 4, I demonstrate a strategy for designing active materials for rechargeable Al batteries.¹⁴ This strategy entails the use of redox-active triangular phenanthrenequinone-based macrocycles which form layered superstructures resulting in the reversible insertion and extraction of cationic Al complex. This architecture exhibits an outstanding electrochemical performance with a reversible capacity of 110 mAh g⁻¹ along with a superior cyclability of up to 5000 cycles. Furthermore, electrodes composed of these macrocycles blended with graphite flakes results in higher specific capacity, electronic conductivity, and areal loading. These findings constitute a major advance in the design of rechargeable Al batteries and represent a good starting point for addressing affordable large-scale energy storage.

Al batteries are of great interest in “beyond-lithium” battery research, because of their remarkably high performance in terms of rate capability and cycle life. The electrochemical performance that has been achieved thus far is unusual as cells usually adopted viscous ionic liquid (IL) electrolytes with bulky complex carrier ions. In chapter 5, I not only demonstrate the excellent rate and cycling performance of phenanthrenequinone (PQ), but also elucidate the origin of this extraordinary performance.¹⁵ Density functional theory (DFT) calculations and experimental analyses jointly revealed that the long-term cyclability of PQ arises from PQ-AlCl₂ complexation, which lessens the effective charge of PQ to mitigate its dissolution into the electrolyte. Moreover, the formation of AlCl₂⁺ without a separate desolvation step allows fast charge transfer, accelerating the AlCl₂⁺ insertion process. This work unveils the importance of aluminum coordination chemistry in determining the key electrochemical properties of aluminum batteries and forms the basis of a new research direction for the development of battery systems based on complex ions.

Chapter 2. Tuning the Reductive Polymerization of Aromatic Solvent for Stable Lithium Metal Batteries

2.1 Introduction

Lithium (Li) metal has received increasing attention as a promising anode material for Li-ion batteries (LIBs) with targeting green electric transportation due to its low redox potential (-3.04 V vs SHE) and unprecedented theoretical capacity (3860 mAh g^{-1} or 2060 mAh mL^{-1}).^{4, 16-18} In spite of these advantages, a substantial gap remains before practical application due to vulnerable dendritic growth during repeated Li deposition and stripping. Dendrite growth causes indiscriminate electrolyte decomposition and dead Li, resulting in inferior charge-discharge reversibility and ultimately severe capacity fading.

Li dendrite growth has been described by two models. One is the ‘space charge’ model. This model focuses on ion depletion at the electrode-electrolyte interface; as current density increases, an ion depletion layer on the electrode surface is formed and thickens.^{19, 20} In this interfacial evolution, Sand’s time, an onset point where an ion depletion layer begins to form, serves as a useful descriptor. Above this point, due to Li ion depletion, Li ions tend to lose their homogeneous distribution in the bulk electrolyte and are rather concentrated toward local spots (so-called surface ‘tips’) with higher electron densities. While this model well explains the behaviors of dendrite growth at different current densities, those at low current densities below Sand’s time are described limitedly.

The other model focuses on the ‘uniformity’ of the SEI layer with respect to morphology and composition, without taking current density into consideration.^{21, 22} This model relies on a viewpoint that in the non-uniform SEI layer, Li ion transport becomes uneven over the electrode area, which accelerates dendrite growth and consequently destroys the SEI layer. Therefore, from this model’s perspective, success in suppressing dendrite growth depends largely on the uniformity and durability of the SEI layer.

Based on the consensus regarding the importance of a uniform SEI layer,

numerous approaches have been introduced, including artificial SEI layers,²³⁻²⁷ LiNO₃ additives,²⁸⁻³⁰ vinylene carbonate (VC) additives,³¹⁻³⁵ fluoroethylene carbonate (FEC) additives,³⁶⁻³⁸ polymer electrolytes,³⁹⁻⁴³ and high concentration electrolytes.⁴⁴⁻⁵⁰ In the case of artificial SEI layers, while their effect is noticeable in the early cycling period, inevitable defects in the SEI layers tend to impair their stability for prolonged cycles, resulting in a limited impact in long-term cycle life. Nevertheless, electrolyte engineering is generally advantageous, as it can be adoptable without implementing additional steps in cell assembly or altering manufacturing procedures significantly. In addition, electrolyte engineering is usually more uniformly applicable to the surface of electrodes and is thus more sustainable over cycling compared to pre-treatments of electrodes (e.g., surface coating, etc.).

Among various electrolyte approaches, high concentration electrolytes (HCEs) stand out because they engage the decomposition of anions in SEI formation in contrast with normal concentration electrolytes in which solvent decomposition is dominant. Moreover, high Li ion concentrations in HCEs delay the onset point of ion depletion to a higher current density and could thus alleviate dendrite growth markedly.⁴⁶ Qian et al.⁴⁷ firstly demonstrated that ether-based HCEs indeed significantly suppress dendritic growth and achieve high Coulombic efficiencies (> 97%). However, this high concentration effect is less pronounced for carbonate solvents, such as ethylene carbonate (EC), diethyl carbonate (DEC), and propylene carbonate (PC) because carbonates have higher reduction potentials for their decomposition than those of ether counterparts, such as dioxolane (DOL), dimethoxyethane (DME), and tetrahydrofuran (THF),^{51, 52} making carbonate-based electrolytes more unstable in the anode potential regime. For this reason, it is widely accepted⁵² that ether-based electrolytes exhibit superior cycling performance for Li metal anodes compared to carbonate-based ones. The weaker reduction stability of carbonate-based electrolytes necessitates even higher concentrations, i.e., 5 M or higher, to achieve the high concentration effect.⁴⁶ However, such high concentrations, in turn, bring critical drawbacks in fabricating cells due to the low wettability and high viscosity of electrolytes. Cost increase is also another critical demerit. Nonetheless, carbonates are still preferred over other electrolytes, as carbonates possess high oxidation stability for compatibility with high voltage cathodes,

as well as long industrial experience in terms of materials design and manufacturing.⁴⁴

In this study, we focus on aromatic compounds as electrolyte components that are involved in the formation of the SEI layer. The benzene ring in aromatic compounds has three double bonds in resonance, which can initiate polymerization in random orientations. Previous investigations reveal^{31, 33} that this bond characteristic of benzene ring results in branched polymeric structures upon polymerization, producing a more compact and durable SEI layer when included in the electrolyte, compared to linear counterparts generated from the decomposition of conventional electrolyte solvents represented by various carbonates and ethers. The polymerization of an aromatic compound depends on the electron density in the benzene ring, and therefore functional groups attached to the benzene ring play an important role based on their electron withdrawing or donating capability. This rationale relating to the electronic properties of the benzene ring has prompted us to systematically study the functional group effect. In our experiment, attachment of an electron donating group (EDG) turned out to be more effective in forming a stable SEI layer when applied to conventional carbonate electrolytes compared to an electron withdrawing group (EWG), which can be understood based on their reduction potential trend. Separately, we have investigated the concentration effect of a salt, lithium bis(fluorosulfonyl)imide (LiFSI), in correlation with the content of lithium fluoride (LiF) in the SEI layer, which is known⁵³ to improve SEI stability substantially in Li metal anodes. Electrolyte engineering based on the optimization of these two parameters allows to reach a decent average Coulombic efficiency (CE) (97.2% for 350 cycles) for carbonate electrolytes. Our findings provide a useful guideline in designing the electrolyte for Li metal anodes, particularly with a focus on uniform SEI formation.

2.2 Result and discussion

When any co-solvents are considered to be added in carbonate-based electrolytes, a key criterion is whether the co-solvents can be reduced at higher potentials than those of carbonate counterparts so that they can alter the properties of the SEI layer. In order to examine this scenario, three different aromatic compounds, benzene (Ben), toluene (Tol), and trifluorotoluene (tfTol) were chosen (Fig. 2-1a) because the three different moieties can change the electron density in the benzene ring and thus the reduction potential. The methyl group of toluene represents an electron donating group (EDG), whereas the trifluoromethyl group of trifluorotoluene represents an electron withdrawing group (EWG).

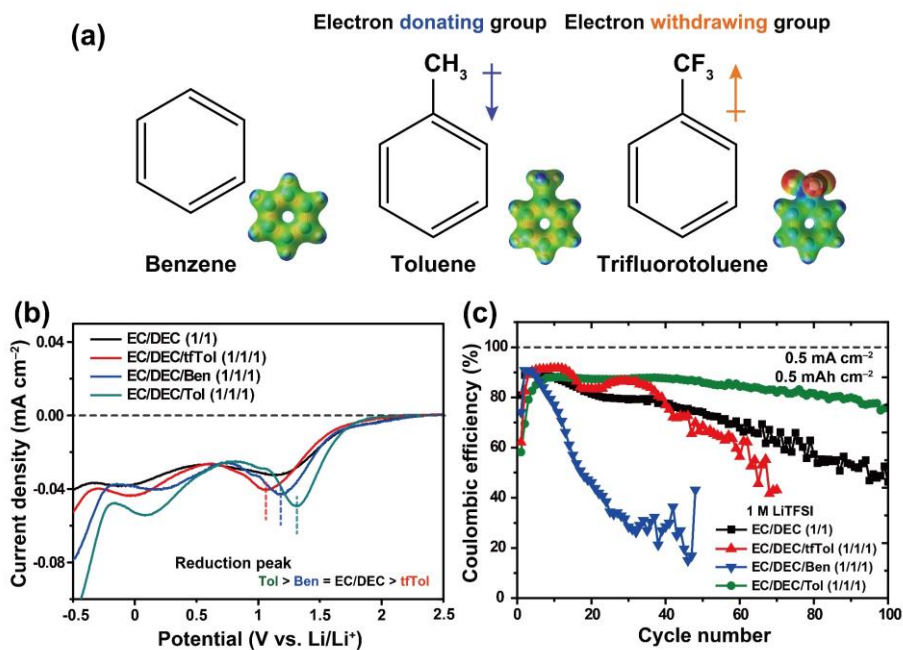


Fig. 2-1 (a) Molecular structures of benzene, toluene, and trifluorotoluene with electron donating/withdrawing character denoted. (b) Linear sweep voltammetry profiles of three EC/DEC electrolytes containing Ben, Tol, and tfTol in addition to the EC/DEC standard case. (c) Cycling performance of the electrolytes in (b) under the Li-Cu cell configuration when measured at 0.5 mA cm^{-2} with 0.5 mAh cm^{-2} .

In an attempt to find optimal ratios of the co-solvents in the electrolytes, salt

solubility and CE were tested with different contents of toluene in an EC/DEC electrolyte. When toluene was added above 60% in volume, phase separation occurred. For reference, LiTFSI is barely soluble in pure toluene. In terms of CE, the volume ratio of EC/DEC/Tol = 1/1/1 exhibited the highest performance, and this ratio was thus adopted for various tests in this work.

Linear sweep voltammetry (LSV) was conducted to determine the reduction potentials of the selected aromatic compounds (Fig. 2-1b). In a Li-Cu cell configuration, potential was scanned from open circuit voltage (OCV) to -0.5 V (*vs* Li/Li⁺) at 5 mV s⁻¹. The trend in reduction potential reflects the electron density in the benzene ring; while the reduction potential of electron-rich toluene was highest, the reduction potential of electron-poor trifluorotoluene was lowest. The reduction potential of benzene positioned in between these two values, which is close to the reduction potential of EC/DEC. These series of results verify that the reduction potentials of aromatic compounds can be tuned by their electron densities in the benzene rings.

The reversibility of Li plating/stripping was evaluated in a Li-Cu asymmetric cell condition for four different electrolyte solvent conditions, EC/DEC, EC/DEC/Ben, EC/DEC/Tol, and EC/DEC/tfTol while 1 M LiTFSI was commonly used as a salt (Fig. 2-1c). The Coulombic efficiency (CE) in this investigation was defined as charging (Li stripping) capacity over discharging (Li plating) capacity. When measured at 0.5 mA cm⁻² with an areal capacity of 0.5 mAh cm⁻², among the three cases in which the aromatic co-solvents were added, only the EC/DEC/Tol mixture exhibited more stable CEs than those of the EC/DEC standard sample. Considering that only the EC/DEC/Tol mixture with the highest reduction potential in the LSV showed improved CEs compared to EC/DEC, it can be rationalized that reduction potential constitutes a good parameter in estimating whether a co-solvent largely participates in the formation of the SEI layer.

The distinct trend between the electrolyte solvent conditions was also reflected in the surface SEM images after Li deposition on the Cu foil (Fig. 2-2). When the current density was 0.2 mA cm⁻², the deposited Li on the EC/DEC electrode exhibited dendritic morphologies, while that on the EC/DEC/Tol electrode showed rounded and compact morphologies. When the current density was increased to 0.5 mA

cm^{-2} , the Li dendrites on the EC/DEC electrode became thinner and more needle-like with more severe growth of the SEI layer (red circles in the inset of Fig. 2-2c), whereas the round shapes of deposited Li on the EC/DEC/Tol electrode still remained. In the case of the EC/DEC/Ben and EC/DEC/tfTol electrodes, the morphology of deposited Li was similarly needle-like, which provides a clue for their rapid decay in CE (Fig. 2-1c). Since the morphology of deposited Li largely depends on the rigidity and coverage of the SEI layer, the observed round-shaped Li on the EC/DEC/Tol electrode indicates the formation of a high coverage rigid SEI layer, once again owing to the precedent decomposition of toluene.

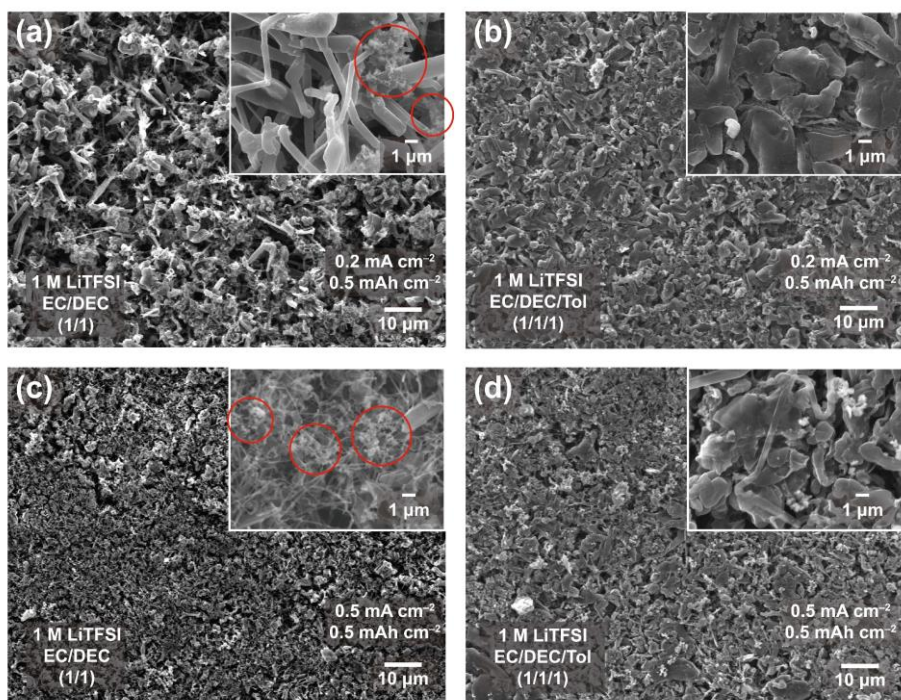


Fig. 2-2 SEM images of deposited Li on Cu foil with different electrolyte solvents and current densities with 0.5 mAh cm^{-2} . 1 M LiTFSI in (a) EC/DEC or (b) EC/DEC/Tol when measured at 0.2 mA cm^{-2} . 1 M LiTFSI in (c) EC/DEC or (d) EC/DEC/Tol when measured at 0.5 mA cm^{-2} .

The mechanism of the formation of a high coverage polymeric SEI layer in the presence of toluene is provided in Fig 2-3. On the Li metal surface with the reductive environment, the C–H bond in the methyl group of toluene is first broken to yield benzyl anion and hydrogen radical. The benzyl anion constitutes a stable species

because the electron in the methyl group can be delocalized with the electrons in the benzene ring,⁵⁴⁻⁵⁶ which must assist in stabilizing the initiation of the polymerization process. In the subsequent propagation step, the hydrogen radical formed in the initiation step attacks the toluene to produce a stable radical intermediate that can undergo resonance bond rearrangement,⁵⁴⁻⁵⁶ leading to polymerization in random orientations along the benzene ring plane. It is plausible that the remaining double bonds in the benzene ring also participate in the polymerization (last arrow in the propagation), resulting in branched polymer structures. This mechanism has been validated by density functional theory (DFT) calculation. As shown in Fig 2-3b, the bond dissociation energy of the C–H bond in the methyl group (1.93 eV) of toluene is conspicuously lower compared with those of the three positions (> 2.7 eV) in the benzene ring of toluene due to the resonance stabilization of benzyl anion. Based on a similar logic, the bond dissociation energy of toluene is also significantly lower than that of benzene (1.93 vs 2.95 eV), explaining the higher reduction potential of toluene. In addition, it is noteworthy that the bond dissociation energy of trifluorotoluene was unable to be retrieved because a convergent value was not available for dissociation energy, reflecting that the reduction of trifluorotoluene is infeasible due to the unstable nature of its reduced form. In Fig. 2-3c, the DFT calculation reveals the importance of the electron density in the benzene ring in relation with the activation energy in the propagation step. It turned out that the higher is the electron density in the benzene ring, the easier it is for the corresponding aromatic compound to form a C–H bond with hydrogen radical. When hydrogen radical approaches the aromatic compound, total energy slightly decreases due to electrostatic attraction (E_2). In order to form the C–H bond (E_4), the reaction should go through the transition state (E_3), and the energy difference between E_2 and E_3 represents the activation energy. The activation energies of toluene, benzene, and trifluorotoluene were 0.149, 0.158, and 0.168 eV, respectively. Although the formation of polyphenylene seems to be feasible based on the same initiation/propagation scheme, such scenario is unlikely to be the case because C=C bond was not detected in the X-ray photoelectron spectroscopy (XPS) analysis in the next paragraph. Considering that the HOMO/LUMO energy levels of the aromatic compounds are not significantly different, it is convinced that their reduction potentials

are determined mainly by the initiation and propagation steps. The results of the DFT calculations reconfirm the importance of the electron density in the benzene ring when an aromatic compound is involved in the polymerization during the formation of the SEI layer.

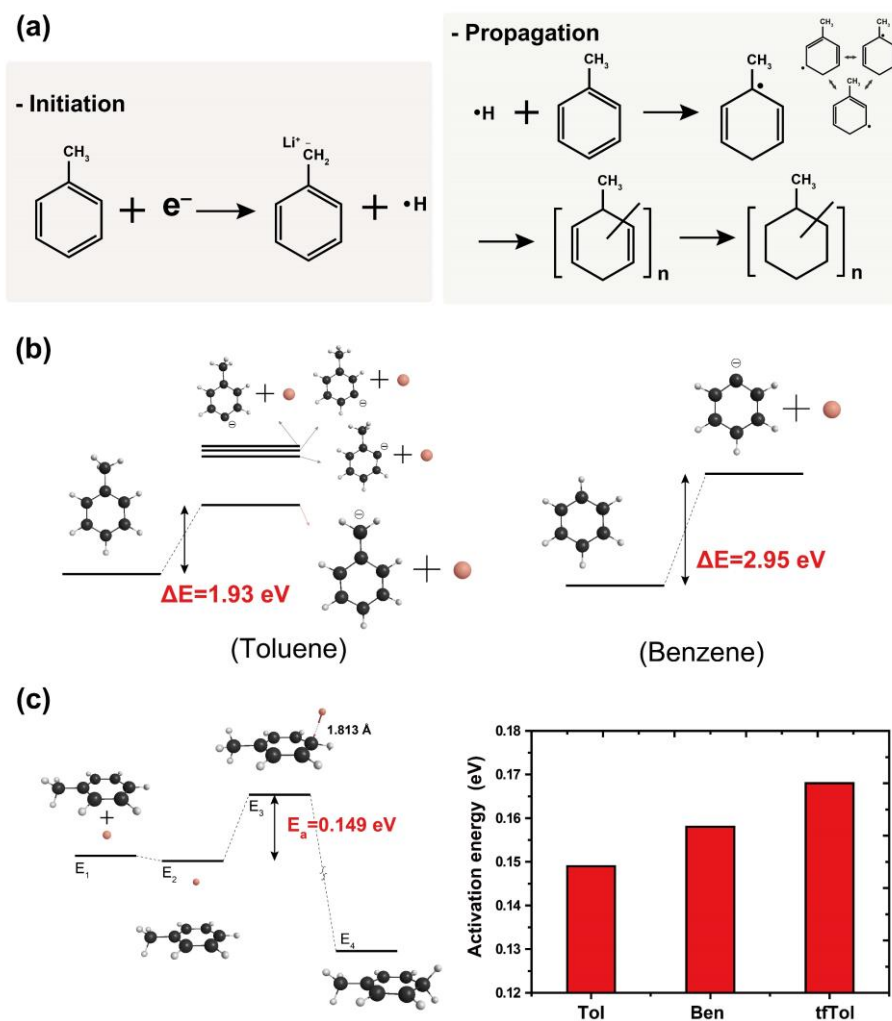


Fig. 2-3 (a) Polymerization scheme of toluene. Energy diagrams along (b) initiation step and (c) propagation step. The black, white, and red balls represent carbon atoms, hydrogen atoms, and hydrogen radicals, respectively.

The chemical composition of the SEI layer was analyzed by XPS. Fig. 2-4

comparatively displays the XPS spectra of SEI layers after one cycle of Li plating and stripping when EC/DEC with and without toluene were used. Both spectra showed peaks at almost identical positions, but the peak intensities were distinct. In the C 1s branches, peaks at 293.0, 290.4, 288.7, 286.6, and 284.8 eV are assigned to the $-\text{CF}_3$, ROCO_2Li , Li_2CO_3 , COR, and C-C bonds, respectively.^{9, 57} Furthermore, the origin of each peak can be elucidated in a way that the $-\text{CF}_3$ peak is generated from the decomposition of TFSI anion, and the C-C peak is attributed to the decomposition of both toluene and EC/DEC, while the other oxygen-containing peaks are ascribed to the decomposition of EC/DEC. According to the C 1s profile of the EC/DEC/Tol case (Fig. 2-4a), the peak corresponding to the C-C bond was more pronounced with respect to other peaks when compared to that of the EC/DEC counterpart (Fig. 2-4c), while the intensities of other peaks originating from TFSI and EC/DEC were lowered substantially.

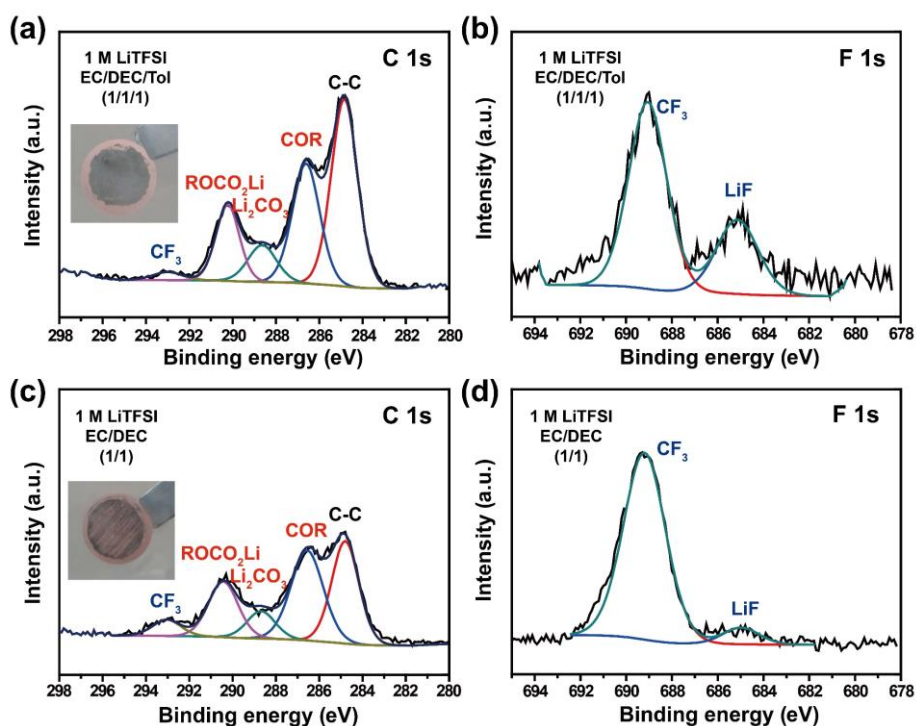


Fig. 2-4 XPS spectra of 1 M LiTFSI in EC/DEC/Tol in (a) C 1s and (b) F 1s branches. XPS spectra of 1 M LiTFSI in EC/DEC in (c) C 1s and (d) F 1s branches. The analyses were performed after one cycle at 0.5 mA cm^{-2} with 0.5 mAh cm^{-2} .

This observation reflects the substantial decomposition of toluene, which in turn weakens the decomposition of EC/DEC and TFSI anion. With regard to the atomic composition in the SEI layer, when toluene was added as a co-solvent, the atomic portion of C increased while that of O decreased. In the F 1s branches (Fig. 2-4b and d), two peaks appeared at 689.1 and 685.1 eV corresponding to $-\text{CF}_3$ and Li-F bond, respectively.⁵⁸ In the case of EC/DEC/Tol, the intensity of the Li-F peak relative to that of the $-\text{CF}_3$ peak was enhanced compared to that of EC/DEC. It is anticipated that even though the decomposition of the C-F bond in the $-\text{CF}_3$ is normally infeasible, the radicals formed during the polymerization of toluene could facilitate the decomposition of $-\text{CF}_3$ to yield LiF, which makes the SEI layer more rigid. A similar observation has been reported in Li-O₂ batteries; TFSI anions can be decomposed to yield LiF by superoxide radicals generated during discharge. These results indicate that the addition of toluene suppresses the decomposition of EC/DEC and alters the composition of the SEI layer by its precedent participation in SEI formation.

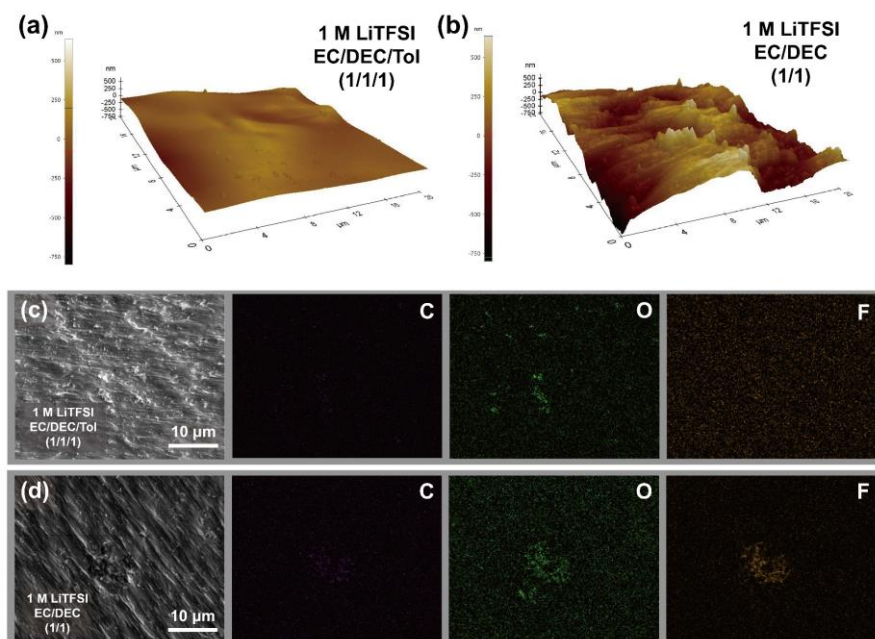


Fig. 2-5 3-D AFM scanning images of the SEI layers formed on Cu foil when 1 M LiTFSI in (a) EC/DEC/Tol and (b) EC/DEC are used as electrolytes. The characterization was performed after discharging from OCV to 0 V at 0.01 mA cm⁻². SEM and EDX images for the same two electrodes.

In order to examine the chemical and morphological uniformity of the SEI layer, 3-D atomic force spectroscopy (AFM) and energy dispersive X-ray spectroscopy (EDX) analyses were conducted (Fig. 2-5). For these analyses, an SEI layer was formed on a Cu foil by scanning the potential from OCV to 0 V (vs Li/Li⁺) at 0.01 mA cm⁻². According to 3-D AFM images (Fig. 2-5a and b), the surface of the electrode with EC/DEC was rougher than that of the electrode with EC/DEC/Tol, which directly visualizes more uniform surface morphology by the addition of toluene. In the same line, the surfaces of the electrodes with EC/DEC/Ben and EC/DEC/tfTol appeared similarly rougher than that of the EC/DEC/Tol case EDX element mapping also supports the role of toluene in the formation of a uniform SEI layer (Fig. 2-5c and d).

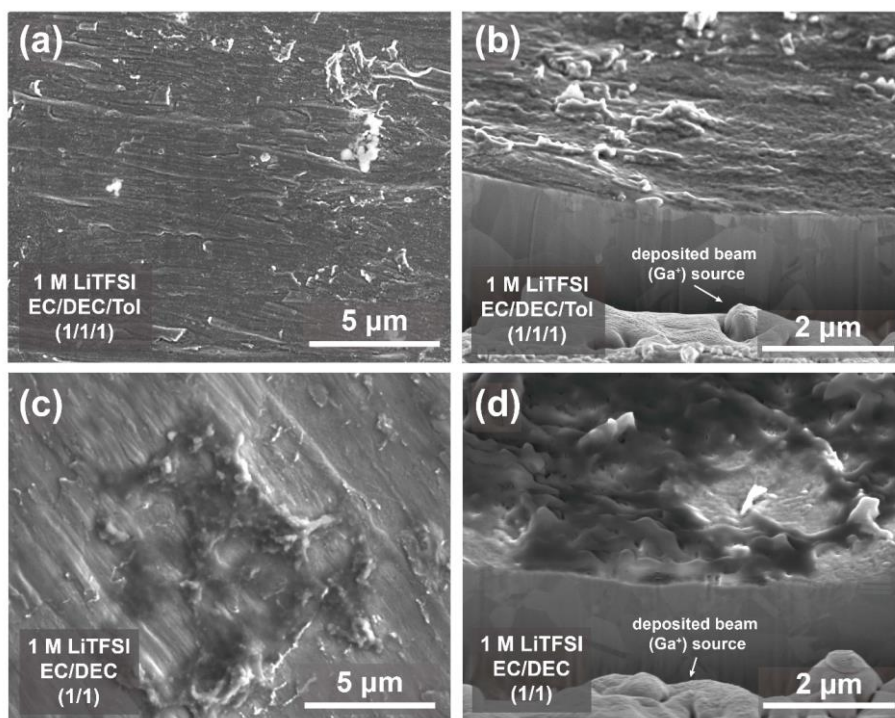


Fig. 2-6 Top-view and cross-sectional SEM images of the SEI layer formed in 1 M LiTFSI in (a, b) EC/DEC/Tol or (c, d) EC/DEC.

See the higher magnification SEM images of the same samples (Fig. 2-6) to capture the surface morphologies more clearly. While the distributions of carbon and oxygen were not largely distinct, the fluorine distribution of the EC/DEC/Tol case was clearly more

uniform than that of the EC/DEC counterpart. This observation indicates less uniform decomposition of TFSI anions in EC/DEC electrolyte, which further deteriorates the morphology of Li deposition. In contrast, the more uniform distribution of fluorine of the EC/DEC/Tol electrode can be understood by the decomposition of TFSI anions that is accelerated through the polymerization of toluene involving the reactive radicals. The accelerated decomposition of TFSI anions was reflected in the increased LiF peak in the XPS spectra.

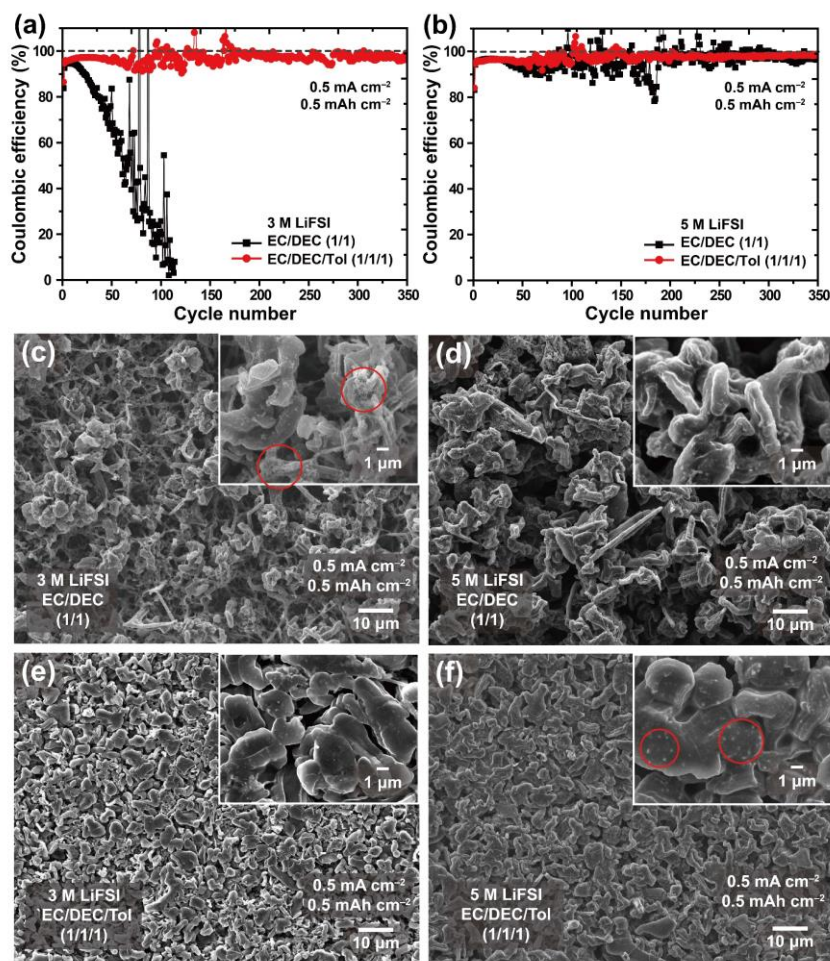


Fig. 2-7 Cycling performance of Li-Cu asymmetric cells with different salt concentrations when measured at 0.5 mA cm^{-2} with 0.5 mAh cm^{-2} : (a) 3 M LiFSI; (b) 5 M LiFSI. SEM images of deposited Li for both solvent compositions with (c, e) 3 M LiFSI and (d, f) 5 M LiFSI.

The effect of toluene was further investigated by varying salt concentration in a Li-Cu asymmetric cell condition, while the current density and areal capacity were set to 0.5 mA cm^{-2} and 0.5 mAh cm^{-2} , respectively (Fig. 2-7). As shown in Fig.2-7a, when 3 M of LiFSI was used, the EC/DEC/Tol cell exhibited an average CE of 97.2% for 350 cycles, whereas the CE of the EC/DEC cell dropped immediately after 40 cycles and reached 0% after 100 cycles. This severe CE drop implies that the concentration of 3 M is not high enough to have the HCE in effect, which is in good agreement with the literature that carbonate-based electrolytes enter the HCE regime at above 5 M.⁴⁶ Remarkably, the capacity of the EC/DEC cell decayed more rapidly at 3 M compared to at 1 M, which suggests that at 3 M, the decomposition of FSI anions is spatially less even. This observation can also be explained by the higher portion of ethylene carbonate in the electrolyte, which results in more uniform and stable SEI layer in the low concentration regime. By contrast, the performance of the EC/DEC/Tol cell at 3 M was clearly superior to that at 1 M due to the uniform LiF-rich SEI layer induced by the polymerization of toluene. The superior performance of the EC/DEC/Tol cell was preserved at other areal capacity and current density conditions. When the salt concentration was increased to 5 M, the HCE effect was more significant for the EC/DEC cell (Fig. 2-7b). While the average CE of the EC/DEC/Tol cell increased slightly to 97.5% for 350 cycles, the average CE of the EC/DEC cell increased drastically to 95.7% due to the known HCE effect that produces the LiF-rich SEI layer. The higher average CEs of the EC/DEC/Tol cell at both concentrations reconfirm the beneficial effect of toluene, even though such effect becomes weakened with increasing concentration. It is worth noting that although CE generally increases with increasing concentration of F-donating salt, extraordinarily high concentrations are less desired from cost and processing viewpoints.

The effect of high concentration on the morphology of Li deposition was examined by SEM analysis (Fig. 2-7c-f). With 3 M LiFSI, the EC/DEC electrode exhibited dendritic growth with uneven electrolyte decomposition residue. However, when the electrolyte concentration was increased to 5 M, the EC/DEC electrode still showed dendrite morphologies, but the decomposed electrolyte residues were observed less frequently. By contrast, the EC/DEC/Tol electrode displayed clearly distinct Li

morphologies and interfacial stability at the same salt concentrations. Evidently, Li dendrites were far more flat and rounded for both concentrations of 3 and 5 M. The effect of toluene co-solvent to weaken the dendritic growth was also observed in cross-sectional SEM images (Fig. 2-8).

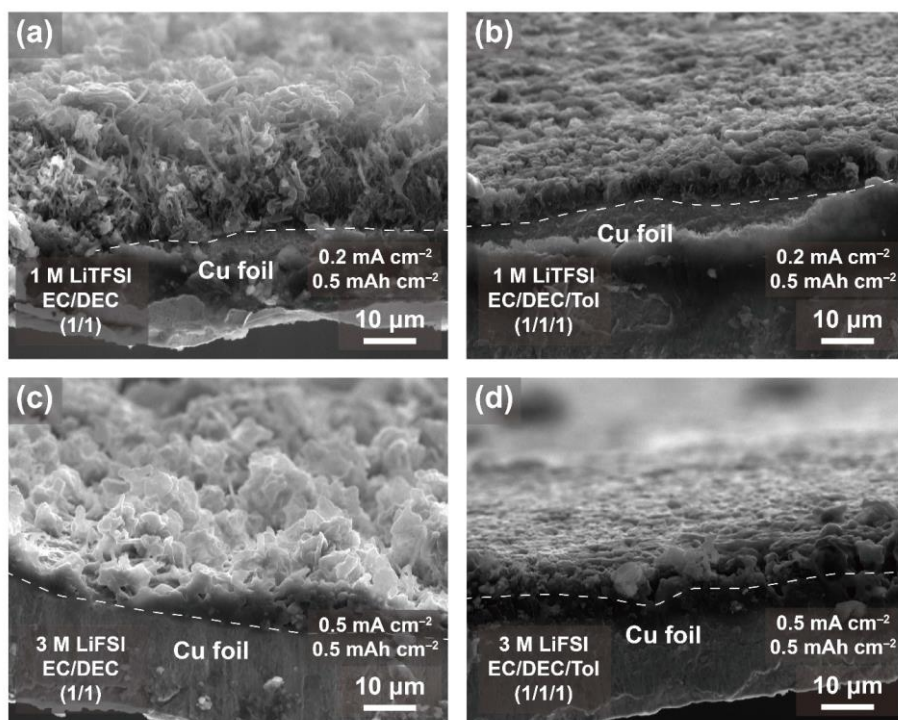


Fig. 2-8 Cross-sectional SEM images of deposited Li on Cu foil with different electrolytes and current densities when areal capacity is fixed at 0.5 mAh cm⁻². 1 M LiTFSI in (a) EC/DEC and (b) EC/DEC/Tol when measured at 0.2 mA cm⁻². 3 M LiFSI in (c) EC/DEC and (d) EC/DEC/Tol when measured at 0.5 mA cm⁻².

In accord with the modified Li morphology, electrolyte residues from reductive decomposition were also markedly reduced for the EC/DEC/Tol electrode at both concentrations. In the case of 5 M LiFSI in EC/DEC/Tol, white spots were observed in the high magnification SEM image (Fig. 2-7f inset), which is ascribed to LiF in the SEI layer and thus serves as a signature of spatially uniform salt decomposition. The series of results indicates that the incorporation of toluene in carbonate-based electrolytes can lower an onset concentration in manifesting the HCE

effect, and can thus avoid excessively high concentrations in salt content that are necessarily accompanied by the aforementioned drawbacks in cost and processing. Hence, the role of toluene in inducing the LiF-rich SEI layer can be beneficially applied for HCEs by lowering the onset salt concentration and therefore allowing for more practically viable cell conditions.

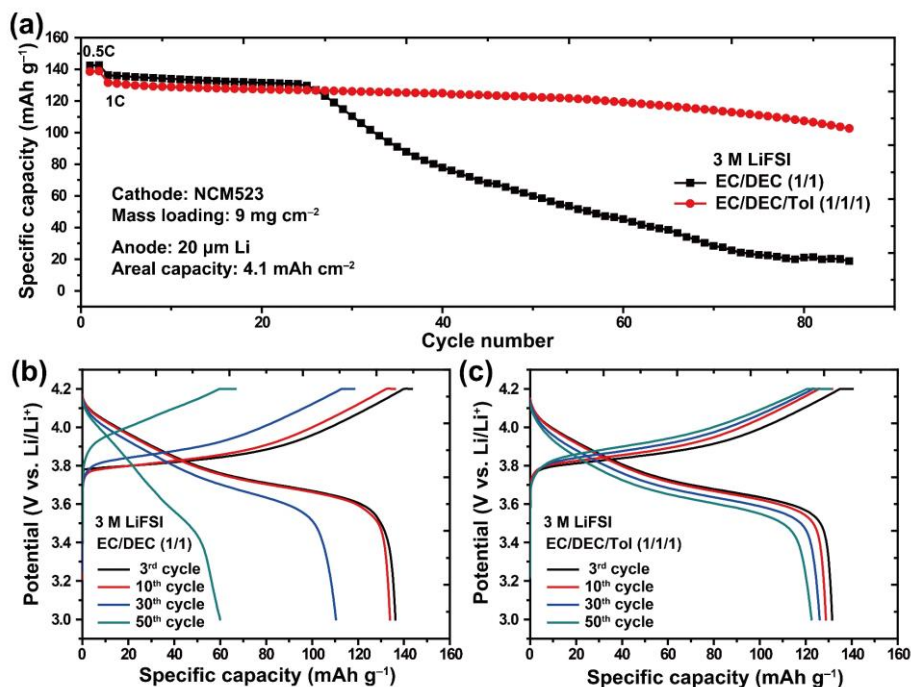


Fig. 2-9 (a) Cycling performance of NCM523-Li full-cells with 3 M LiFSI in EC/DEC and EC/DEC/Tol. (b-c) Corresponding voltage profiles at different cycle numbers. The mass loading of the active material in the cathode is 9 mg cm⁻², and the thickness of the Li layer in the anode is 20 μm.

In order to verify the effect of toluene in a more practical cell setting, full-cells in pairing with LiNi_{0.5}Co_{0.2}Mn_{0.3}O₂ (NCM) cathodes were tested (Fig. 2-9). Importantly, the tests were carried out with a limited amount of Li in the anode (thickness of 20 μm corresponding to 4.1 mAh cm⁻²), as excessive Li contents could exaggerate cycling performance and impair energy density. With the limited amount of Li in the anode, a cathode loading of 9.0 mg cm⁻² was adopted, and 3 M LiFSI in EC/DEC/Tol or EC/DEC was used as electrolytes. For this measurement, the cell was cycled at 0.5C (0.7 mA

cm⁻²) for the first two cycles and then at 1C (1.4 mA cm⁻²) thereafter. The capacity of the EC/DEC cell abruptly dropped at the 25th cycle, which is attributed to a point where excess Li began to be depleted. By contrast, the EC/DEC/Tol cell retained 81.6% after 80 cycles with respect to the capacity at the 3rd cycle in which C-rate was raised from 0.5C to 1C, revealing the improved stability of the SEI layer by the incorporation of toluene. The Li depletion of the EC/DEC cell was reflected in its increased overpotentials and decreased capacities (Fig. 2-9b), which is in sharp contrast with those of the EC/DEC/Tol cell that preserved the voltage profiles far better during the same number of cycles (Fig. 2-9c). Considering the limited freedom in the anode amount and the degree of Li utilization in practical cell designs, the enhanced cyclability of the EC/DEC/Tol cell validates the importance of a uniform and robust SEI layer in practical cells operating based on carbonate electrolytes.

2.3 Conclusion

In conclusion, we have demonstrated toluene as a useful co-solvent for carbonate-based electrolyte solutions for Li metal batteries. The precedented reductive decomposition of toluene prior to that of carbonate solvents commonly used in LIB electrolytes results in a more uniform and rigid SEI layer. The electron donating nature of the methyl group in toluene plays a crucial role in the precedented decomposition and resulting facile radical polymerization with uniform surface coverage. Furthermore, the polymerization process of toluene induces the uniform distribution of LiF and thus enables the ‘high concentration’ effect even with 3 M of LiFSI, leading to relatively decent average Coulombic efficiency of 97.2% over 350 cycles for carbonate electrolytes. The addition of toluene also considerably improves the cycling performance of a full-cell in pairing with LiNi_{0.5}Co_{0.2}Mn_{0.3}O₂ cathode. The present investigation provides a useful guideline in designing carbonate-based electrolytes for Li metal anodes, that is, the addition of aromatic compounds that induces a more stable and rigid SEI layer based on the tuning of the electron density in the benzene ring.

2.4 Experimental

2.4.1 Electrolyte preparation

LiTFSI (99.95%), toluene (anhydrous, 99.8%), benzene (anhydrous, 99.8%), and trifluorotoluene (99%) were purchased from Sigma-Aldrich. LiFSI (>98.0%) was purchased from TCI Chemicals. Ethylene carbonate and diethyl carbonate mixture (v/v = 1:1) was purchased from PANAX ETEC. All electrolytes were prepared in an argon-filled glove box.

2.4.2 Electrochemical measurements

The cathodes were prepared based on the following procedure: $\text{LiNi}_{0.5}\text{Co}_{0.2}\text{Mn}_{0.3}\text{O}_2$ (NCM523), super-P, and polyvinylidenedifluoride (PVDF) were uniformly dispersed in N-methyl 2-pyrrolidone in a weight ratio of 80:10:10. The well-mixed slurry was cast onto Al foil using the doctor blade technique. The cast electrodes were dried under vacuum at 80 °C for 12 h. The areal mass loading of the active material was 9.0 mg cm⁻². The electrochemical performance was characterized by preparing 2032 coin-type cells. The full cells were composed of Li metal anode with a thickness of 20 μm (Honjo Metal, Japan), a polypropylene separator with a thickness of 25 μm (Celgard 2400), and the NCM523 cathode with different electrolytes. Asymmetric cells were composed of Cu foil electrode and Li metal counter electrode. The full-cell assembly was carried out in an argon-filled glove box. All of the electrochemical measurements were performed at 25 °C using a battery cycler (MACCOR series 4000).

2.4.3 Characterization

For all of the characterizations after electrochemical measurements, the cells were disassembled in an argon-filled glove box, and the cycled Li metals were washed with EC/DEC solvent and dried under vacuum for 3 h in a chamber connected to a glove box. In order to characterize the morphologies of the Li metal electrodes, field-emission scanning electron microscope (SEM) (JSM-7800F Prime, JEOL, Japan) at the National Center for Inter-University Research Facilities (NCIRF) at Seoul National University was used. The chemical compositions and bonding characteristics of the SEI

layers were analyzed by XPS (Sigma Probe, Thermo VG Scientific, England) with an Mg K α line as an X-ray source. The binding energies were calibrated with respect to the C 1s peak at 284.5 eV. Atomic force microscope (NX-10, Park Systems) was used to characterize the roughness of the SEI layers. For all characterizations, moisture and air contamination were avoided by using an airtight sample box during each sample transfer.

2.4.4 DFT calculation

Geometry optimizations and energy calculations were performed without symmetry restriction using the B3LYP hybrid density functional implemented in the General Atomic and Molecular Electronic Structure System (GAMESS).⁵⁹ The 6-311+G(d, p) basis sets were adopted for H, F, and C atoms. The threshold value of 0.00001 hartree for self-consistency-field energy for ‘tight’ optimization was adopted. The energy calculations were performed in gas phase to compare the trends of aromatic compounds explicitly. When harmonic frequencies were calculated for optimized transition states, only single imaginary frequencies were obtained in all cases.

Chapter 3. Fluorinated Aromatic Diluent in Localized High-Concentration Electrolytes

3.1 Introduction

As state-of-the-art lithium ion batteries (LIBs) are approaching their practical limit in terms of energy density, lithium (Li) metal has lately received much attention as an alternative anode material to the conventional graphite on account of its unparalleled theoretical capacity (3860 mAh g^{-1} or 2060 mAh mL^{-1}) and low electrochemical potential (-3.04 versus the standard hydrogen electrode).^{60, 61} Nonetheless, the battery community is still struggling to address the ever-challenging issue of poor stability of the Li | electrolyte interface.⁶²⁻⁶⁴ From a morphological perspective, the moderate Li ion diffusion on the Li metal surface and its low surface energy lead to uncontrolled growth of Li dendrites, especially when the plating current surpasses the so-called sand's time.^{6, 65} The high reactivity of Li metal leads to the formation of a weak solid-electrolyte-interphase (SEI) layer composed of randomly distributed inorganic and organic components upon reductive reaction with classical carbonate electrolytes.^{66, 67} The non-uniform and fragile SEI layer accelerates dendritic growth with cycling, thereby undermining the cycle life and adversely impacting upon the safety.

To date, a myriad of approaches have been used to stabilize Li metal anodes including the employment of various protective layers,^{8, 68-70} electrode designs,⁷¹⁻⁷⁶ electrolyte additives,^{22, 30, 37, 77-79} and solid-state electrolytes.⁸⁰⁻⁸³ Among these efforts, electrolyte engineering has been highlighted markedly because of its possibility of modifying the composition and morphology of the SEI layer such that it improves the charge-discharge efficiency without sacrificing the energy density of a cell significantly. With regard to the composition of the SEI layer, lithium fluoride (LiF) was identified as a desirable SEI component to suppress dendritic growth owing to its intrinsic properties of high mechanical strength, high surface energy at the Li-LiF interface, and electrochemical stability across a wide potential range.^{8, 84} In addition, He *et al.*

discovered that LiF surrounded by an organic outer layer, which is formed as a result of the electrochemical decomposition of the electrolyte, is able to more effectively suppress dendritic growth as compared to a chemically formed LiF-containing surface layer, which easily ruptures during the growth of dendrites.⁸⁵ It was also reported that the spatial distributions of LiF and lithium oxide (Li₂O) in the SEI layer play a crucial role for Li dendrite suppression.^{86, 87}

Conventional carbonate-based electrolytes tend to generate a fragile mosaic SEI layer rich in Li₂O and lithium carbonate (Li₂CO₃), which are distributed in an amorphous organic polymer matrix. These Li-containing components induce relatively high local Li ion migration and consequently accelerate the growth of Li dendrites, severely impairing the cycle life of a cell.⁸⁸ In an effort to avoid this problem common to carbonate solvents, Fan *et al.* demonstrated that high concentrations (> 6 M) of lithium bis(fluorosulfonyl)imide (LiFSI) salt lead to the formation of a LiF-rich SEI layer by decreasing the portion of free solvent molecules and modifying the Li⁺ solvation shell such that it becomes anion-abundant.⁴⁶ Even though it is widely accepted that high-concentration electrolytes (HCEs) improve the overall cell performance remarkably,⁸⁹ HCEs are not yet ready to be widely implemented in practical cells because of their high cost, high viscosity, and poor wetting to the electrode and separator.

In recent years, a concept known as localized high concentration electrolyte (LHCE) was proposed, in which an inert cosolvent is used to dilute HCEs while preserving the local solvation structure of the Li ion. Hydrofluoroethers (HFEs) such as 1,1,2,2-tetrafluoroethyl 2,2,3,3-tetrafluoropropyl ether,⁹⁰ tris(2,2,2-trifluoroethyl) orthoformate,^{91, 92} and bis(2,2,2-trifluoroethyl) ether^{44, 93} were demonstrated to be effective diluent solvents to realize the high-concentration effect on the basis of being inert and barely dissolving the lithium salt. Thus, the inclusion of diluent solvents has the advantage of enabling the electrolyte to maintain the Li-coordination environment in the HCE while lowering the bulk salt concentration to a more practical level. Although LHCEs with HFE solvents can improve the cell performance substantially, the role of HFEs is more or less passive in that they mainly suppress the decomposition

of carbonate solvents; however, they do not permit the composition of the SEI layer to be actively tuned.

Herein, we report 1,2-difluorobenzene (1,2-dfBen) as a fluorine-donating (F-donating) non-HFE diluent solvent for LHCEs, which not only induces the high-concentration effect but also transforms the SEI layer into being LiF-rich. Our decision to concentrate on fluorinated aromatic compounds at the molecular design stage was prompted by the low dielectric constants and high fluorine-donating nature of these compounds. Toward this end, a variety of aromatic compounds and their fluorinated analogues were screened, focusing on both their capability as diluent and their fluorine-donating properties. After the series of compounds was screened, the dual F-functionality of 1,2-dfBen to yield two LiF units per each molecular unit upon rigorous reaction with Li metal *via* the formation of a unique intermediate organolithium complex attracted our attention.⁹⁴ These features allow 1,2-dfBen-containing LHCEs to preserve the anion-abundant local solvation structure in the bulk electrolytes while passivating the Li metal with a LiF-rich SEI layer upon Li plating, thereby effectively suppressing dendritic growth. Moreover, by incorporating a suitable combination of salt and additive, LHCEs that are stable with respect to both Li metal and 4-V cathodes were recognized, and highly competitive electrochemical properties were demonstrated in lithium-copper (Li-Cu) asymmetric and full-cell configurations.

3.2 Result and discussion

To determine the feasibility of reduction, we calculated the lowest unoccupied molecular orbital (LUMO) levels of selected solvents: dimethyl carbonate (DMC), bis(2,2,2-trifluoroethyl) ether (BTFE), benzene (Ben), fluorobenzene (fBen), and 1,2-difluorobenzene (1,2-dfBen). The LUMO level is generally accepted as a descriptor to determine the reduction priority upon electrochemical bias such that the lower the LUMO level is, the earlier reduction occurs. Among the solvents of interest, DMC showed the highest LUMO level of 0.129 eV, followed by BTFE at -0.357 eV (Fig. 3-1a). In the case of the benzene derivatives, the LUMO level typically decreases as hydrogen is increasingly substituted by fluorine because the strong electronegativity of the fluorine atom withdraws electrons from the benzene ring. This trend was indeed observed for methoxybenzene (mBen) and (trifluoromethoxy)benzene (tfmBen). The LUMO level of 1,2-dfBen is -0.943 eV, which is significantly lower than that of BTFE, suggesting the possibility of undergoing facile reduction on the surface of Li metal. The LUMO levels of all the solvents covered in this study are summarized in Table S1.

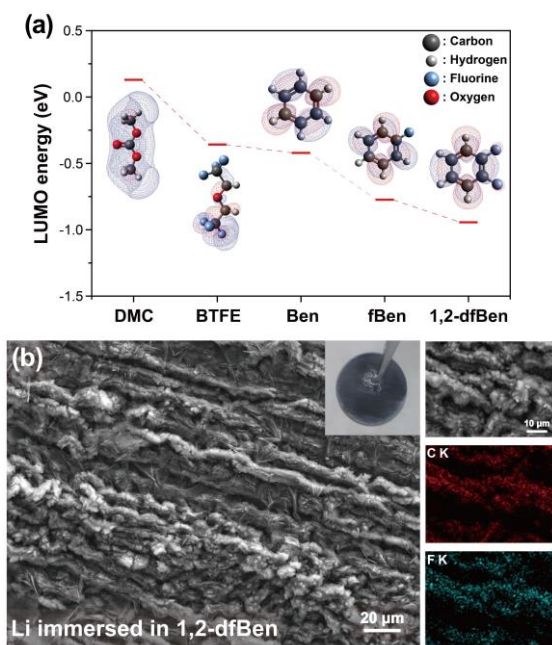


Fig. 3-1 (a) LUMO energy levels of DMC, BTFE, Ben, fBen, and 1,2-dfBen. (b) SEM image of Li metal after immersion in 1,2-dfBen for 1 day and its EDS mapping images with respect to carbon and fluorine. (Inset) Digital photograph of the same Li metal foil.

Solvent	LUMO level (eV)	Binding energy (eV)	Chemical reactivity with Li metal	Cyclability (cycle)
DMC	0.129	-1.57	X	7
BTFE	-0.357	-1.41	X	159
Ben	-0.421	-1.23	X	189
fBen	-0.774	-0.98	X	196
1,2-dfBen	-0.943	-0.76	O	288
1,3-dfBen	-0.965	-0.74	X	232
mBen	-0.487	-1.54	X	123
tfmBen	-0.902	-1.03	X	176
tfTol	-1.276	-0.91	X	218

Table 3-1 LUMO levels, binding energies, and cyclability of cosolvents used in this study. Cyclability refers to the cycle number when the CE of a Li-Cu asymmetric cell drops below 90% when tested with a capacity of 0.5 mAh cm^{-2} at 0.5 mA cm^{-2} .

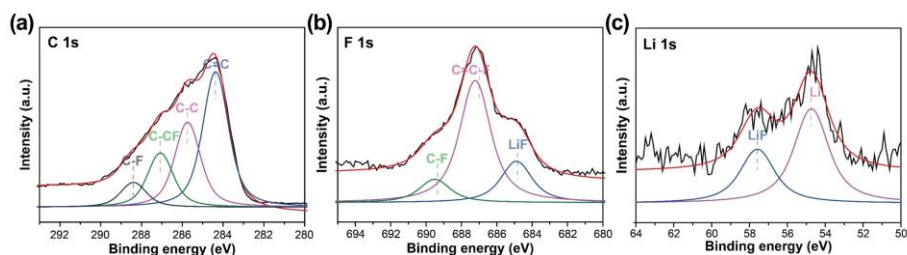


Fig. 3-2 XPS spectra of Li metal in (a) C 1s, (b) F 1s and (c) Li 1s branches after immersion in 1,2-dfBen for 1 day.

We investigated the chemical reactivity of the selected solvents with Li metal by immersing the Li metal foil in each of the solvents for one day. Whereas the surface of the Li metal remained smooth in the other solvents, the surface morphology of the Li metal exposed to 1,2-dfBen exhibited a highly uneven morphology and was composed of carbon and fluorine (Fig. 3-1b). We characterized these surface structures

by conducting X-ray photoelectron spectroscopy (XPS) analyses (Fig. 3-2). The C 1s branch displayed peaks at 284.2, 285.8, 287.1, and 288.4 eV, which can be assigned to the C=C, C-C, C-CF, and C-F bonds, respectively.^{95, 96} For the F 1s branch, peaks at 684.8, 687.2, and 689.8 eV were detected, corresponding to LiF and the C=C-F and C-F bonds, respectively.^{79, 97} The relatively weak intensity of the C-F bond and the appearance of LiF prompted us to infer that 1,2-dfBen reacted with Li metal to produce LiF and graphitic carbon as products. The formation of graphitic carbon is attributed to the decomposition of the benzene ring of 1,2-dfBen. The formation of LiF was additionally verified by a peak at 57.6 eV in the Li 1s branch. In addition, when Li metal foil was immersed in an electrolyte containing 1,2-dfBen for one day, the color and level of gloss did not change significantly, implying that once Li foil is passivated by the compact SEI layer, the Li foil is protected from further reaction with 1,2-dfBen.

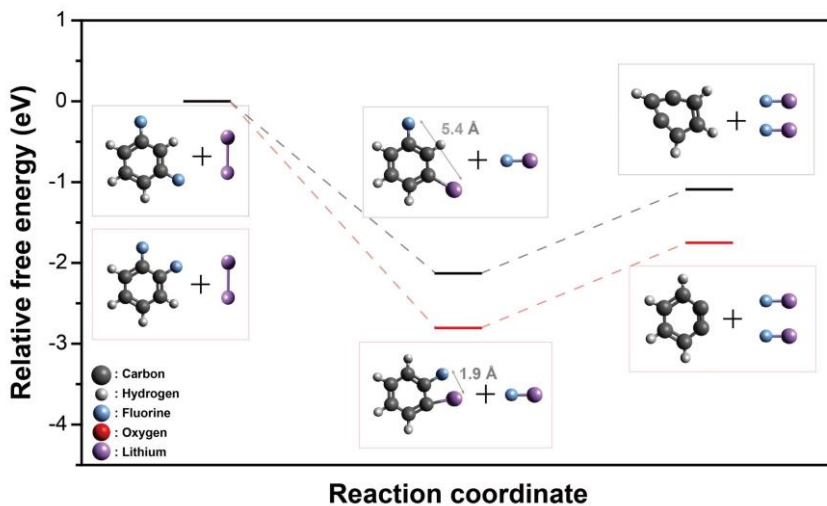


Fig. 3-3 Relative free energies of 1,2-dfBen and 1,3-dfBen along the reaction coordinate.

Peculiarly, 1,3-dfBen was not as reactive with Li metal as 1,2-dfBen in the same immersion test although the LUMO level of 1,3-dfBen is lower at -0.965 eV. This observation suggests that the LUMO level is not the only factor to be considered in determining the chemical reactivity. To further elucidate the reaction mechanism, we conducted density functional theory (DFT) calculations. The reaction models were based on the formation and decomposition of organolithium complexes, because

organohalogen compounds are well known for their strong tendency to react with Li metal to yield organolithium complexes.^{98,99} Fig. 3-3 shows the free energy landscapes for the reaction of 1,2-dfBen and 1,3-dfBen along the reaction coordinates. The calculations revealed that the free energies of 1,2-dfBen are conspicuously lower relative to those of 1,3-dfBen in both steps involving sequential LiF formations. Moreover, the smaller Li-to-F distance of 1,2-dfBen in the organolithium complex compared to that of 1,3-dfBen (1.9 vs. 5.4 Å) imposes a lower activation energy barrier on subsequent Li–F formation. Thus, although 1,2-dfBen is isomeric to 1,3-dfBen, the adjacent fluorine positions of 1,2-dfBen further promote the LiF formation as the reacting Li and F at the intermediate state are both covalently bonded to the benzene ring. This positional difference of fluorine explains the more facile formation of LiF in the SEI layer of the 1,2-dfBen case.

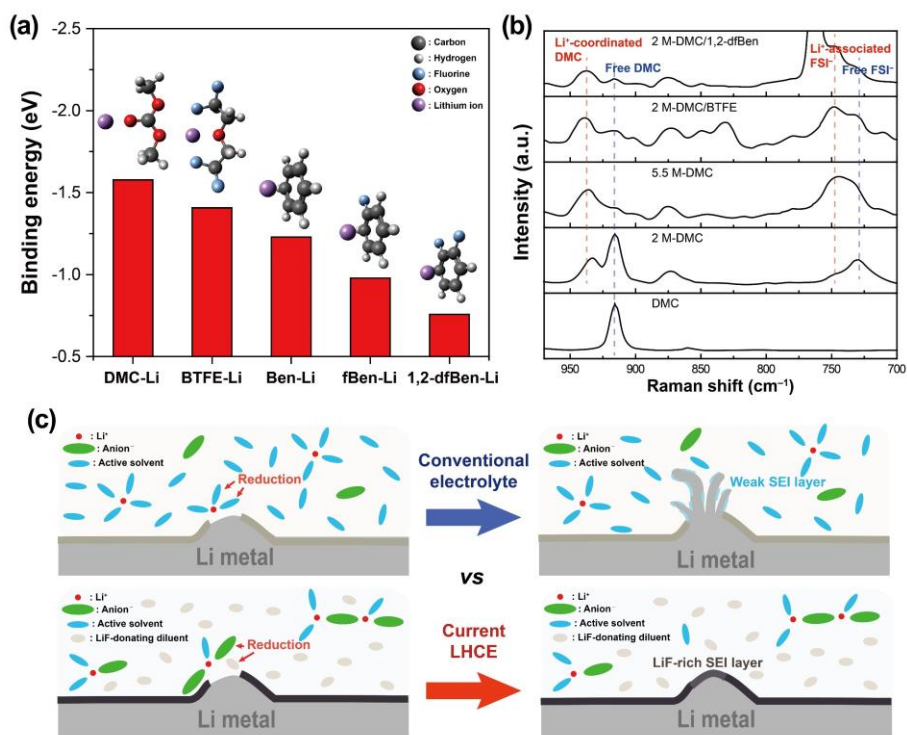


Fig. 3-4 (a) Binding energies of DMC, BTFE, Ben, fBen, and 1,2-dfBen with a Li ion. (b) Raman spectra of DMC, 2 M-DMC, 5.5 M-DMC, 2 M-DMC/BTFE, and 2 M-DMC/1,2-dfBen. (c) Schematic illustration of the mechanism of SEI layer formation of the conventional electrolyte and current LHCE.

In an attempt to evaluate the diluting power of the solvents, we calculated the binding energy of each solvent with the Li ion (Fig. 3-4a). For this purpose, we quantified the binding energy, which is defined as the energy difference between the optimized binding state and the sum of each component. The binding energy of DMC was -1.57 eV, whereas that of BTFE, a known diluent used in LHCEs, was -1.41 eV, suggesting that DMC likely binds exclusively with a Li ion in DMC/BTFE mixtures. The binding energy of Ben was relatively low at -1.23 eV (in absolute term) owing to the absence of functional groups with an effective negative charge. Noteworthy is that the binding energy of mBen, with an ether functional group, was comparatively high (in absolute terms) at -1.54 eV. In the case of the benzene derivatives, as the number of fluorine substituents increases, the binding energy decreases because the fluorine withdraws electrons from the benzene ring. Based on the combined effect of the benzene ring and fluorine substitution, 1,2-dfBen had the lowest binding energy of -0.76 eV, thereby confirming its superior diluting power in LHCEs. Consistent results were obtained when FSI anion was taken into account in evaluating the binding energies.

To characterize the coordination environments, we recorded the Raman spectra of various electrolytes (Fig. 3-4b). Note that we prepared all the LHCEs in solvent mixtures of DMC/diluent ($v/v=3/7$). Upon coordination with a Li ion, the corresponding peaks of DMC or FSI⁻, i.e., O-CH₃ (of DMC) (920 cm^{-1}) or N-S (of FSI⁻) (725 cm^{-1}), shifted to longer wavelength numbers.¹⁰⁰ When the concentration of LiFSI salt was increased from 0 M to 5.5 M, the peak of free DMC at 920 cm^{-1} gradually weakened at the expense of the growth of the peak at 940 cm^{-1} corresponding to the Li⁺-coordinated DMC.¹⁰¹ A similar trend was observed for FSI⁻; an increase in the salt concentration decreased the intensity of the peak of free FSI⁻ at 725 cm^{-1} , whereas the intensity of the peak at 750 cm^{-1} related to the Li⁺-associated FSI⁻ increased.¹⁰² Importantly, when diluted by BTFE or 1,2-dfBen, the peak at 940 cm^{-1} corresponding to Li⁺-coordinated DMC was preserved to a greater extent, indicating the more persistent coordination environments of DMC and FSI⁻ even after the addition of BTFE and 1,2-dfBen. The diluent character of BTFE and 1,2-dfBen was also revealed by the peaks of free BTFE and 1,2-dfBen that were largely preserved in the electrolytes. In

this line, 2 M LiFSI in DMC/1,2-dfBen ($v/v=3/7$) (abbreviated as 2 M-DMC/1,2-dfBen) more effectively maintained the relative peak ratio between the coordinated DMC and free DMC compared to that of 2 M-DMC/BTFE. This observation is in good agreement with the results of the binding energy calculations in that 1,2-dfBen is less interactive. Based on the results of the binding energy calculations and Raman spectroscopy, we portray the coordination structure of the Li ion in LHCE with 1,2-dfBen and its SEI character in Fig. 3-4c, in comparison with that of the conventional electrolyte. In the former case involving 1,2-dfBen, a high portion of Li ions are coordinated with the anions while the 1,2-dfBen diluent is available near the electrode surface. Thus, when Li plating occurs, the coordinated anions and 1,2-dfBen could both be decomposed to yield a LiF-rich SEI layer.

The effect of 1,2-dfBen on the electrochemical performance was evaluated by testing Li-Cu asymmetric cells under different electrolyte conditions (Fig. 3-5). The Coulombic efficiency (CE) in this investigation was defined as the charging (Li stripping) capacity over the discharging (Li plating) capacity. When cycled at a fixed capacity of 0.5 mAh cm^{-2} at 0.5 mA cm^{-2} for each charge and discharge, the cell with 5.5 M-DMC decayed rapidly after 10 cycles, implying the moderate high-concentration effect of this electrolyte. Although 5.5 M-DMC was previously reported to deliver the high-concentration effect with surfactant-coated separators,⁴⁴ the cells with bare separators in this study exhibited limited cyclability because of poor electrolyte wetting, unveiling the negative effect of HCEs when adopted for cells with common polyethylene or polypropylene separators. In the case of 2 M-DMC/BTFE, the cycling period with high CE ($>90\%$) was extended to 159 cycles mainly owing to the improved wettability. In the case of benzene derivatives with the same salt condition, the cyclability of the cells with LHCEs diluted by Ben and fBen improved, sustaining high CE ($>90\%$) for 189 and 196 cycles, respectively. Remarkably, the cell of which the LHCE was diluted by 1,2-dfBen exhibited even greater cyclability by maintaining the high CE ($>90\%$) for 288 cycles owing to the combined features of the fluorine-donating capability and high diluting power of 1,2-dfBen.

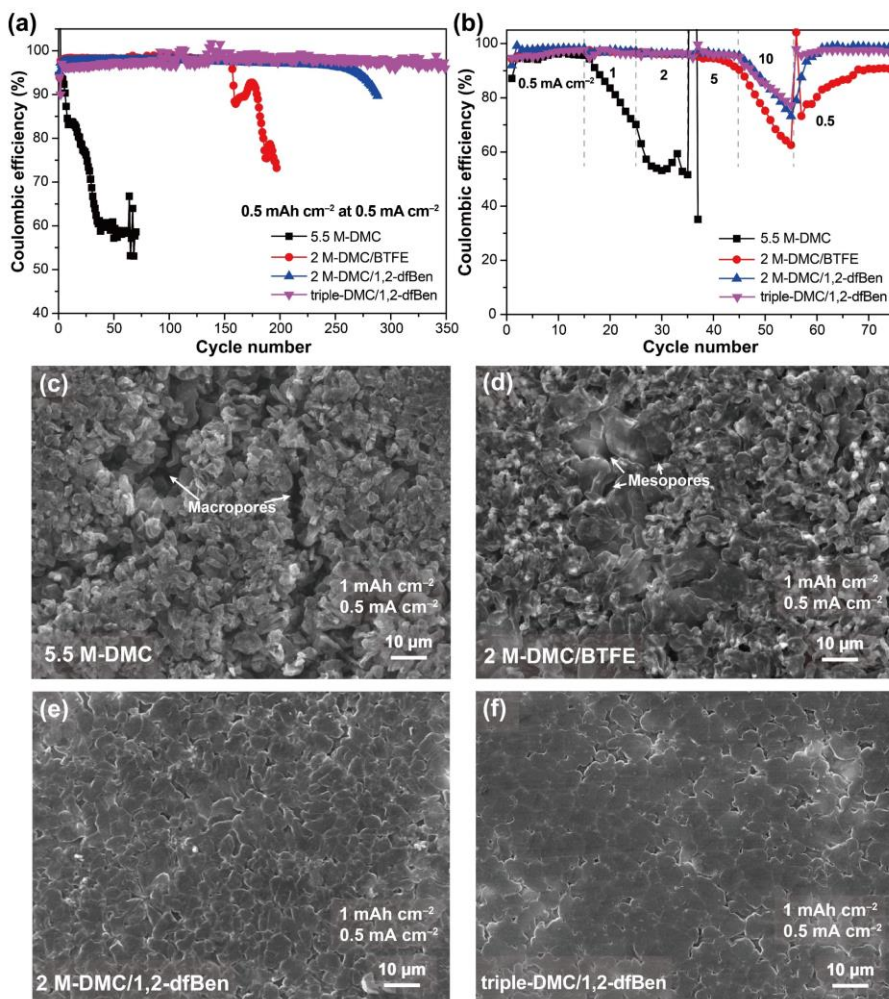


Fig. 3-5 Cycling performance of Li-Cu asymmetric cells with different electrolytes with a capacity of 0.5 mAh cm^{-2} at (a) 0.5 mA cm^{-2} and (b) various current densities of 0.5, 1, 2, 5, and 10 mA cm^{-2} . SEM images of plated Li with (c) 5.5 M-DMC, (d) 2 M-DMC/BTFE, (e) 2 M-DMC/1,2-dfBen, and (f) triple-DMC/1,2-dfBen.

To further enhance the performance, we adopted triple salts, such as $1.3 \text{ M LiFSI} + 0.7 \text{ M LiTFSI} + 0.02 \text{ M LiPF}_6$ in DMC/1,2-dfBen (abbreviated as triple-DMC/1,2-dfBen), by benchmarking recent findings that the dual salts of LiTFSI and LiFSI can enhance the kinetics of FSI⁻ decomposition,¹⁰³ and that the additive LiPF₆ can induce a robust SEI layer and prevent the corrosion of the aluminum current collector.¹⁰⁴ The cell with this electrolyte composition extended the cycle life

significantly even to 350 cycles when the same criterion with regard to cyclability was applied. The average CEs of 2 M-DMC/1,2-dfBen and triple-DMC/1,2-dfBen for 200 cycles were 97.7% and 97.5%, respectively. When the areal capacity was increased to 1 and 3 mAh cm⁻², the average CEs of 2 M-DMC/1,2-dfBen and triple-DMC/1,2-dfBen increased to 98.3% and 98.2% for 1 mAh cm⁻² (for 100 cycles) and 99.0% and 99.1% for 3 mAh cm⁻² (for 40 cycles), respectively. The increased values at 3 mAh cm⁻² are attributed to the decreased portion of the SEI layer that sacrificed the CE.

We further investigated the effect of the electrolytes at various current densities of 0.5, 1, 2, 5, and 10 mA cm⁻² (Fig. 3-5b). The CE of 5.5 M-DMC decreased rapidly at a current density of 1 mA cm⁻², revealing its weak tolerance against increasing the current density. The CE of 2 M-DMC/BTFE was stable up to a current density of 5 mA cm⁻², but failed to recover when the current density was lowered to 0.5 mA cm⁻² after being maintained at 10 mA cm⁻² for a certain period. The CEs with 2 M-DMC/1,2-dfBen and triple-DMC/1,2-dfBen decayed to certain levels at the highest current density of 10 mA cm⁻². However, these CEs recovered to above 98.8% when the current density was returned to 0.5 mA cm⁻², pointing to improved robustness against high current abuse. The superior rate performance of the 1,2-dfBen-containing electrolytes might also be associated with its low binding energy with the Li ion.

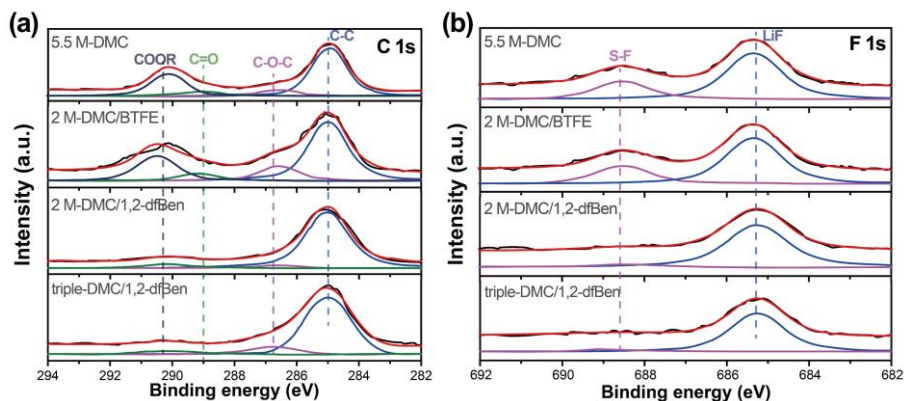


Fig. 3-6 XPS spectra of the SEI layers in the (a) C 1s and (b) F 1s branches in the presence of different electrolytes. The analyses were performed after three cycles of Li plating and stripping with a capacity of 0.5 mAh cm⁻² at 0.5 mA cm⁻².

The morphology of Li plated in the presence of different electrolytes was examined by scanning electron microscopy (SEM) (Fig. 3-5c–f). For this analysis, Li with a capacity of 1 mAh cm^{-2} was plated onto Cu current collectors at a current density of 0.5 mA cm^{-2} . The Li that was plated in 5.5 M-DMC exhibited granular morphologies with sizes of 2–5 μm and abundant macropores between Li bundles. In the case of 2 M-DMC/BTFE, the plated Li showed larger granule sizes of 5–15 μm but fewer macropores. In stark contrast, the Li plated in 2 M-DMC/1,2-dfBen displayed granules that were more flat and compact with far fewer macro- and meso-pores. This morphological trend was more prominent for the electrolyte triple-DMC/1,2-dfBen such that the Li deposits had even greater flatness and compactness, owing to the synergistic effects of the triple salts and the fluorine-donating nature of 1,2-dfBen.

The chemical composition of the SEI layer was analyzed by X-ray photoelectron spectroscopy (XPS). Fig. 3-6 compares the XPS spectra of the SEI layers formed under different electrolyte conditions. These analyses were performed after three cycles of Li plating and stripping with a capacity of 0.5 mAh cm^{-2} at 0.5 mA cm^{-2} . In the C 1s branch (Fig. 3-6a), the peaks observed at 290.3, 289.0, 286.8, and 285.0 can be assigned to the COOR, C=O, C–O–C, and C–C bonds, respectively, and the peaks related to the COOR, C=O, and C–O–C bonds are attributed particularly to the decomposition of DMC.^{44, 79} Based on this information, the more prominent COOR, C=O, and C–O–C peaks of 5.5 M-DMC and 2 M-DMC/BTFE indicate more significant decomposition of DMC in these electrolytes. In contrast, these peaks were pronouncedly suppressed with 2 M-DMC/1,2-dfBen and triple-DMC/1,2-dfBen, reflecting the weakened decomposition of DMC. These phenomena were further evidenced by the full-range XPS profiles; the former two electrolytes showed higher O-to-C atomic ratios than the latter two. In the F 1s branch (Fig. 3-6b), the 2 M-DMC/1,2-dfBen and triple-DMC/1,2-dfBen electrolytes exhibited higher LiF-to-S–F peak ratios (assigned to the peaks at 685.3 and 688.8 eV, respectively) compared to those of 5.5 M-DMC and 2 M-DMC/BTFE. Considering the similar linear scanning voltammetry (LSV) profiles of the different electrolytes, the above observation can be interpreted as indicating that the FSI[−] anions coordinated with Li ions as well as 1,2-

dfBen itself were both preferentially decomposed in contact with metallic Li during Li plating, leading to passivation of the Li metal by the LiF-rich SEI layer.

The different electrolyte conditions were further assessed in a full-cell configuration by pairing with a $\text{LiNi}_{0.5}\text{Co}_{0.2}\text{Mn}_{0.3}\text{O}_2$ (NCM523) cathode. The tests were conducted by using a $40\ \mu\text{m}$ -thick Li anode corresponding to $8\ \text{mAh cm}^{-2}$ that was paired with the cathode with an active material loading of $17\ \text{mg cm}^{-2}$ corresponding to $3\ \text{mAh cm}^{-2}$. We first carried out cyclic voltammetry (CV) in the potential range of 3.0–4.3 V at a scan rate of $1\ \text{mV s}^{-1}$ to see the overall redox behavior of the cathodes in the various electrolytes (Fig. 3-7). Notably, in the case of 2 M-DMC/BTFE and 2 M-DMC/1,2-dfBen, the reduction and oxidation peaks gradually decreased as a result of the corrosion of the aluminum current collectors caused by LiFSI salt.¹⁰⁵ By contrast, the cell with triple-DMC/1,2-dfBen exhibited stable CV cycles, similar to that with 1 M LiPF_6 in EC/DEC, indicating that the triple salt suppressed the aluminum corrosion effectively.^{103, 104} In addition, the XPS spectra of NCM523 cathodes after 15 cycles (Fig. 3-8) revealed that triple-DMC/1,2-dfBen contributed to the formation of a cathode electrolyte interphase (CEI) layer containing $-\text{CF}_3$ and LiF.

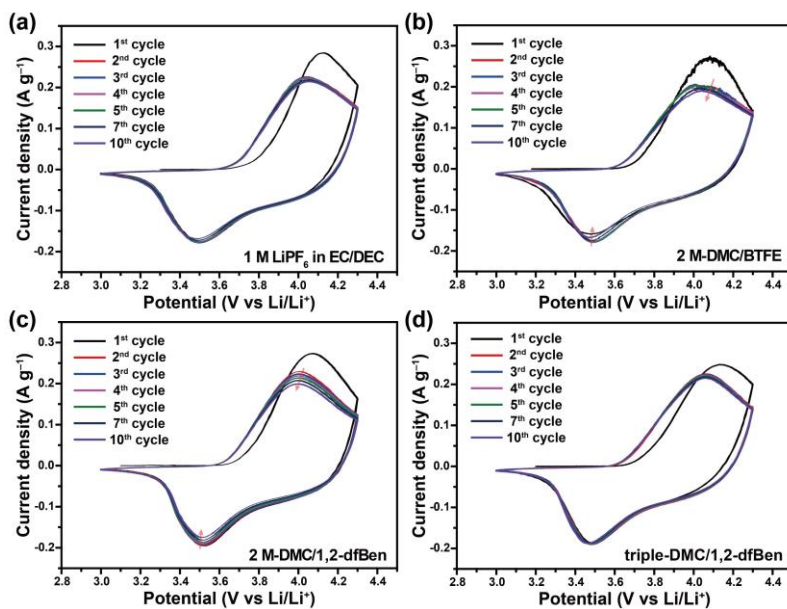


Fig. 3-7 Cyclic voltammetry profiles of NCM523 cathodes at a scan rate of $1\ \text{mV s}^{-1}$ with (a) 1 M LiPF_6 in EC/DEC, (b) 2 M-DMC/BTFE, (c) 2 M-DMC/1,2-dfBen, and (d) triple-DMC/1,2-dfBen.

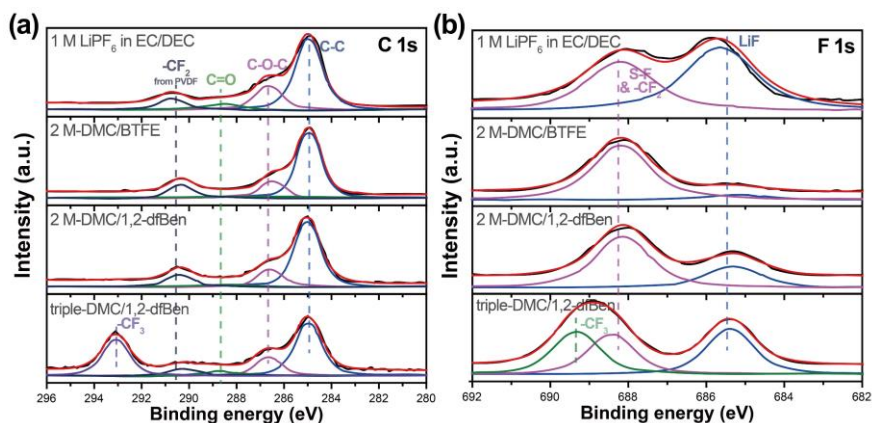


Fig. 3-8 XPS spectra of the NCM523 cathodes in the (a) C 1s and (b) F 1s branches after 15 cycles when different electrolytes are used.

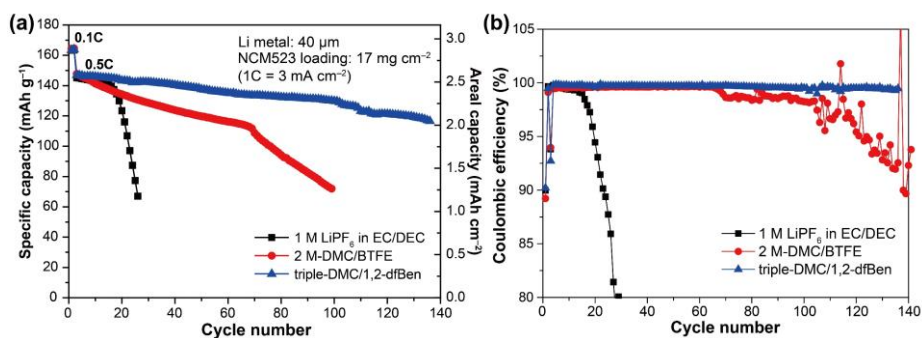


Fig. 3-9 (a) Cycling performance and (b) coulombic efficiencies of NCM523-Li full cells with different electrolytes. The mass loading of the active material in the cathode is 17 mg cm⁻², and the thickness of the Li foil in the anode is 40 μm.

Cycling tests were carried out by galvanostatically cycling the cells at 0.1C (1C = 3 mA cm⁻²) for the first two cycles and then at 0.5C for subsequent cycles (Fig. 3-9). The capacity of the cell with 1 M LiPF₆ in EC/DEC decreased abruptly after only 17 cycles, which is attributed to the depletion of Li metal. Although the cell with 2 M-DMC/BTFE maintained 111 mAh g⁻¹ for 70 cycles with a capacity fade rate of 0.42% per cycle, it decayed more rapidly for the next 30 cycles at a capacity fade rate of 1.5% per cycle. This degradation trend corresponded well with the CE results (Fig. 3-9b), which showed average values of 99.58% for the first 70 cycles and 98.60% for the next 30 cycles. These distinct periods of cyclic degradation led us to infer that the Li metal

was depleted at around the 70th cycle. Although 2 M-DMC/1,2-dfBen showed better cycling performance than that of 2 M-DMC/BTFE, the capacity fading of 2 M-DMC/1,2-dfBen was still substantial, particularly after 80 cycles presumably due to the Li depletion. In contrast, the cell with triple-DMC/1,2-dfBen was vastly superior in terms of maintaining the capacity, as it retained 130 mAh g⁻¹ after 100 cycles with a capacity fade rate of 0.14% per cycle, followed by 0.41% per cycle for the next 40 cycles. Furthermore, the average CE was 99.70% for the first 100 cycles and 99.47% for the next 40 cycles. These series of results imply that the given optimized electrolyte condition enables decent cycling performance even under full-cell conditions that are also practically viable.

3.3 Conclusion

The usefulness of a high salt concentration and LiF-rich SEI composition for Li metal anodes has settled as a consensus in the battery community. In this sense, 1,2-dfBen is remarkable as it realizes both the high-concentration effect and a LiF-rich SEI layer simultaneously. In fact, 1,2-dfBen is the first non-HFE diluent solvent for LHCEs and thus unfolds the promise of fluorinated aromatic compounds in relation to their LUMO energy levels, binding affinity with the Li ion, and fluorine-donating power. We also identified an optimal triple salt composition that assists with the formation of a LiF-rich SEI layer and prevents the corrosion of the aluminum current collector while maintaining the high-concentration effect even at a relatively low salt concentration of 2.02 M. The present investigation heightens the possibility of achieving the highly beneficial yet economically feasible high-concentration effect for emerging LMBs.

3.4 Experimental

3.4.1 Electrolyte preparation

Lithium bis(trifluoromethanesulfonyl)imide (99.95%), lithium hexafluorophosphate (99.99%), dimethyl carbonate (99%), bis(2,2,2-trifluoroethyl) ether (98%), methoxybenzene (anhydrous, 99.7%), (trifluoromethoxy)benzene (99%), benzene (anhydrous, 99.8%), fluorobenzene (99%), 1,2-difluorobenzene (98%), and 1,3-difluorobenzene (99%) were purchased from Sigma Aldrich. Lithium bis(fluorosulfonyl)imide (98.0%) was purchased from TCI Chemicals. Conventional electrolyte consisting of 1M lithium hexafluorophosphate in ethylene carbonate/diethyl carbonate (v/v=1/1) was purchased from PANAX ETEC. All the localized high-concentration electrolytes were prepared in solvent mixtures of dimethyl carbonate/diluent (v/v=3/7). All electrolytes were prepared in an argon-filled glove box.

3.4.2 Electrochemical measurements

For the full-cell measurements, the cathodes were prepared based on the following procedure. $\text{LiNi}_{0.5}\text{Co}_{0.2}\text{Mn}_{0.3}\text{O}_2$ (NCM523), super-P, and poly(vinylidene difluoride) (PVDF) were uniformly dispersed in *N*-methyl 2-pyrrolidone (NMP) in a weight ratio of 90:5:5. The well-mixed slurry was cast onto Al foil using the doctor blade technique. The cast electrodes were dried under vacuum at 80 °C for 12 h. The areal mass loading of the active material was 17 mg cm⁻². The electrochemical performance was characterized by preparing 2032 coin-type cells. The full-cells were composed of a Li metal anode with a thickness of 40 μm (Honjo Metal, Japan), a polypropylene separator with a thickness of 25 μm (Celgard 2400), and the NCM523 cathode, together with different electrolytes. Asymmetric cells consisted of a Cu foil electrode and Li metal counter electrode. The full-cells were assembled in an argon-filled glove box. Cyclic voltammetry (CV) measurements were performed at a scan rate of 1 mV s⁻¹. All of the electrochemical measurements were performed at 25 °C using a battery cycler (WBCS3000, Wonatech, South Korea)

3.4.3 Characterization

For all of the characterizations after electrochemical measurements, cells were disassembled in an argon-filled glove box, and the cycled Li metal was washed with DMC solvent and dried under vacuum for 3 h in a chamber connected to a glove box. The chemical compositions and bonding characteristics of the SEI layers were analyzed by XPS (Sigma Probe, Thermo VG Scientific, England) with a Mg K α line as the X-ray source. The Raman spectra of various electrolytes were recorded using a Raman spectrometer (DXR2xi, Thermo Fisher, USA). The morphologies of the Li metal electrodes were characterized by using field-emission SEM (JSM-7800F Prime, JEOL, Japan) at the National Center for Inter-University Research Facilities (NCIRF) at Seoul National University. For all characterizations, moisture and air contamination were avoided by using an airtight sample box during sample transfer.

3.4.4 DFT calculation

Geometry optimizations and molecular orbital energy calculations of selected solvents were performed without symmetry restriction using the B3LYP hybrid density functional implemented in the GAUSSIAN 09 software package.¹⁰⁶ The 6-31+G(d, p) basis sets were used for all the atoms. Frequency calculations of the same basis sets were conducted to determine the nature of a stationary point as the true local minimum. The geometry calculations were performed in gas phase to compare the trends of selected solvents.

Chapter 4. Triangular Phenanthrenequinone-based Macrocycle for Aluminum Batteries

4.1 Introduction

Climate change affects our everyday lives. A paradigm shift in the world's energy reliance from conventional fossil fuels to renewable energy has become inevitable. In this context, designing rechargeable batteries for large-scale applications, such as storing electricity generated from sustainable resources, has emerged as one of the major contemporary challenges in the energy industry.^{16, 107} Since the 1990s, lithium-ion batteries (LIBs), based on lithium-containing inorganic cathodes and graphite anodes, have met with stunning successes in applications associated with mobile electronic devices.^{108, 109} The overall performance of LIBs remains, however, unsatisfactory for renewable energy-storage applications because of their limited cycle life, safety, and relatively high cost.^{4, 110} It follows that next generation energy-storage devices need to satisfy very much higher standards than the current state-of-the-art LIBs. With this goal in mind, rechargeable aluminium batteries (ALBs) offer considerable promise. Aluminium is the third most abundant element (8.1 wt%) in the Earth's crust, after oxygen and silicon, and has one of the highest theoretical volumetric capacities (8056 mAh cm⁻³) on account of its multiple redox states.^{11, 111} It is worth noting that the development of ALBs has not reached an advanced stage yet. In particular, it has proved difficult to design electrode materials that can insert aluminium (complex) ions reversibly.¹⁰ Also, the number of currently available materials for use in electrochemically stable aluminium-based electrolytes is limited.¹¹²

Based on lessons learnt from numerous investigations¹¹³⁻¹¹⁵ of relationships between redox-active organic compounds and transition metals, we envisioned phenanthrenequinone-based compounds as promising ALB-active materials on account of their reversible redox nature¹¹⁶ and their susceptibility to form metal-ligand complexes with aluminium.^{117, 118} We hypothesised that phenanthrenequinone (PQ) derivatives stand a good chance of undergoing redox-reversible Al-complex ion

insertion and extraction as long as (i) PQ compounds do not dissolve in the electrolyte during battery cycling, (ii) a favourable Al-complex ion inserting structure is maintained, and (iii) the binding strength of reduced PQ derivatives with Al-complex ion is moderately strong, enabling electrochemical re-oxidation to the neutral state.

Herein, we demonstrate a class of active materials for ALBs, namely a redox-active macrocyclic compound, in which the redox-active units are covalently linked together to form a triangular constitution. From previous attempts at designing multi-valence rechargeable batteries,¹¹⁹⁻¹²¹ we envisioned that the formation of layered stacks of organic compounds would have a higher chance of inserting Al-complex ion than other architectures, particularly in wet electrolyte environments. In order to test this idea, we prepared a triangular macrocycle, namely, the phenanthrenequinone triangle (**PQ- Δ**) and confirmed the reversible insertion and extraction of cationic chloroaluminate. **PQ- Δ** showed a reversible specific capacity of 94 mAh g⁻¹ with a cyclability of up to 5000 cycles, most likely resulting from the sterically hindered constitution of the molecular triangle with sufficient flexibility that can accommodate the strain accompanied by chloroaluminate ion insertion. Furthermore, we fabricated a phenanthrenequinone triangle hybrid material (**PQ- Δ -HY**) by blending **PQ- Δ** with graphite flakes. This optimisation enabled the dual insertion of cationic and anionic chloroaluminates, increasing the specific capacity to 126 mAh g⁻¹ at 1.7 V vs Al/Al³⁺, along with other advantages such as enhanced conductivity and high loading capability. Our findings suggest that simple redox-active compounds with defined constitutional arrangements in order to achieve homogeneous stacking are crucial for ensuring the reversible insertion and extraction of chloroaluminate ions during the operation of ALBs.

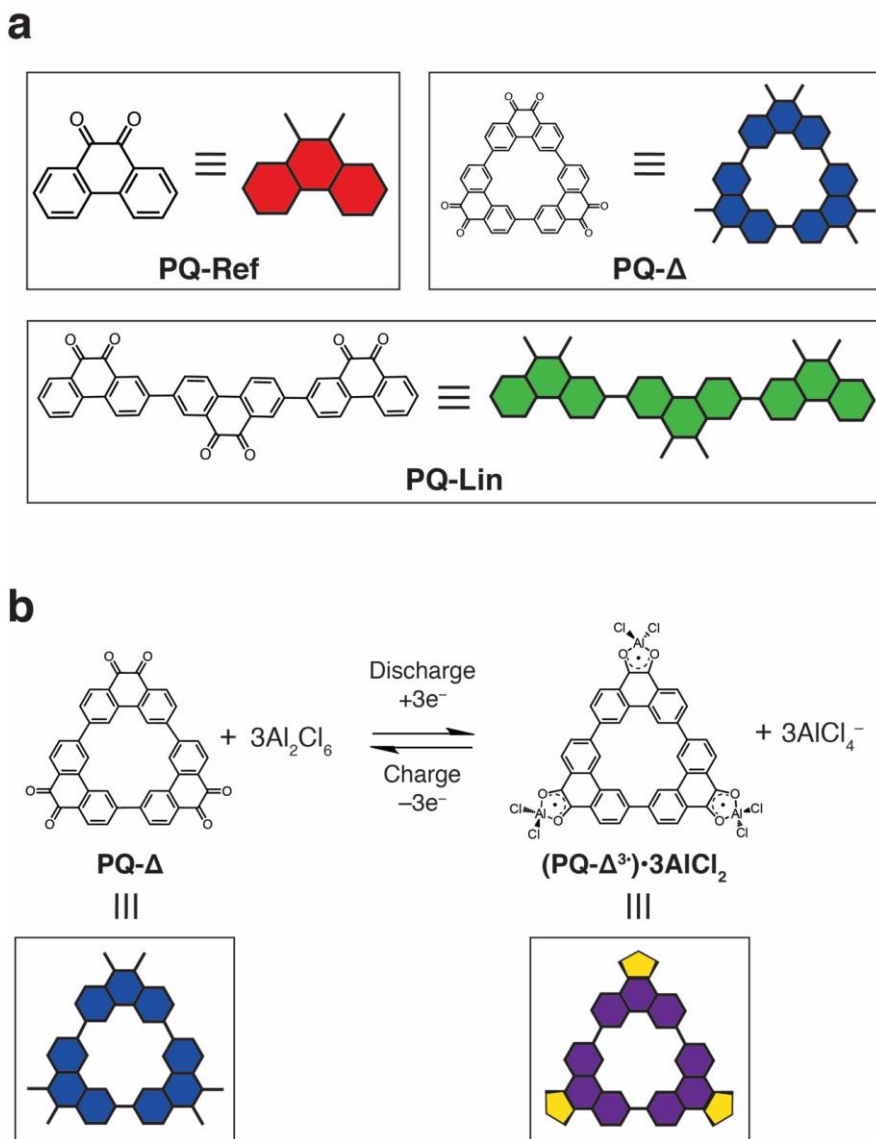


Fig. 4-1 Series of phenanthrenequinone (PQ) derivatives for rechargeable aluminium batteries (ALBs). (a) Structural formulae of three phenanthrenequinone compounds—the phenanthrenequinone monomer (**PQ-Ref**), the linear phenanthrenequinone trimer (**PQ-Lin**), and the phenanthrenequinone triangle (**PQ- Δ**). (b) Electrochemical redox chemistry of **PQ- Δ** (blue) and its schematic representation. Upon discharging, the macrocycle is reduced to its semiquinone state (**PQ- $\Delta^{3\bullet}$** , purple), followed by interacting with the cationic chloroaluminates (AlCl_2^+ , yellow), which were generated by the asymmetric cleavage of dialuminium hexachloride, resulting in the formation of the tetracoordinate complex, **(PQ- $\Delta^{3\bullet}$)** \cdot 3AlCl_2 .

4.2 Result and discussion

In an effort to achieve the reversible insertion and extraction of Al-complex ion, we explored rigid and geometrically planar PQ-based compounds (Fig. 4-1a): **PQ-Δ**, previously reported by Müllen and co-workers,¹²² captured our attention. Briefly, PQ was brominated in the presence of elemental bromine, 2,2'-bipyridine, and benzyl peroxide in refluxing nitrobenzene, resulting in the generation of 3,6-dibromophenanthrenequinone which was then subjected to a Yamamoto homocoupling process, using bis(cyclooctadiene)nickel as the reducing agent. The crude product was purified by Soxhlet extraction and **PQ-Δ** was isolated in 44% yield.

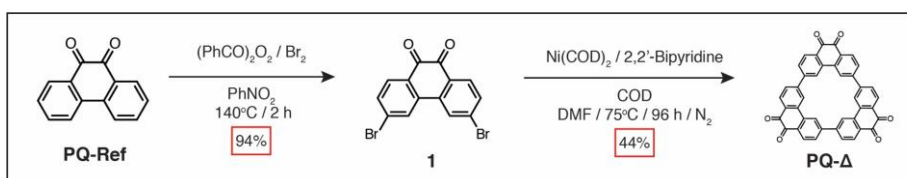


Fig. 4-2 | Synthesis of 3,6-dibromophenanthrenequinone and phenanthrenequinone triangle (**PQ-Δ**).

In an effort to investigate the relationship between molecular geometry and ALB performance, we also prepared the phenanthrenequinone monomer (**PQ-Ref**) and linear phenanthrenequinone trimer (**PQ-Lin**). **PQ-Ref** was purchased from a commercial vendor and used as received. **PQ-Lin** was synthesised by Suzuki coupling in a 1:2 molar ratio of a boronic acid ester and the iodide precursors of PQ, respectively.

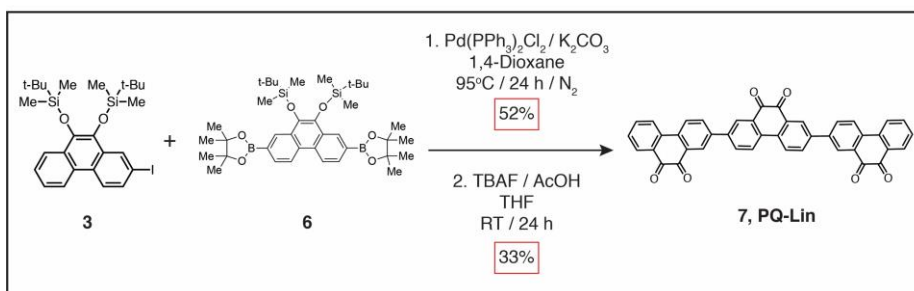


Fig. 4-3 | Synthesis of **PQ-Lin** through Suzuki coupling.

As mentioned in a previous report, **PQ- Δ** is insoluble in all common deuterated NMR solvents. Therefore, we conducted ^{13}C CP MAS solid-state NMR measurements and confirmed the presence of the expected aromatic peaks for **PQ- Δ** . We also performed MALDI-TOF experiments using a 1:1 mixture of 2,5-dihydroxybenzoic acid and α -cyano-4-hydroxy-cinnamic acid as a matrix, and our data matched the theoretical and previously reported values.¹²² The TGA profile of **PQ- Δ** reveals (Fig. 4-4a) that the macrocycle does not have a clear melting point, while the FTIR absorption at 1670 cm^{-1} matches (Fig. 4-4b) well with that of a quinone reference peak.

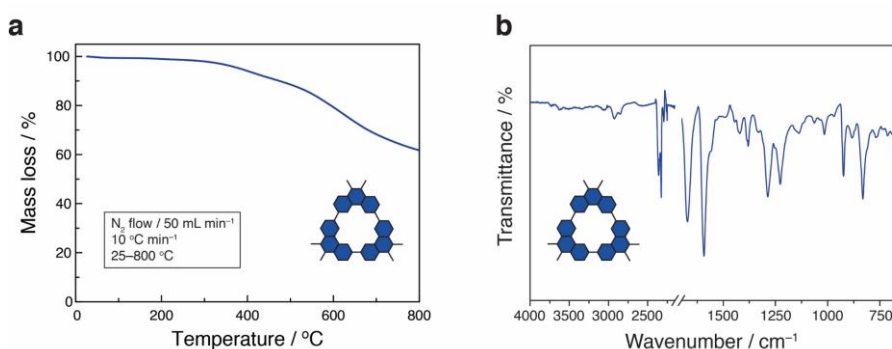


Fig. 4-4 | (a) TGA Curve and (b) FT-IR spectrum of **PQ- Δ** .

Notwithstanding many efforts, we could not produce a sufficiently high quality single crystal of **PQ- Δ** because of its poor solubility in all solvents. And so we turned our attention to powder X-ray diffraction (PXRD) and confirmed the crystallinity of all three compounds. The diffraction peak of **PQ-Ref** indicates (Fig. 4-5a) the highly crystalline phase, whereas the **PQ-Lin** diffraction peak (Fig. 4-5b) become broadened, on account of the rotational flexibility associated with its linear constitution. It transpires that **PQ- Δ** , which exhibits (Fig. 4-5c) one broad peak around $2\theta = 22\text{--}28^\circ$, makes it distinct from the other two PQ derivatives. This broad diffraction peak implies the presence of an amorphous layered structure,^{123, 124} resulting from the stacking of the rigid and planar molecular geometry.¹²⁵

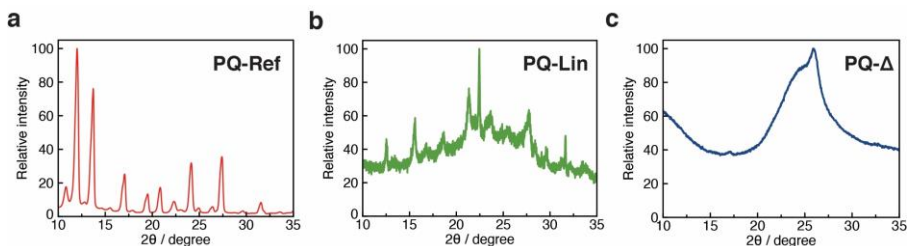


Fig. 4-5 | Powder X-ray diffraction results of (a) PQ-Ref, (b) PQ-Lin, and (c) PQ-Δ.

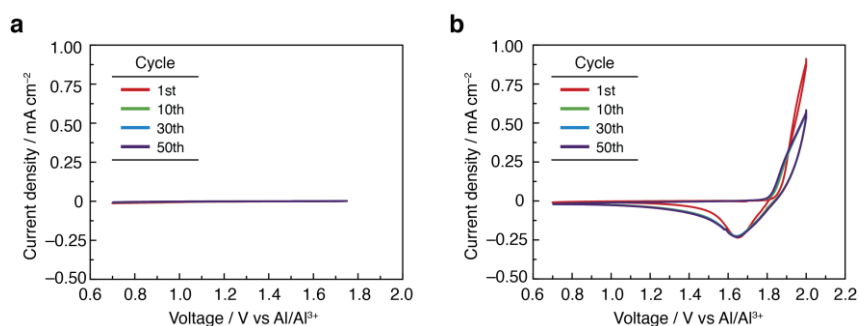


Fig. 4-6 | Cyclic voltammetry (CV) of pyrolytic graphite-based current collector at (a) 0.7–1.75 V and (b) 0.7–2.0 V voltage range.

A modified Swagelok-type two-electrode cell⁹ was used for making electrochemical measurements on ALBs. Detailed electrode preparations and cell configurations are described in the Methods section. Hereafter, all potentials are based on Al/Al^{3+} (-0.7 V vs NHE, in $\text{AlCl}_3/\text{EMImCl} = 1.3$) redox couple,¹²⁶ unless otherwise stated. Prior to analysing the redox properties of the PQ derivatives, we confirmed (Fig. 4-6a) the stable voltage range of the imidazolium chloride electrolyte and the graphite current collector by conducting cyclic voltammetry (CV) without any active materials. During the CV measurements we did not identify any noticeable redox peaks in the voltage range between 0.70–1.75 V, indicating a stable electrochemical cell configuration for ALB characterisation. When the voltage range was increased (Fig. 4-6b) up to 2.00 V, however, new oxidation and reduction peaks appeared around 1.90 and 1.70 V, respectively, an observation which can most likely be attributed to the insertion of anionic chloroaluminates inside the graphite current collector. We also

confirm that the binder and conductive agent used in the electrodes do not contribute to their specific capacities.

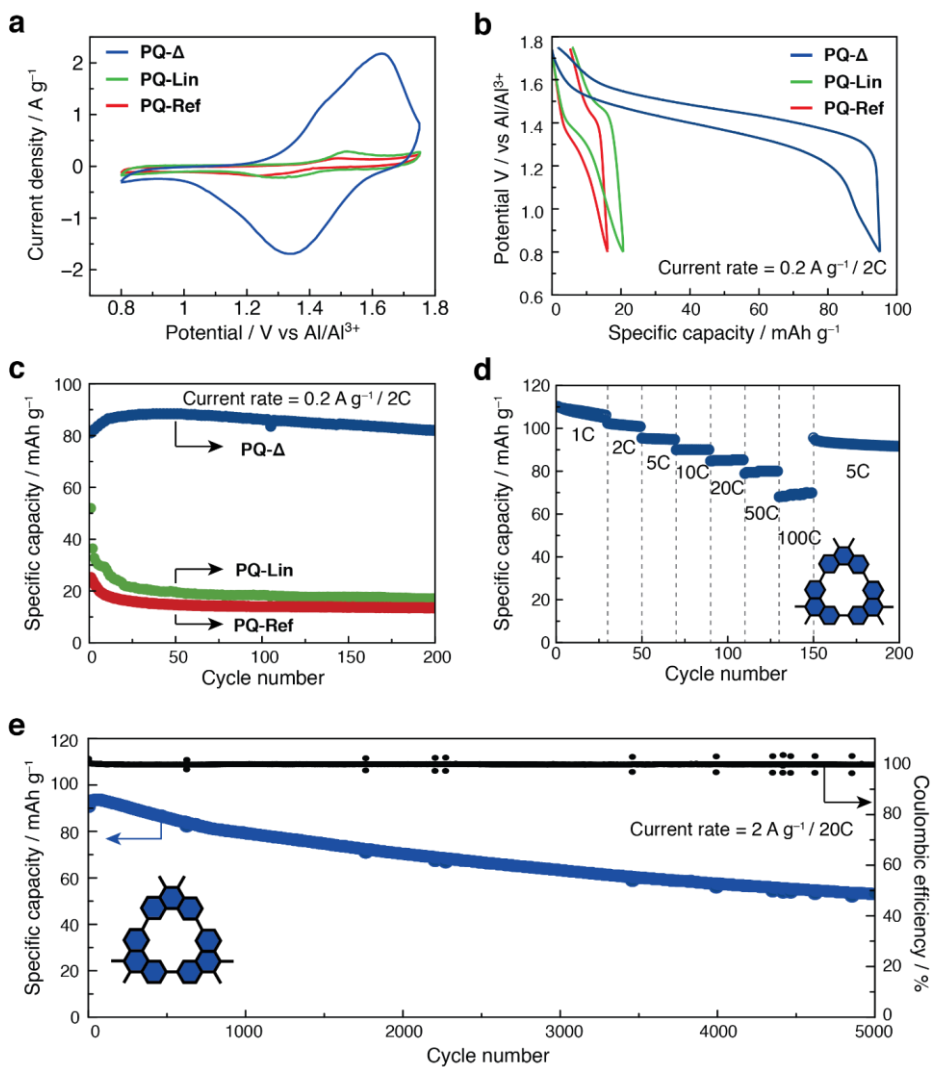


Fig. 4-7 | Electrochemical measurements of PQ derivatives. All of the electrochemical measurements were performed in the voltage range of 0.8–1.75 V vs Al/Al³⁺. Compound colour code: **PQ-Ref** (Red), **PQ-Lin** (green), and **PQ-Δ** (blue). (a) Cyclic voltammetry of each of the PQ derivatives at a scan rate of 5 mV s⁻¹. (b) Comparison of the galvanostatic voltage profiles, and (c) cycling performances of PQ derivatives at a current rate of 0.2 A g⁻¹ (= 2C). (d) Rate capability measurement of **PQ-Δ**. The initial 30 cycles were measured at 1C and the current rate was increased every 20 cycles up to 100C. (e) Extended cycling test of **PQ-Δ** at a current rate of 2 A g⁻¹ (= 20C). The Coulombic efficiency is defined on the right axis.

Based on the established stable voltage range for the electrolyte and current collector in the ALB environment, we subsequently carried out CV measurements on **PQ-Ref**, **PQ-Lin** and **PQ-Δ** in the voltage range of 0.70–1.75 V. All PQ derivatives exhibited (Fig. 4-7a) one pair of reversible reduction and oxidation peaks around 1.3 and 1.5 V, respectively. It is worth mentioning that the current density of **PQ-Ref** and **PQ-Lin** decreased gradually with each cycle (Fig. 4-8a and b), an observation which we ascribe to the gradual dissolution (Supplementary Fig. 11) of the active materials in the electrolyte. For **PQ-Δ**, however, the current density increased gradually (Fig. 4-8c) during extended cycles.

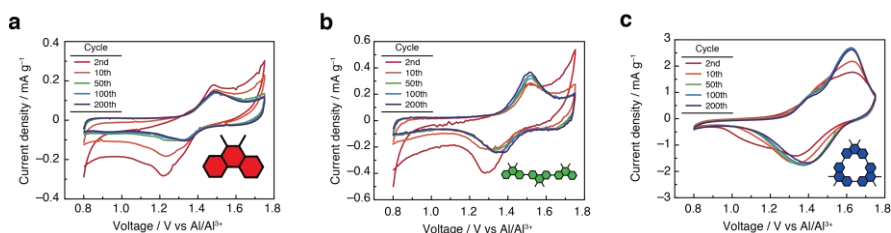


Fig. 4-8 | CV results of (a) **PQ-Ref**, (b) **PQ-Lin**, and (c) **PQ-Δ** up to 200 cycles at 10 mV s^{-1} scan rate.

This current density increase could be a result of microstructural rearrangements in **PQ-Δ**, which increases the activity of **PQ-Δ** during cycles.¹²⁷ After observing the reversible redox nature of PQ derivatives in the ALB system, we carried out galvanostatic measurements of **PQ-Ref**, **PQ-Lin**, and **PQ-Δ** as the active materials of ALBs. Notably, all galvanostatic measurements were preceded by an activation process consisting of 50 CV cycles at 5.0 mV s^{-1} . Theoretical specific capacities were calculated based on a 1:1 ratio of PQ:chloroaluminate, while the charge and discharge processes refer to the oxidation (Al-complex ion extraction) and reduction (Al-complex ion insertion), respectively. At a current rate of 0.2 A g^{-1} , **PQ-Ref** and **PQ-Lin** showed (Fig. 4-7b) a single smooth plateau around 1.2–1.6 V for both discharging and charging, with specific capacities of 15 and 20 mAh g^{-1} , respectively. In the case of **PQ-Δ**, the triangular macrocycle displayed a similar voltage profile with the substantially increased reversible capacity of 94 mAh g^{-1} under identical measurement conditions. It is worth mentioning that the specific capacities obtained correspond to one-electron

transfer per Al-complex ion, not three electrons. Previous reports¹²⁸ have revealed that soluble halides of group 13 elements undergo asymmetric cleavage in solution, generating $[\text{MX}_2]^+$ and $[\text{MX}_4]^-$ ions. Thereafter, the cationic complex reacts with the radical anion of the PQ, resulting in a single electron transfer.^{129, 130} This observation raises the possibility of $\text{PQ-}\Delta^{3-}$ interacting (Fig. 4-1b) also with the cationic aluminium complex (AlCl_2^+), comprising the stable tetracoordinate centres ($(\text{PQ-}\Delta^{3-})\cdot 3\text{AlCl}_2$) with both quinone oxygens chelating one aluminium centre. Because of the formation of a strong cationic aluminium complex, we suspect that PQ derivatives cannot be fully reduced to a dianionic state in the ALB system, an observation which is consistent (Fig. 4-7a) with the CV results. More recent research from the battery standpoint by Kravchuk *et al.*¹³¹ has also confirmed that bare aluminium-ion does not directly engage in insertion by means of electrochemical redox in an imidazolium chloride-based electrolyte environment, but rather chloroaluminate anions, such as AlCl_4^- and Al_2Cl_7^- , express the redox processes. Our electrochemical results suggest strongly that the cationic chloroaluminate migrates through the $\text{PQ-}\Delta^{3-}$, therefore enabling reversible insertion and extraction (Fig. 4-1b). The use of the cationic carrier ions in the cathode reactions is more beneficial in energy density that takes the amount of electrolyte into account, compared to typical Al-complex ion batteries where anionic carrier ions are used for cathode reactions. When all three compounds were subjected to galvanostatic cycling tests at a current rate of 0.2 A g^{-1} (Fig. 4-7b and c), **PQ- Δ** displayed an excellent capacity retention of 82 mAh g^{-1} after 200 cycles, corresponding to 100.9% retention with respect to that observed in the first cycle. This specific capacity, after 200 cycles, is compared with 17 mAh g^{-1} for **PQ-Lin** and 13 mAh g^{-1} for **PQ-Ref**. This substantial capacity retention of **PQ- Δ** suggests that the macrocyclic constitution restricts the rotational possibility between neighbouring PQ moieties under these electrolyte conditions which minimises the solvation event in the presence of the battery electrolyte.¹³² We have also investigated the ALB performance of **PQ- Δ** and found that it displays (Fig. 4-7d) an excellent rate capability, which could originate from its conjugated molecular constitution. **PQ- Δ** exhibited a specific capacity of 110 mAh g^{-1} at a current rate of 0.1 A g^{-1} . When the current rate was increased up to 100 times (10 A g^{-1}), a specific capacity of 70 mAh g^{-1} was still observed, indicating

the extraordinary rate capability of **PQ-Δ**. This rate performance is attributed to well-defined ion channels along the π - π stacked superstructure of **PQ-Δ**. Also, **PQ-Δ** maintained excellent capacity retention (95 mAh g⁻¹) when the current rate was decreased back to 0.5 A g⁻¹. Since the cycle life is of primary importance for large-scale energy storage applications, we then subjected **PQ-Δ** to extensive cycling performance testing (Fig. 4-7e). The macrocycle preserved 53 mAh g⁻¹ after 5000 cycles, corresponding to a capacity fade of only 0.0082% for each cycle. This remarkable cycling performance highlights the robustness of the molecular triangle and the reversible accessibility of cationic chloroaluminate throughout galvanostatic cycling.

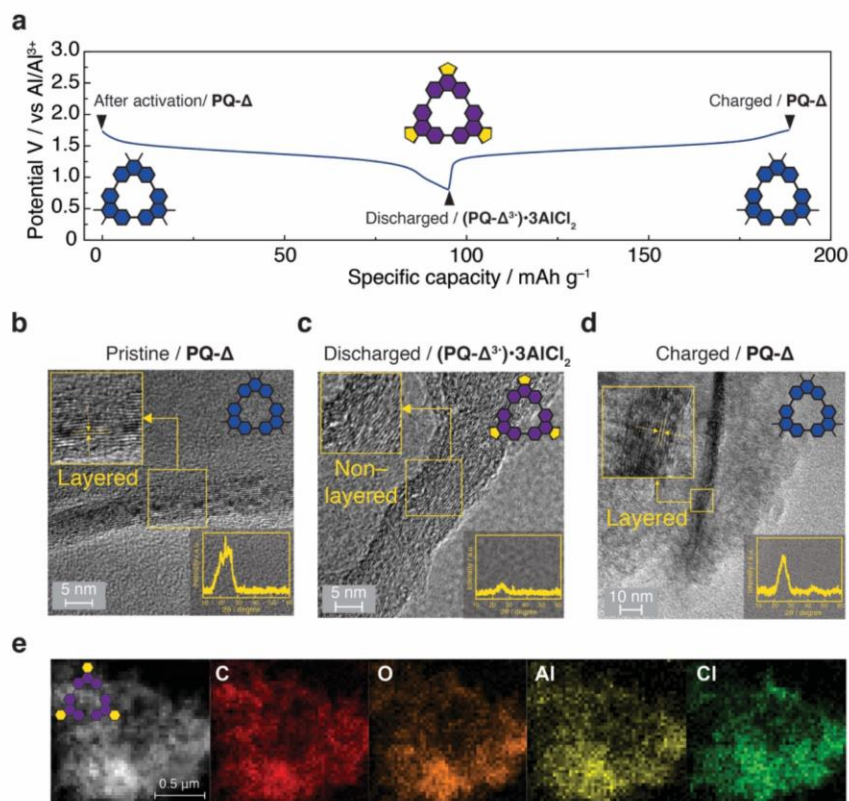


Fig. 4-9 | Ex-situ characterisation of PQ-Δ. (a) Galvanostatic voltage profile of **PQ-Δ** and its schematic illustration for each *ex-situ* state. (b-d) Transmission electron microscopic (TEM) images of *ex-situ* electrodes and corresponding (inset) powder X-ray diffraction (PXRD) traces. (e) Energy-dispersive X-ray spectroscopy of the discharged state sample—carbon (red), oxygen (orange), aluminium (yellow), and chlorine (green).

In order to assess the insertion and extraction of chloroaluminate in **PQ- Δ** during battery cycling, we analysed **PQ- Δ** electrodes by using both *ex-situ* PXRD and transmission electron microscopy (TEM). Detailed *ex-situ* sample preparations are described in the Methods section. All of the *ex-situ* analysis samples were collected after neutral state, charging or discharging, followed by disassembling inside of the glove box. The galvanostatic voltage profile of **PQ- Δ** , as well as the schematic for each *ex-situ* state is illustrated in Fig. 4-9a. According to PXRD analysis, the amorphous layered superstructure of **PQ- Δ** is carried over into the battery electrode fabrication. We observed once again in the electrode material a diffraction peak around $2\theta = 16\text{--}28^\circ$, which corresponds (inset in Fig. 4-9b) to a layer-to-layer distance of 0.36 nm. This layered superstructure (Fig. 4-9b) of pristine **PQ- Δ** was confirmed by TEM analysis. In the discharged state, *ex-situ* PXRD diffraction showed (inset in Fig. 4-9c) peak broadening as a result of the insertion of chloroaluminate ions between the **PQ- Δ** layers, causing (Fig. 4-9c) physical distortion of the stacked superstructure.¹³³ As indicated by PXRD diffraction analysis (inset in Fig. 4-9d) that recovered the peak around $2\theta = 22\text{--}28^\circ$, the stacking structure (Fig. 4-9d) was largely restored to its neutral state, resulting in the extraction of chloroaluminate from the electrode. Furthermore, we conducted time-of-flight secondary ion mass spectrometry (ToF-SIMS) on the discharged electrode along with energy-dispersive X-ray spectroscopy (EDX), in order to investigate the elemental composition of the discharged **PQ- Δ** .

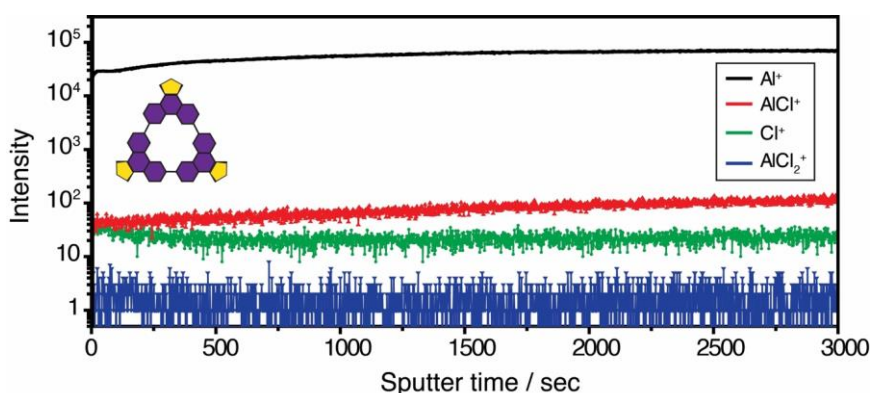


Fig. 4-10 | ToF-SIMS spectra of the discharged **PQ- Δ** electrode.

The mass spectrum of the discharged electrode exhibits (Fig. 4-10) the signal corresponding to cationic chloroaluminates, whereas EDX verifies (Fig. 4-9e) the presence of both aluminium and chlorine. The Al-to-Cl peak intensity ratios (average value = 1.83) obtained from various spots on the EDX map support the charge storage mechanism involving AlCl_2^+ . These two analytic techniques taken together make it reasonable to adopt the insertion of AlCl_2^+ toward **PQ- Δ** electrode. In addition, we performed *ex-situ* X-ray photoelectron spectroscopy (XPS) analysis on the discharged electrode. This analysis indicates (Fig. 4-11) that the O 1s edge shifted to a lower energy after discharging on account of the decreased oxidation state of the quinone group. After charging, the O 1s edge was restored to its pristine state. Taken together, *ex-situ* studies of **PQ- Δ** provide a valuable insight into the reversible insertion and extraction of chloroaluminate within the wet electrolyte environment.

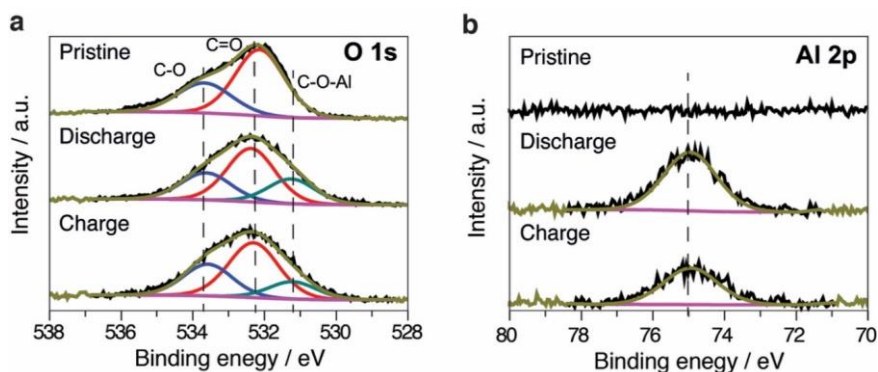


Fig. 4-11 | XPS Spectra of pristine, discharged, and charged **PQ- Δ** electrodes in the regions of (a) O 1s and (b) Al 2p.

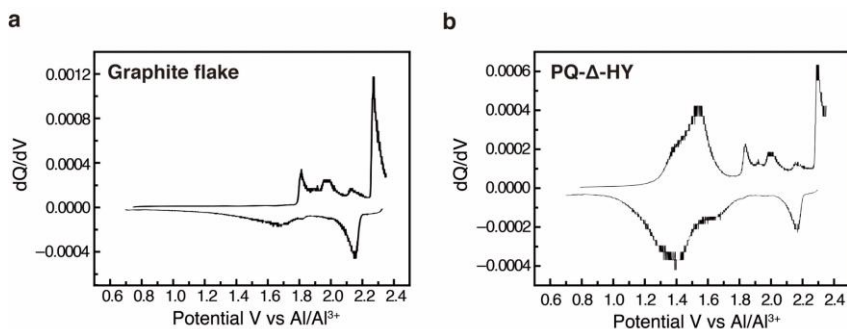


Fig. 4-12 | Voltage versus differential capacity plot of (a) graphite flake and (b) **PQ- Δ -HY**.

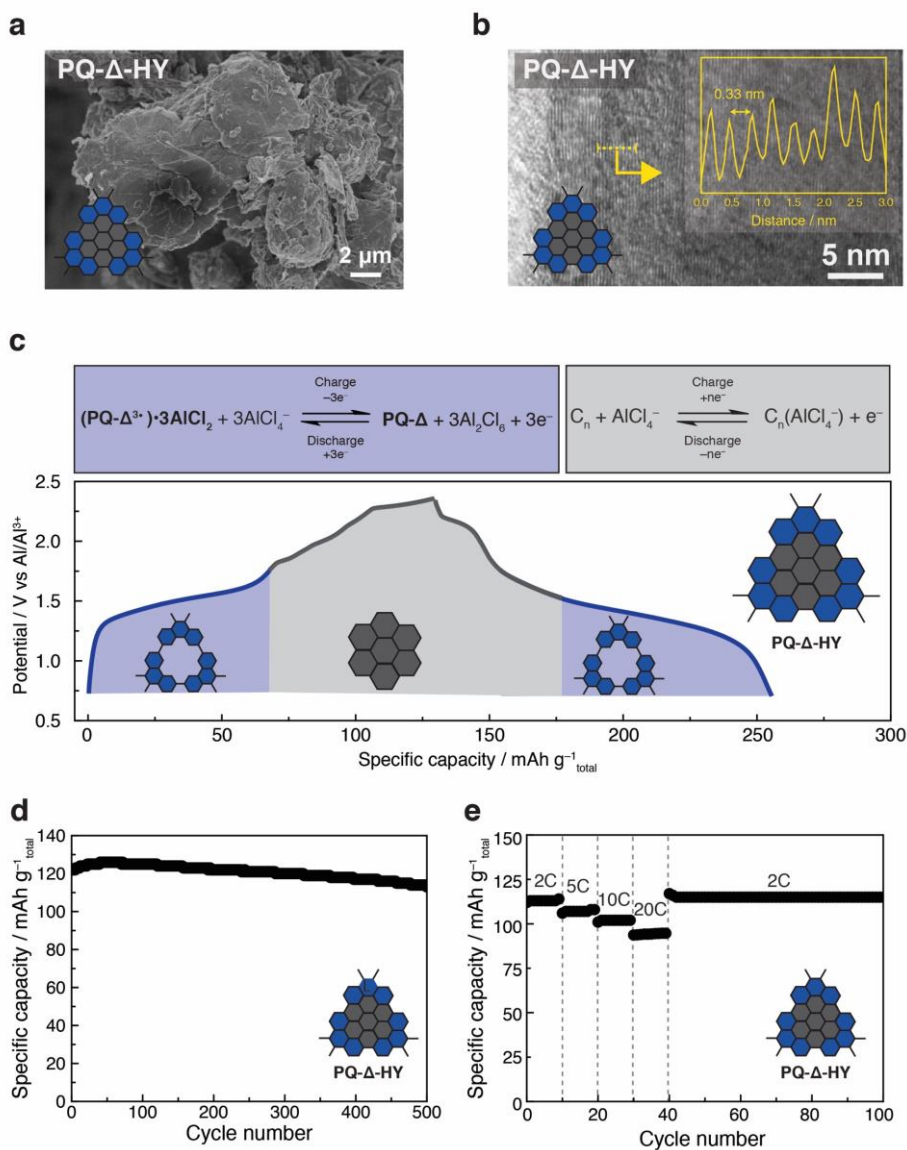


Fig. 4-13 | Fabrication of the graphite flake-blended phenanthrenequinone triangle hybrid (PQ- Δ -HY) and its electrochemical performance. Equal weight (1:1 w/w) of PQ- Δ and graphite flakes were used to fabricate the PQ- Δ -HY. (a-b) SEM and TEM images which characterise the microstructures. (c) Galvanostatic voltage profile of PQ- Δ -HY and its electrochemical redox schematic. Specific energy contributed from PQ- Δ and graphite flakes are represented in blue and grey colour, respectively. (d) Cycling performance of PQ- Δ -HY at the current rate of 0.2 A g⁻¹ (= 2C). (e) Rate capability measurement of PQ- Δ -HY.

The exceptional cyclability of **PQ-Δ** as the active material for ALBs, encouraged us to enhance its feasibility in a practical electrode setting by designing a hybrid electrode with graphite flakes. In previous reports, Dai *et al.*⁹ demonstrated a graphite flake-based, ALB showing excellent cyclability and power capability. Recently, Kravchyk *et al.*¹³¹ investigated the detailed mechanism of chloroaluminate anion insertion into graphite flakes. Noticeably, we recognised (Fig. 4-12) the redox potential differences between **PQ-Δ** (1.4 V vs Al/Al³⁺) and graphite flakes (1.8 V vs Al/Al³⁺), attributed to the different types of chloroaluminate ions engaged in each compound. Thus, by taking advantage of the redox potential differences and the planar geometry of **PQ-Δ**, we have fabricated a graphite flake-blended phenanthrenequinone triangle hybrid (**PQ-Δ-HY**) electrode. The highlight of this hybrid composition is that the graphite flakes, not only increase electronic conductivity as the conductive agent, but also serve as the active material along with **PQ-Δ** in the higher voltage range. It is worth noting that the exclusive use of redox-active organic compounds is usually impractical in high-loading electrodes because of their poor electronic conductivity and unstable stacking architecture. In order to overcome the insufficient electronic conductivity, organic-based electrodes frequently require a considerable amount of conductive carbon filler, such as carbon black,¹³⁴ carbon nanotubes,¹³⁵ or graphene.¹³⁶ While adding carbon fillers apparently enhances the conductivity of the electrode, it decreases the energy density of the battery cell on account of the small active mass content. Moreover, addition of carbon fillers does not resolve the issue of limited electrode loadings. In our investigation, **PQ-Δ-HY** was prepared by sonicating an equal molar weight of **PQ-Δ** and graphite flake using *N*-methyl-2-pyrrolidone as the solvent. Detailed electrode preparation procedures are described in the Methods section. The formation of a **PQ-Δ-HY** superstructure was confirmed by scanning electron microscopy (SEM, Fig. 4-13a) and TEM (Fig. 4-13b), indicating the homogeneous stacking of **PQ-Δ** and graphite flakes. For the control experiment, we attempted to fabricate the hybrid electrode using **PQ-Ref** and graphite flakes. We could not, however, achieve a similar structure and morphology, implying the importance of the constitution and geometry of the molecules. The electrochemical behaviour of **PQ-Δ-HY** displays a unique combination of **PQ-Δ** and graphite flakes, which is similar to the previously

reported^{137, 138} bipolar battery system. From the voltage versus the differential capacity plot (Fig. 4-12), the oxidation and reduction peaks are confirmed at 1.55, 1.83–2.15 V and 1.40, 2.15 V, respectively. These multiple redox peaks can be attributed to the co-existence of **PQ-Δ** and graphite flakes within a single electrode, and the potential values are consistent with our earlier results (**PQ-Δ**) and previous graphite flake reports.¹³⁹ We have confirmed (Fig. 4-13c) the two-stage redox behaviour in galvanostatic measurements of **PQ-Δ-HY**. **PQ-Δ** exists in the reduced form of **(PQ-Δ³⁺)•3AlCl₂** in its fully discharged state (0.75 V), while the graphite flakes are present in their neutral state (C_n). For reference, the specific capacities of **PQ-Δ-HY** were calculated based on the weight of both **PQ-Δ** and graphite flake for the electrochemical evaluation of **PQ-Δ-HY**. Upon charging, oxidation of **(PQ-Δ³⁺)•3AlCl₂** reveals one smooth plateau in the range of 0.75–1.75 V, with a specific capacity of 68 mAh g⁻¹_{total}. Additionally, **PQ-Δ-HY** could charge up to 2.35 V, through the oxidation of the graphite flakes, accompanied by the insertion of AlCl₄⁻, with the total specific capacity reaching 130 mAh g⁻¹_{total}. During discharge, this multi-step oxidation process is reversed. Notably, this specific capacity of 130 mAh g⁻¹_{total} is greater than those of individual **PQ-Δ-HY** and graphite (110 and 80 mAh g⁻¹, respectively). This unexpected result can be explained by the fact that enhanced electronic conductivity in the **PQ-Δ-HY** electrode by the integration of the graphite increases the specific capacity of **PQ-Δ**. In fact, in the **PQ-Δ-HY** composite electrode, the capacity contributions at discharge from **PQ-Δ** and graphite were found to be 140 and 90 mAh g⁻¹, respectively, according to the differential capacity (dQ/dV) profile of **PQ-Δ-HY** (Fig. 4-12). Remarkably, the observed 140 mAh g⁻¹ corresponds to the theoretical capacity of **PQ-Δ**, thus verifying the importance of electronic conductivity for the electrochemical activity of **PQ-Δ**. The cycling performance test of **PQ-Δ-HY** was also carried out (Fig. 4-13d) and again demonstrated excellent capacity retention, as 94% (114 mAh g⁻¹_{total}) of capacity was preserved after 500 cycles. We conducted (Fig. 4-13e) galvanostatic measurements by increasing the current rates, where **PQ-Δ-HY** exhibited excellent rate capability. When the initial current rate (0.2 A g⁻¹) was increased 2.5, 5, and 10 times, the hybrid electrode exhibited 94, 83, and 81%, respectively, of the initial specific capacity. In addition, we calculated specific energy and power, based on the total weight of

electrode and electrolyte. The specific energy value is 69 or 32% higher than singularly composed electrodes of either the graphite flakes or **PQ-Δ**, demonstrating remarkable advances with high practical impact.

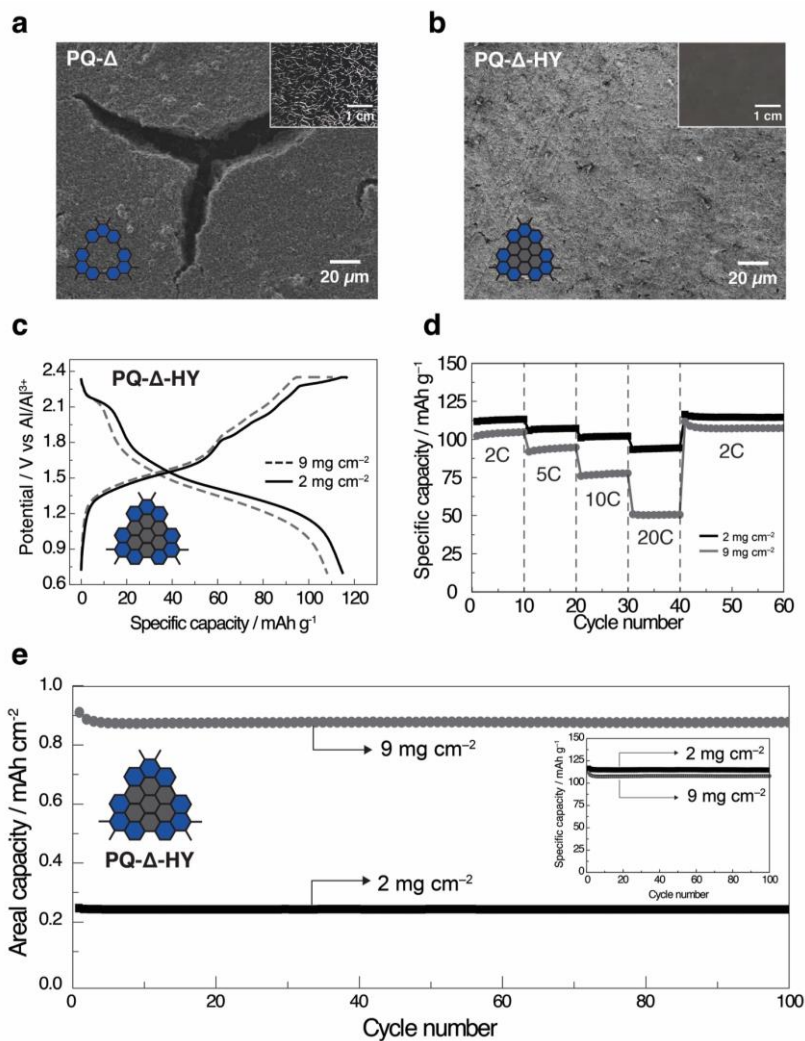


Fig. 4-14 | Mechanical stability and electrochemical performance of the hybrid electrode. (a-b) SEM images and digital photographs (insets) of **PQ-Δ** and **PQ-Δ-HY** electrodes at their pristine states. The areal loadings of the active materials in **a** and **b** are 2 and 9 mg cm⁻², respectively. The electrode compositions in **a** and **b** are **PQ-Δ**: Denka black: PVDF = 4: 5: 1 and **PQ-Δ-HY**: graphite: Denka black: PVDF = 4: 4: 1: 1, respectively. (c) Galvanostatic voltage profiles and (d) rate capability measurement of **PQ-Δ-HY** electrodes with different mass loadings of 2 and 9 mg cm⁻² at 0.1 A g⁻¹. (e) Cycling performance of the same electrodes at a current rate of 0.2 A g⁻¹ (=2C).

One challenge with organic electrode materials lies in increasing substantially (i) their weight portion and (ii) the areal loading of the electrode. In order to appreciate the impact of the graphite integration in **PQ- Δ -HY** with respect to these aspects, we fabricated **PQ- Δ** and **PQ- Δ -HY** electrodes by means of a conventional casting process and checked their morphologies. In the case of **PQ- Δ** electrodes containing 50 wt% Denka black, the electrodes suffered from crack formation and peel-off during the drying process in the electrode fabrication, even at an active mass loading of 2 mg cm^{-2} , an observation which can be ascribed¹⁴⁰ to significant generation of stress in stacking **PQ- Δ** . This phenomenon can also be interpreted in a way that the stress is not well distributed (Fig. 4-14a) through conductive carbon fillers. With an increased portion of **PQ- Δ** (i.e., > 40 wt%), the peeling issue of the electrode becomes more serious because of increased stress generation along the **PQ- Δ** stack.^{141, 142} By contrast, even at an areal loading of 9 mg cm^{-2} , **PQ- Δ -HY** electrodes were able to maintain (Fig. 4-14b) their integrity by co-stacking of graphite flakes and **PQ- Δ** during the same drying process. With the areal loading of 9 mg cm^{-2} , **PQ- Δ -HY** electrode achieved (Fig. 4-14c) a capacity of $110 \text{ mAh g}^{-1}_{\text{total}}$ at 0.1 A g^{-1} . When the current rate was increased by 20 times (2 A g^{-1}) for this electrode, a specific capacity of $51 \text{ mAh g}^{-1}_{\text{total}}$ was still preserved, indicating (Fig. 4-14d) the excellent rate capability of **PQ- Δ -HY** electrodes. This rate performance can be attributed to the well distributed graphite in **PQ- Δ -HY** as a result of π - π interactions between **PQ- Δ** and graphite which facilitates efficient electron transport. **PQ- Δ -HY** electrodes with a loading of 9 mg cm^{-2} also showed (Fig. 4-14e) good cyclability, as 96% (108 mAh g^{-1}) of the initial capacity was preserved after 100 cycles.

4.3 Conclusion

In summary, we have prepared three phenanthrenequinone derivatives—a monomer, a linear trimer, and a molecular triangle—as active materials for emerging ALBs and explored their structure-performance relationships. While all three compounds share similar redox potentials, we have observed that the triangular disposition of the redox-active units influences very strongly the accessibility of chloroaluminate ions, as well as the solubility of the triangular molecules. Most notably, the rigid triangular macrocycle increases the specific capacity and the cyclability dramatically, as a consequence of its layered architecture and the minimisation of solvent effects. In addition, fabricating the hybrid electrode with graphite flakes overcomes significantly the inherently low electronic conductivity and limited areal loading of conventional organic electrodes, enabling the bipolar storage of anions and cations to increase the specific capacity. In the future development of affordable large-scale energy storage systems, we suspect that other redox-active organic molecules with well-defined geometries will find use as active materials in ALBs.

4.4 Experimental

4.4.1 *Materials preparation and characterization*

Starting materials and reagents were purchased from commercial suppliers (Sigma Aldrich, Fisher Scientific or Tokyo Chemical Industry) and used without further purification. All reactions were performed under a nitrogen atmosphere, using anhydrous solvents unless otherwise stated. The crude reaction mixture was separated by silica gel column chromatography or on a Teledyne Isco Combiflash RF 200 system. Solution and solid-state nuclear magnetic resonance (NMR) spectra were recorded on Bruker Avance III 500 MHz and Varian VNMRS 400 MHz spectrometers, respectively, with working frequencies of 500 MHz (^1H nuclei), 125 MHz (^{13}C nuclei), and 100 MHz (^{13}C CP MAS solid-state). All chemical shifts are reported in ppm with reference to deuterated chloroform (CDCl_3 , $\delta_{\text{H}} = 7.26$ and $\delta_{\text{C}} = 77.2$ ppm). High-resolution mass spectra (HRMS) were performed on an Agilent 6210 Time of Flight (TOF) LC-MS, using an electrospray ionization (ESI) source. MALDI-TOF was carried out on a Bruker Autoflex III spectrometer using a 1:1 mixture of 2,5-dihydroxybenzoic acid and α -cyano-4-hydroxycinnamic acid as a matrix. Morphological changes in battery electrodes were characterised by field-emission scanning electron microscopy (FE-SEM, S-4800, Hitachi) and ultra-high resolution SEM (Magellan 400, FEI). Elemental mapping of electrode surfaces was carried out by energy-dispersive X-ray spectroscopy (EDX). Powder X-ray diffraction (PXRD) profiles of the phenanthrenequinones (PQ) were obtained using an X-ray diffractometer (SmartLab, Rigaku, Japan) based on $\text{Cu-K}\alpha$ ($\lambda = 0.15406$ nm) radiation. Thermogravimetric analysis (TGA, SDTA851, Mettler Toledo Instruments) was carried out from 25 to 800 °C at 10 °C min^{-1} , under nitrogen flow rate of 50 mL min^{-1} .

4.4.2 *ex-situ Characterization of PQ-A electrodes*

The Swagelok cells were disassembled in an argon-filled glovebox and the electrodes were washed with tetrahydrofuran. In order to remove PVDF binder and residual electrolyte, the electrode samples were sealed and sonicated in dimethoxyethane for 1 h, followed by drying under vacuum for 12 h. In order to avoid

exposure to oxygen and moisture, a home-made gas-tight XRD holder was employed during XRD analyses. Field-emission TEM (FE-TEM, Tecnai) was used to identify changes in the layered superstructures of the charged and discharged **PQ-Δ** electrodes.

4.4.3 Preparation of ALB electrodes and measurements

ALB electrodes were prepared according to the following procedures. PQ Derivatives, denka black, and polyvinylidene fluoride (PVDF, Arkema) binder were dispersed in *N*-methyl-2-pyrrolidone (NMP) in a weight ratio of 3: 5: 2, respectively. The resultant slurry was then cast onto a tantalum foil (99.95%, Thermo Fisher) or pyrolytic graphite foil (MTI) which serve as current collectors. These casted electrodes were dried at 70°C for 24 h under vacuum to remove residual NMP and the average electrode loading weight was found to be 0.5 mg cm⁻². **PQ-Δ-HY** was prepared by blending **PQ-Ref** or **PQ-Δ** with nano graphite flakes (N006, Digichem) according to the following procedure. Firstly, graphite (50 mg) was added to NMP (5 mL) and sonicated for 6 h, followed by addition of 50 mg of **PQ-Ref** or **PQ-Δ**: the mixture was dispersed for another 3 h. The solution was evaporated at 70°C for 72 h under vacuum, yielding **PQ-Δ-HY**. Electrodes incorporating **PQ-Δ-HY** were fabricated using a composite of **PQ-Δ-HY**: Denka black: PVDF = 8: 1: 1 = *w*: *w*: *w* in which **PQ-Δ** and graphite were mixed in equal amounts by weight. The loading of active materials on **PQ-Δ-HY** electrodes was either 2 or 9 mg cm⁻². The ALB electrolyte was prepared inside the glovebox. Aluminium trichloride (AlCl₃) was added slowly to ethyl-3-methylimidazolium tetrachloroaluminate (EMImAlCl₄) in a molar ratio of 1.0 to 1.5, and then the mixture was stirred for a further 6 h, after which the electrolyte exhibited a light-yellowish colour. The electrochemical measurements were conducted using a modified Swagelok-type cell, which was composed of the aluminium metal anode, a glass fiber membrane (GF/D, Whatman, USA), and the PQ derived cathode. The entire cell assembly process was carried out inside an argon-filled glovebox. All electrochemical measurements were performed using a battery cycler (MACCOR series 4000). CVs of PQ-based electrodes were performed at a rate of 5 mV s⁻¹ in the range of 0.8–1.75 V, while linear sweep voltammetry was performed from –0.7 to 3 V (vs Al/Al³⁺) at a current rate of 1 mV s⁻¹ to confirm the electrochemical stability of the

tantalum foil. Galvanostatic measurements were carried out after cycling 50 times by CV in order to activate PQ compounds except open-circuit (Supplementary Fig. 19 and 20) and Li-ion storage (Supplementary Fig. 21) measurements. The rate performance was evaluated, based on a current density of $1C = 100 \text{ mA g}^{-1}$. In the case of **PQ- Δ -HY**, the CV was measured at a scan rate of 5 mV s^{-1} in the range of 0.7–2.35 V. Furthermore, galvanostatic measurements were carried out at a current density of $1C = 100 \text{ mA g}^{-1}$ in the range of 0.7–2.35 V.

Chapter 5. Elucidating the Extraordinary Behavior of Phenanthrenequinone in Aluminum Batteries

5.1 Introduction

Even though lithium (Li)-ion batteries (LIBs) are the main power source of mobile electronic devices and green electric vehicles, the uneven global distribution and unpredictable cost of raw materials such as cobalt and Li precursors have promoted research on alternative battery chemistries involving multivalent carrier ions.^{4, 16, 107, 143} Another critical drawback of LIBs is the fact that they present a fire hazard and this has motivated the investigation of alternative safe systems.^{144, 145} In searching for the so-called “beyond-Li” systems, aluminum (Al) stands out as it is the third most abundant element in the Earth’s crust and has found use in a wide range of commodities. From the viewpoint of a battery electrode, metallic Al offers one of the highest theoretical capacities, 8,056 mAh cm⁻³, on account of its trivalency.^{10, 111, 146} In spite of these advantages, research on aluminum-ion batteries (AIBs) has not progressed much owing to the limited pool of materials suitable for use as the electrolyte and cathode. The main challenge associated with identifying electrolytes lies in the formation of a large band-gap passivation layer on the Al metal surface that prevents reversible Al plating and stripping. Finding materials for the cathode is not also trivial because the trivalency of the aluminum ion (Al³⁺) offers substantial resistance that hinders its diffusion into the framework of any material.^{147, 148}

One of the remarkable achievements in electrolyte research was the use of ionic liquids (ILs) containing aluminum trichloride (AlCl₃) with Lewis acidity. This family of electrolytes is known to remove the passivation layer of Al metal and facilitate the reversible reaction with Al metal by engaging the redox couple of AlCl₄⁻ and Al₂Cl₇⁻ ions. In particular, 1-ethyl-methylimidazolium chloride (EMImCl) with AlCl₃ was demonstrated to be adaptable with a variety of cathode materials, including graphite,^{131, 149-152} metal oxides,¹⁵³⁻¹⁵⁷ metal sulfides,¹⁵⁸⁻¹⁶² tellurium,⁸⁶ and sulfur.^{163, 164} Because the active ion species, Al₂Cl₇⁻, in these electrolytes can generate various types

of Al-containing ions, such as AlCl_4^- , AlCl_2^+ , or Al^{3+} , it is essential to understand how aluminum complex ions behave and are stored in electrode materials.¹⁶⁵ Surprisingly, even with the bulky cation of EMIm⁺, Lin *et al.* achieved extraordinarily high rate performance to a level at which AlCl_4^- ions can reversibly (de)intercalate into (from) the graphite even at a rate as high as 60 C.¹⁵²

We recently reported¹⁶⁶ a triangular macrocyclic compound as a cathode material for AIBs. This compound comprises three redox-active organic units of phenanthrenequinone (PQ) that are covalently linked in a triangular configuration. The PQ unit was found to coordinate with AlCl_2^+ complex ions for ion storage, unlike other typical cases in which ions were stored in the form of AlCl_4^- . The triangular structure also allows stacking to form a lamellar morphology to release the strain induced during the insertion and extraction of the complex ions, and also prevented unwanted dissolution into the electrolyte. Remarkably, from the viewpoint of kinetics, the reaction of AlCl_2^+ with PQ is quite fast such that 64% of the capacity is retained upon a 100-fold increase in the current density (i.e., 10 A g⁻¹). Nonetheless, details of the underlying mechanism have not yet been elucidated.

Herein, we report an in-depth study of the charge storage mechanism of PQ in coordination with aluminum chloride (AlCl_2^+). This investigation was motivated by the superior cycling and rate performance of PQ as a result of complexation with AlCl_2^+ compared to its Li⁺ ion counterparts, even in viscous ionic liquid electrolytes. A combination of density functional theory (DFT) calculations and experimental analyses revealed that this enhanced cycling and rate performance is related to the structure of the PQ- AlCl_2 complex with its lessened charge exposure such that reduced PQ is not easily dissolved in the electrolyte. Moreover, the formation of AlCl_2^+ without involving a separate step of solvent detachment for desolvation allows fast charge transfer, making its rate performance far superior to that of its Li-ion counterpart, the kinetics of which is usually more efficient based on its smaller ionic radius.

5.2 Result and discussion

As shown in Fig. 5-1a, 9,10-phenanthrenequinone (PQ) is an organic molecule with two adjacent carbonyl groups. When reduced, these carbonyl groups can coordinate with alkali ions such as Li^+ , Na^+ , and K^+ . The two benzene rings attached to the quinone unit in PQ readily stabilize the reduced state by forming a resonance structure with the obtained electrons. From the viewpoint of the crystal structure, the planar structure resulting from the presence of the two conjugated benzene rings promotes π - π interactions with adjacent molecules to form a stack in the direction perpendicular to the molecular plane. At the same time, the asymmetric molecular structure resulting from the carbonyl groups being located only on one side of the molecule leads to an in-plane molecular arrangement. This arrangement is such that the carbonyl groups of adjacent molecules do not face each other owing to the repulsive force between them. These molecular interactions are likely to be the origin of high crystallinity evidenced by sharp peaks on the X-ray diffraction (XRD) pattern (Fig. 5-2a). The high crystallinity together with the low binding force renders PQ less sustainable during repeated (de)insertion of ions to ultimately impose structural distortion, thereby causing severe dissolution (Fig. 5-2b and c).

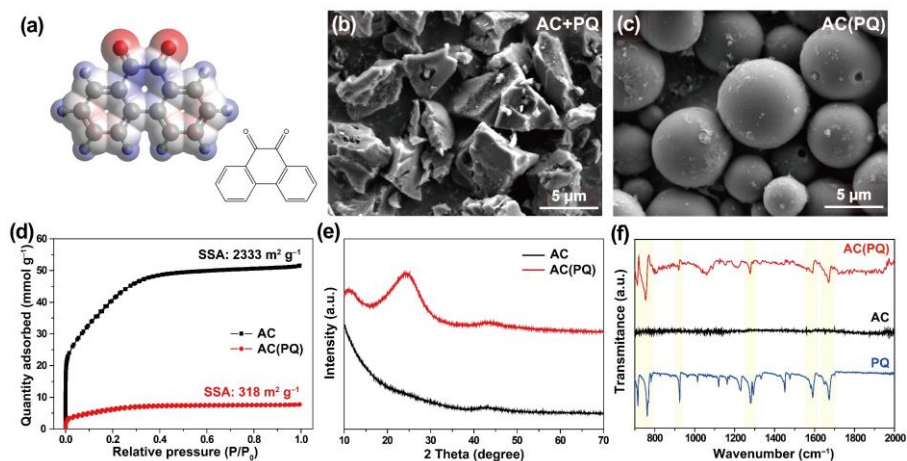


Fig. 5-1 (a) Molecular structure of PQ. SEM images of (b) physical mixture of AC and PQ and (c) AC with melt-infused PQ. (d) Adsorption-desorption isotherms of pristine AC and AC(PQ), and (e) their XRD patterns. (f) FT-IR spectra of PQ, AC, and AC(PQ).

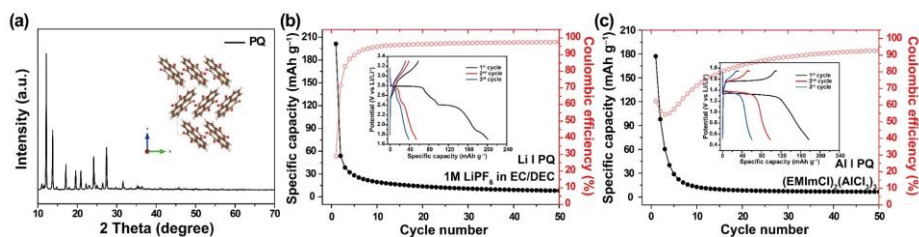


Fig. 5-2 (a) XRD patterns of PQ. Cycling performance of PQ with (b) 1M LiPF₆ in EC/DEC and (c) (EMImCl)₂(AlCl₃)₃ at a current density of 100 mA g⁻¹, together with their voltage profiles (insets).

In an effort to avoid the dissolution problem associated with the weak intermolecular binding force, we impregnated the pores of activated carbon (AC) with PQ molecules. The size of the AC particles used in this study (BEAPS-AC 0830, Asahi Chemicals) was in the range 5–10 μm and their pores were mainly nanopores with sizes below 3 nm. Fig. 5-1b shows the morphology of physically blended AC and PQ, and shows that the AC particles are wrapped by PQ. Considering the melting and boiling point of PQ of 210 and 360 °C, respectively, the sample was subjected to heat treatment at 250 °C for 3 hours to allow the PQ to infiltrate the AC. This sample was denoted as AC(PQ). The clean smooth surface of AC (Fig. 5-1c) was the first indication of the successful melt-infusion of PQ. The infiltration was further corroborated by adsorption-desorption isotherms using N₂ gas, which revealed that the specific surface area of AC(PQ) (318 m² g⁻¹) was significantly smaller than that of the pristine AC (2,333 m² g⁻¹) (Fig. 5-1d) as a result of the pores being filled with PQ. We examined the crystal structure of PQ after infiltration by conducting XRD analyses of both AC and AC(PQ) (Fig. 5-1e). The XRD profile of AC indicated its nearly amorphous nature, whereas that of AC(PQ) showed a single broad peak at 20–30°, implying that PQ lost its original crystallinity. The broad peak was similar to those of hard carbon materials,^{167, 168} suggesting that the confined PQ molecules mainly engaged in π-π interaction, either among themselves or with the interior surface of the pore, which consists of a conjugated carbon configuration. The pore distribution analysis showed that the overall pore distribution was maintained, but that the peak intensity was reduced, reconfirming that the PQ had infiltrated the pores. Infiltration can substantially lessen the problem of PQ dissolving in the electrolytes of lithium-ion batteries (LIBs) and aluminum-ion

batteries (AIBs) because the binding with the pore walls is stronger than the intermolecular interaction. In addition, the Fourier-transform infrared (FT-IR) spectroscopic results (Fig. 5-1f) confirmed that the confined PQ preserved its functional groups in the pristine state.

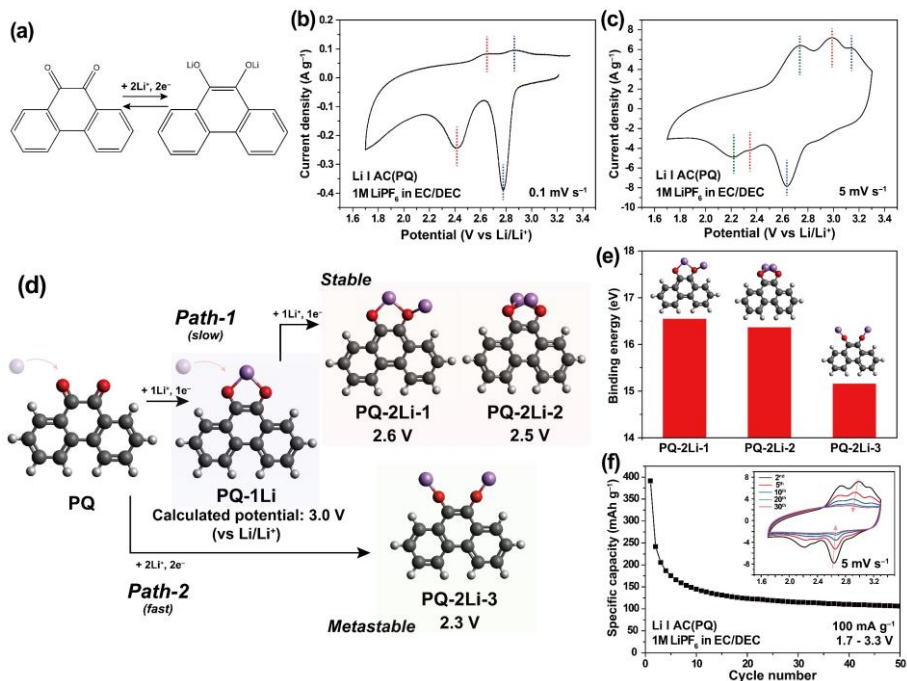


Fig. 5-3 (a) Redox reaction mechanism of PQ. CV profiles of AC(PQ) with 1M LiPF₆ in EC/DEC in the voltage range of 1.7–3.3 V at a scan rate of (b) 0.1 mV s⁻¹ and (c) 5 mV s⁻¹. (d) DFT calculations to present two reaction paths for binding with two Li⁺ ions. (e) Binding energies of the Li ion for the different coordination states. (f) Cycling performance of AC(PQ) at a current density of 100 mA g⁻¹ and (inset) CV profiles after a different number of cycles at a scan rate of 5 mV s⁻¹.

As indicated in Fig. 5-3a, PQ has two sites at which reduction can take place and accommodates up to two Li⁺ ions per molecular unit. It should be noted that the exact coordination structure of PQ-2Li has never been clarified because of the severe dissolution problem. We examined the electrochemical behavior of AC(PQ) by conducting cyclic voltammetry (CV) in 1M lithium hexafluorophosphate (LiPF₆) in ethylene carbonate and diethyl carbonate (EC/DEC=1/1=v/v) in the voltage range of

1.7–3.3 V at two different scan rates of 0.1 and 5 mV s⁻¹ (Fig. 5-3b and c). Two pairs of reversible reduction and oxidation peaks were observed at the scan rate of 0.1 mV s⁻¹, whereas three pairs of peaks were observed at the scan rate of 5 mV s⁻¹, implying kinetically different electrochemical behavior at different scan rates in relation to the coordination structures.

To elucidate the possible coordination structures and reaction paths, we carried out DFT calculations involving Li⁺ ions. Noteworthy is that all of the structures in Fig. 5-3d were structurally optimized and were thus thermodynamically stable states. The first reduction of PQ (PQ-1Li) involved the coordination of a single Li⁺ ion with the two carbonyl groups to form a chelated state. Coordination of an additional Li⁺ ion with the PQ-1Li yielded two stable states (PQ-2Li), which are feasible considering both the attractive force between the Li⁺ ion and carbonyl groups and the repulsive force between the two Li⁺ ions. PQ-2Li-1 was composed of the first Li⁺ ion chelated with both carbonyl groups and the other Li⁺ ion coordinated with one carbonyl group, whereas in PQ-2Li-2 both Li⁺ ions were coordinated with the two carbonyl groups (see Path-1 in Fig. 5-3d). On the other hand, if two Li⁺ ions were to rapidly approach pristine PQ, it could yield a metastable state (PQ-2Li-3) in which the Li⁺ ions coordinate with the carbonyl groups in the outward orientation (see Path-2 in Fig. 5-3d). As for the binding energy (Fig. 5-3e), that of the metastable state (PQ-2Li-3) was lower at 15.1 eV compared to those of the stable states of PQ-2Li-1 and PQ-2Li-2 (16.5 and 16.3 eV, respectively), implying that the additional metastable state could provide a facile path for the storage of two Li⁺ ions. This result of the calculation of the coordination structures is well associated with the electrochemical behavior. The calculated redox potentials (*vs.* Li/Li⁺) of PQ-1Li, stable PQ-2Li, and metastable PQ-2Li were 3.0, 2.6 (or 2.5 for the PQ-2Li-2 state), and 2.3 V, respectively, which were in good agreement with the three pairs of redox peaks in Fig. 5-3c. Thus, the reaction observed at a high scan rate can be understood in terms of two reaction paths, i.e., a slow reaction that takes place *via* PQ-2Li-1 (Path-1) and a fast reaction that proceeds directly to PQ-2Li-3 (Path-2). In the former case, PQ passes through the PQ-1Li intermediate state before reaching PQ-2Li-1 and PQ-2Li-2, whereas the latter case bypasses the PQ-1Li intermediate state, instead binding with two Li ions simultaneously to yield PQ-2Li-3.

Thus, at the lower scan rate of 0.1 mV s^{-1} , Path-1 was exclusively adopted, which correlates with the CV profiles in Fig. 5-3b and c. By contrast, at the higher scan rate of 5 mV s^{-1} , Path-1 and Path-2 were both adopted, resulting in three pairs of redox peaks being displayed. On cycling, the specific capacity decayed rapidly as observed in the galvanostatic and CV profiles in Fig. 5-3f. Based on the capacitive behavior of AC (Fig. 5-4) and the voltage profiles of AC(PQ), the observed capacity fading was attributed to the dissolution of the reduced PQ. For reference, charged organic compounds are known to be more vulnerable to dissolution¹⁶⁹⁻¹⁷² because solvation of the charged forms by electrolyte solvents is easier.

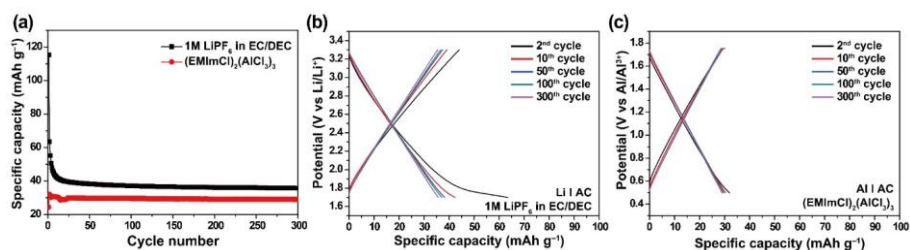


Fig. 5-4 (a) Cycling performance of bare AC with 1M LiPF₆ in EC/DEC and (EMImCl)₂(AlCl₃)₃. Their voltage profiles after a different number of cycles with (b) 1M LiPF₆ in EC/DEC and (c) (EMImCl)₂(AlCl₃)₃.

The coordination behavior of PQ with Li⁺ and AlCl₂⁺ ions was investigated by preparing Li and Al cells. For the Li cell, an AC(PQ) electrode was paired with a Li metal counter electrode with 1M LiPF₆ in EC/DEC or 1M lithium bis(trifluoromethylsulfonyl)imide (LiTFSI) in 1-butyl-1-methylpyrrolidinium bis(trifluoromethylsulfonyl)imide (Pyr14TFSI) as the electrolyte. For the Al cell, an AC(PQ) electrode was paired with an Al metal counter electrode with (EMImCl)₂(AlCl₃)₃ as the electrolyte (Fig. 5-5). Notably, 1M LiTFSI in Pyr14TFSI was included in the LIBs to ensure a more relevant comparison with the ionic liquid (IL) electrolyte for AIBs. PQ was characterized in the range of one-electron reduction by conducting CV tests at 5 mV s^{-1} in the voltage range of 2.5–3.3 V for LIBs and 0.5–1.7 V for AIBs. In the case of the LIB cell with 1M LiPF₆ in EC/DEC (Fig. 5-5a), the intensities of the redox peaks were retained to a much greater extent compared to those of the two-electron reduction in Fig. 5-3f, implying that the dissolution of PQ upon binding a single Li⁺ ion was lessened much more. In the case of the LIB cell with 1M

LiTFSI in Pyr14TFSI (Fig. 5-5b), the intensities of the redox peaks were more effectively maintained over cycling with higher overpotentials compared to those of the EC/DEC-based counterpart. The improved cyclability and higher overpotentials were presumably attributed to the low solubility of PQ-1Li and the lower Li ionic conductivity in the IL, respectively. By stark contrast, the intensity of the redox peaks in the cell with (EMImCl)₂(AlCl₃)₃ gradually increased up to the 50th cycle, after which the redox behavior stabilized (Fig. 5-5c), suggesting that the PQ-AlCl₂ complex is highly stable. The larger redox overpotentials in the initial discharge and the gradual capacity increase during the activation period are likely attributed to electrode wetting with the electrolyte and electrolyte infiltration into the pores of AC.

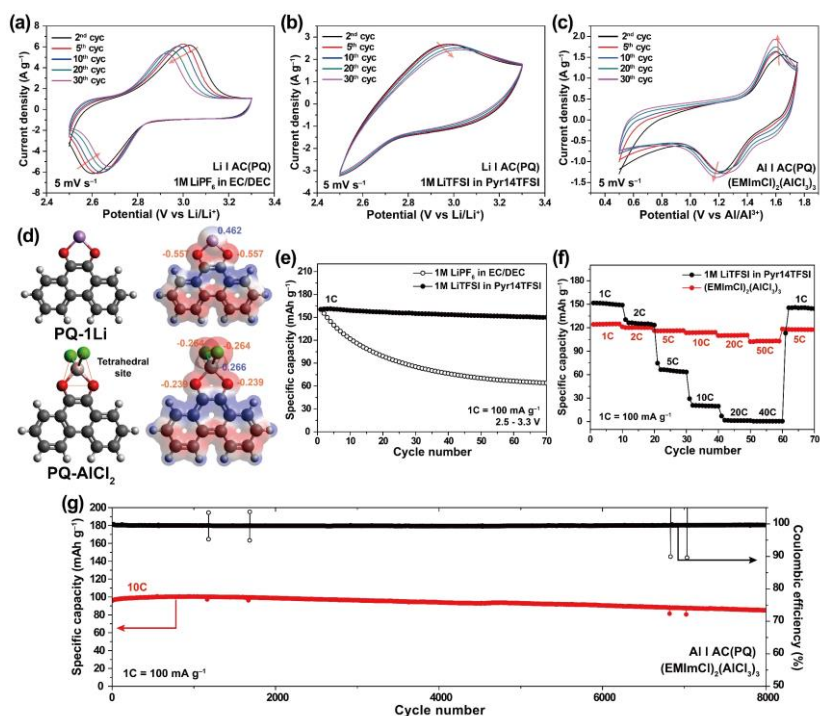


Fig. 5-5 CV profiles after a different number of cycles at a scan rate of 5 mV s⁻¹ with (a) 1M LiPF₆ in EC/DEC, (b) 1M LiTFSI in Pyr14TFSI, and (c) (EMImCl)₂(AlCl₃)₃. (d) Optimized structures and atomic charges of PQ-1Li and PQ-AlCl₂. (e) Cycling performance of AC(PQ) with 1M LiPF₆ in EC/DEC and 1M LiTFSI in Pyr14TFSI. (f) Rate capabilities of AC(PQ) with 1M LiTFSI in Pyr14TFSI and (EMImCl)₂(AlCl₃)₃. (g) Extended cycling test of AC(PQ) with (EMImCl)₂(AlCl₃)₃. The measurements of cells containing Li and Al electrolytes were performed in the voltage ranges of 2.5–3.3 V vs. Li/Li⁺ and 0.5–1.7 V vs. Al/Al³⁺, respectively.

In an attempt to understand the observed difference, the optimized structures and charge distributions of PQ-1Li and PQ-AlCl₂ were investigated by conducting DFT calculations (Fig. 5-5d). Prior to the calculations, we first elucidated the discharged molecular structure by energy-dispersive X-ray spectroscopy (EDS) mapping. Upon the reduction of PQ in AC(PQ) to PQ-AlCl₂ during discharging in (EMImCl)₂(AlCl₃)₃, the EDS mapping indicated that the Al-to-Cl atomic ratio was 1.8. By contrast, the charged electrode that underwent thorough washing showed negligible peaks of Al and Cl, confirming that the observed Al and Cl peaks at the charged state did not originate from residual electrolyte. In addition, electron spin resonance (ESR) analysis indicates the presence of radical in the discharged state, implying that the main complexation process involves one electron per each molecular unit of PQ (Fig. 5-6).

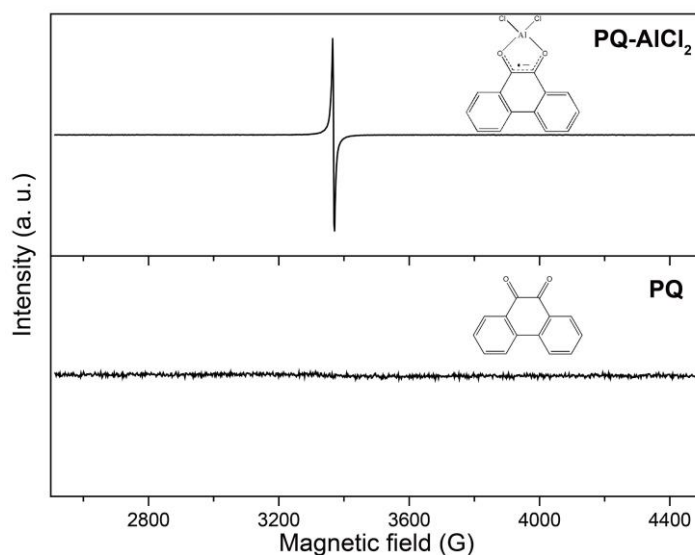


Fig. 5-6 ESR spectra of the pristine and discharged AC(PQ) with (EMImCl)₂(AlCl₃)₃.

As in the case of the Li⁺ ion in PQ-1Li, the AlCl₂⁺ complex ion was chelated to the two carbonyl groups, with the Al ion positioned at the center of a tetrahedral structure of which the corners were occupied by the two carbonyl groups and two chlorine ligands. Considering the atomic charge, that of the Li⁺ ion in PQ-1Li was +0.462, whereas that of the Al³⁺ ion in PQ-AlCl₂ was lower at +0.266. The lower atomic charge of Al³⁺ based on shielding by the neighboring chlorine ions in its chelated form

would be beneficial for sustainable cycling because a higher charge state of an organic active material would be more vulnerable to solvation by electrolyte solvents. The stability of PQ-AlCl₂ was further investigated by measuring capacity retention after 6 hrs of rest at the discharged state (Fig. 5-7). While AC(PQ) with 1M LiPF₆ in EC/DEC and 1M LiTFSI in Pyr14TFSI maintained 71.7% and 78.1% of their original capacities, respectively, AC(PQ) with (EMImCl)₂(AlCl₃)₃ preserved 87.2%, reconfirming the higher stability of PQ-AlCl₂ against dissolution to the electrolyte.

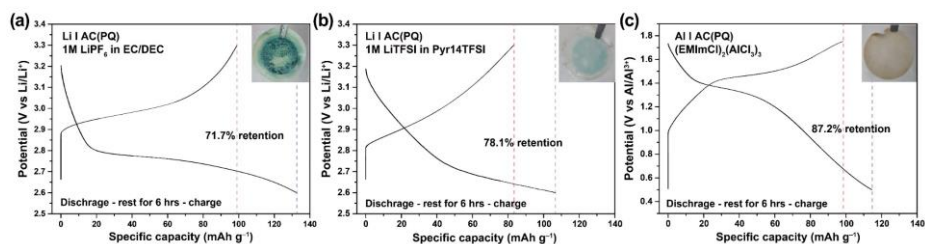


Fig. 5-7 Voltage profiles of discharge and charge after 6 hrs of rest at the discharged state: (a) 1M LiPF₆ in EC/DEC, (b) 1M LiTFSI in Pyr14TFSI, and (c) (EMImCl)₂(AlCl₃)₃. (Insets) Photographs of the separators after the dissolution test.

We further conducted cycling and rate capability tests for both types of cells. Galvanostatic tests (Fig. 5-5e) indicated that, whereas AC(PQ) in 1M LiPF₆ in EC/DEC retained only 40% of the initial capacity of 160 mAh g⁻¹ after 70 cycles, AC(PQ) in 1M LiTFSI in Pyr14TFSI preserved a higher capacity corresponding to 93.7% after the same number of cycles, once again due to the lower solubility of PQ-1Li in the IL. The rate capability tests (Fig. 5-5f) revealed that AC(PQ) in 1M LiTFSI in Pyr14TFSI exhibited capacity retention of 83.4, 43.7, 13.2, 0.1, and 0% with respect to its initial capacity of 151 mAh g⁻¹ when the current density was increased by 2, 5, 10, 20, and 40 times from 100 mA g⁻¹. In contrast, AC(PQ) in (EMImCl)₂(AlCl₃)₃ showed far superior rate capability such that it retained 96.7, 93.5, 91.1, 88.7, and 82.2% with respect to its initial capacity of 124 mA g⁻¹ when the current density was increased by 2, 5, 10, 20, and 50 times from 100 mA g⁻¹. At a current density of 10C (= 1 A g⁻¹), remarkably, 88.8% of the initial capacity was retained even after 8,000 cycles (Fig. 5-5g), verifying the structural and interfacial stability of PQ in repeated (de)complexation with the AlCl₂⁺ ion.

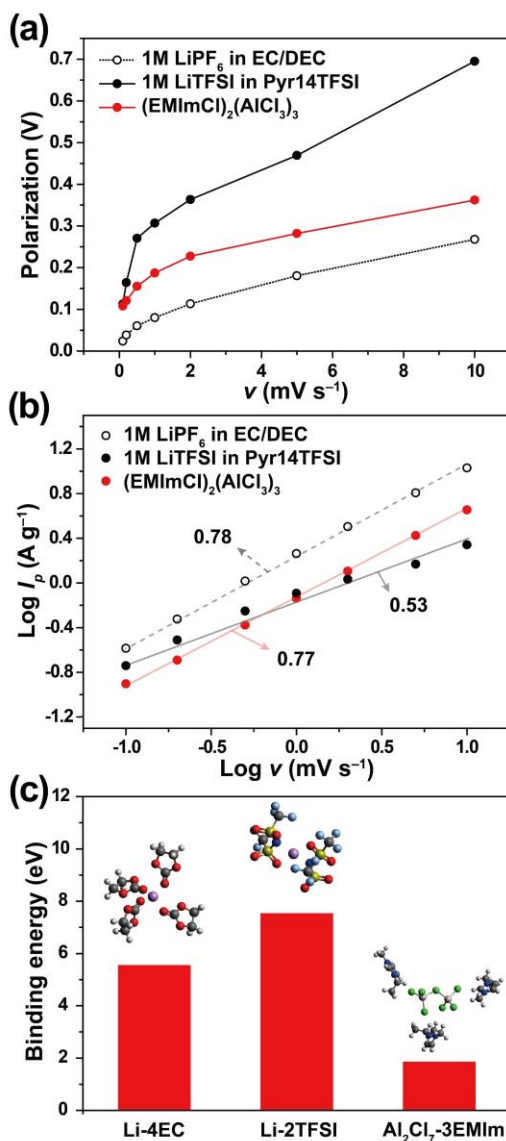


Fig. 5-8 Dependence of the CV on the scan rate with different electrolytes. (a) Potential polarization between the cathodic and anodic peaks in the CV curves. (b) $\log v$ - $\log I$ plots to extract b -values based on the relation $I_p = av^b$. (c) Binding energies for desolvation in different electrolytes.

In order to elaborate the mechanism of fast kinetics of AC(PQ) in $(EMImCl)_2(AlCl_3)_3$, we conducted scan rate-dependent CV measurements in the voltage range of 2.6–3.3 V for LIBs and in the voltage range of 0.5–1.7 V for AIBs (Fig. 5-8a). All CV profiles exhibited one pair of cathodic and anodic peaks and the potential polarizations were examined by obtaining the difference between those peaks. In the case of LIBs, the cell with 1M LiPF₆ in EC/DEC had a much lower polarization than those with 1M LiTFSI in Pyr14TFSI, which was mainly ascribed to the lower ionic conductivity of Pyr14TFSI.¹⁷³ In the case of $(EMImCl)_2(AlCl_3)_3$, upon increasing the scan rate, the polarization increase exhibited by the cell was similar to that of 1M LiPF₆ in EC/DEC, although the polarization was about 0.1 V higher than that of 1M LiPF₆ in EC/DEC at each of the scan rates. This is because the polarization generated at the side of the anode is associated with Al plating and stripping. The higher polarization at the anode side of the Al cell was confirmed in symmetric cell tests performed at various current densities (Fig. 5-9). When galvanostatically scanned, the polarization of the cell with 1M LiTFSI in Pyr14TFSI was high at approximately 200 mV at a current density of 0.1 mA cm⁻² and failed to run once the current density was raised to 0.2 mA cm⁻². In the case of $(EMImCl)_2(AlCl_3)_3$, the cell polarization approximated 60 mV at 0.1 mA cm⁻², which is comparable to that of 1M LiPF₆ in EC/DEC (~40 mV), and the polarization trends among the three cells were maintained over the entire range of scan rates (Fig. 5-8a). The consistent polarization offsets between 1M LiTFSI in Pyr14TFSI and $(EMImCl)_2(AlCl_3)_3$ over the scan rates verifies that the higher polarization originated at the side of the anode.

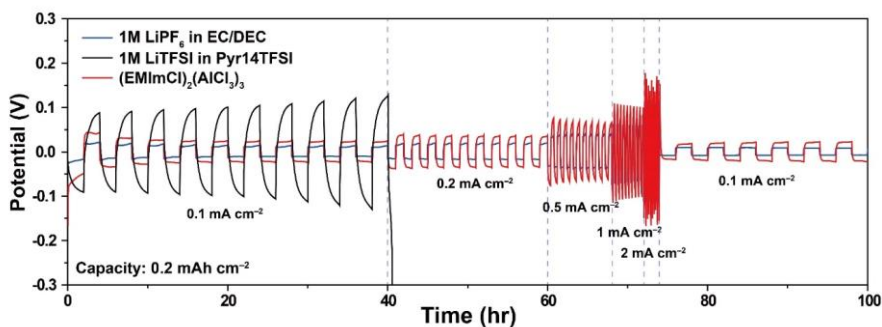


Fig. 5-9 Voltage profiles of symmetric cells with different electrolytes at various current densities.

The charge storage in the CV scan can be understood on the basis of three different processes: a faradaic process based on carrier ion insertion, a pseudo-capacitive process involving charge transfer, and non-faradaic charge storage in the electric double layer.^{174, 175} The contributions of individual processes can be identified by analyzing the CV profiles at various scan rates according to the following relation between the current (I) and the scan rate (ν):

$$I = a\nu^b$$

, in which the b -value can be determined by the slope in the $(\log \nu)$ - $(\log I)$ plot. Particularly, it is known that $b = 0.5$ corresponds to the diffusion-controlled process, whereas $b = 1$ corresponds to the exclusive capacitive-limiting process with negligible charge transfer. The $(\log \nu)$ - $(\log I_p)$ plots and b -values are shown in Fig. 5-8b, with the b -values being between 0.5 and 1, indicating the combined diffusion-based and capacitive storage events. In the case of the LIBs, the cell with 1M LiTFSI in Pyr14TFSI exhibited a particularly low b -value of 0.53, revealing its dominant diffusion-controlled charge storage. The cell with 1M LiPF₆ in EC/DEC showed a higher b -value of 0.78, indicating higher capacitive contribution and faster diffusion kinetics. In the case of the AIBs, the cell with (EMImCl)₂(AlCl₃)₃ exhibited a similar b -value of 0.77, even though a viscous IL was used as the electrolyte. The capacitive contributions at specific voltages were further extracted from the measured CV profiles, and showed a similar trend among the cells with that obtained from their b -values. The substantial contribution from the capacitive process reflected facile ion diffusion and charge-transfer at the electrode-electrolyte interface.

In an effort to deepen our understanding of the behavior of ions at the interface, we evaluated the desolvation energies for different electrolytes (Fig. 5-8c). It should be noted, the Li⁺ ions in EC/DEC were assumed to mainly be solvated by 4 EC molecules because of their high dielectric constant,¹⁷⁶ and the Li⁺ ions in Pyr14TFSI are solvated by two TFSI⁻ anions.¹⁷⁷ The AlCl₂⁺ ion is extracted by the following dissociation:¹⁷⁸



The desolvation energy was retrieved by determining the energy difference between the sum of the energies of the individual salts and solvent molecules and the same sum but with solvation shells, and all the energies were based on the optimized structures.

Here, desolvation energy refers to the energy required for generating carrier ions at the electrode-electrolyte interface. The DFT calculations revealed that Li-2TFSI and Li-4EC required a desolvation energy of 7.51 eV and 5.53 eV, respectively, but that $\text{Al}_2\text{Cl}_7\text{-3EMIm}$ required much lower energy of 1.83 eV. This difference can be explained by the different desolvation processes: in the case of the Li^+ ion, the desolvation of Li-2TFSI and Li-4EC is related to the dissociation from the anion and detachment of the solvent molecules, respectively, whereas in the case of AlCl_2^+ , desolvation is composed of the dissociation of Al_2Cl_7^- to AlCl_2^+ and AlCl_4^- , after which AlCl_4^- is re-coordinated to EMIm^+ . On the whole, the formation of AlCl_2^+ can be realized *via* a simple dissociation-re-coordination process, saving the energy that would have been required for desolvation.

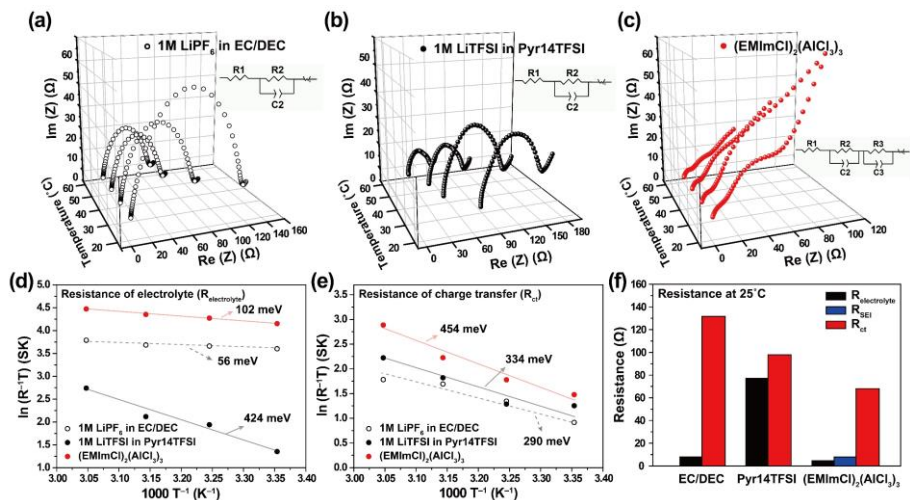


Fig. 5-10 Temperature-dependent Nyquist plots of AC(PQ) with (a) 1M LiPF_6 in EC/DEC, (b) 1M LiTFSI in Pyr14TFSI, and (c) $(\text{EMImCl})_2(\text{AlCl}_3)_3$. Arrhenius plots of the resistance of (d) the electrolyte ($R_{\text{electrolyte}}$) and (e) charge transfer (R_{ct}). (f) Comparison of the resistance contributions at 25 °C.

The fast kinetics with $(\text{EMImCl})_2(\text{AlCl}_3)_3$ was investigated in greater depth by using temperature-dependent electrochemical impedance spectroscopy (EIS) to extract the individual resistance components and activation energies (E_a) (Fig. 5-10). The Nyquist plots of AC(PQ) with various electrolytes at 25–55 °C are displayed in Fig. 5-10a–c. As expected, the total resistance of all the cases decreased as the temperature

increased. The resistance can be categorized into the ion conduction resistance in the electrolyte ($R_{\text{electrolyte}}$) and the charge transfer resistance (R_{ct}) at the interface, and these two types of resistance were retrieved by fitting the EIS spectra to an equivalent circuit. R_{ct} can be further split into desolvation resistance and genuine charge transfer resistance by imposing relaxation time. Here it is necessary to note that, in the case of the AIBs, the resistance of the SEI layer (R_{SEI}) on the anode side was additionally taken into consideration. The activation energy of the individual types of resistance can be assessed by the following Arrhenius equation:¹⁷⁹

$$\sigma T = A \exp(-E_a/k_B T)$$

, where A is the pre-exponential constant, E_a is the activation energy for ion transport, k_B is Boltzmann's constant, T is the absolute temperature, and σ is the ionic conductivity.

Arrhenius plots of the resistance of the electrolyte and that of the charge transfer process with various electrolytes are presented in Fig. 5-10d–e. The plot of $R_{\text{electrolyte}}$ shows that the cell with 1M LiTFSI in Pyr14TFSI had the highest activation energy of 424 meV, whereas the cell with 1M LiPF₆ in EC/DEC showed the lowest activation energy of 56 meV, and the cell with (EMImCl)₂(AlCl₃)₃ exhibited a relatively low activation energy of 102 meV. Although ionic liquids are known to have low ionic conductivity because of their high viscosity, (EMImCl)₂(AlCl₃)₃ exhibited low electrolyte resistance owing to the low cation-anion dissociation energy from delocalized organic cations (EMIm⁺) and bulky anions (AlCl₄⁻, and Al₂Cl₇⁻).¹⁷⁷ In comparison, the R_{ct} plots (Fig. 5-10e) show that the cell with (EMImCl)₂(AlCl₃)₃ had the highest activation energy of 454 meV compared to 334 and 290 meV with 1M LiTFSI in Pyr14TFSI and 1M LiPF₆ in EC/DEC, respectively. The higher activation energy of (EMImCl)₂(AlCl₃)₃ implies greater sensitivity to temperature change. Based on the highest activation energy and the lowest resistance at room temperature (Fig. 5-10f), the rate performance of (EMImCl)₂(AlCl₃)₃ is anticipated to improve even further at temperatures above 25 °C.

5.3 Conclusion

In conclusion, PQ melt-infused activated carbon (AC(PQ)) exhibited outstanding rate and cycling performance as an active material for AIBs even when viscous IL electrolytes with bulky aluminum-chloride complex ions were used. The long-term structural and electrochemical stability of PQ in AIBs originated from its reduced effective charge upon coordination with AlCl_2^+ , which suppresses its dissolution into the electrolyte. On the other hand, the fast storage kinetics resulted from fast charge transfer enabled by the facile transitions of aluminum-chloride complex ions at the interface without separate desolvation being necessary. In contrast, the performance of PQ in the LIB electrolytes including a liquid-based electrolyte was far inferior as a result of unstable Li-PQ coordination in both reduced states (the coordination of both one and two Li^+ ions). Our investigation provides useful information in that Al-coordinated structures and the behavior of Al complex ions at the interface play a critical role in the overall performance of AIBs.

5.4 Experimental

5.4.1 *Synthesis of materials*

9,10-phenanthrenequinone (PQ, >99%), 1-butyl-1-methylpyrrolidinium bis(trifluoromethylsulfonyl)imide (Pyr14TFSI, >99%, <500 ppm H₂O), LiTFSI (99.5%), 1-ethyl-3-methylimidazolium chloride-aluminum chloride ((EMImCl)₂(AlCl₃)₃) were purchased from Sigma-Aldrich. Activated carbon (AC0830) was purchased from Asahi Organic Chemicals. 1M LiPF₆ in EC/DEC was purchased from PANAX ETEC. All the materials were used without further purification. AC(PQ) was prepared based on the following procedure: 1 g of AC and 3 g of PQ were ground together in a mortar. The well-mixed composite was pelletized and heated at 250 °C for 3 hours in Ar atmosphere.

5.4.2 *Electrochemical measurements*

The electrodes were prepared according to the following procedures. PQ or AC(PQ), super-P, and poly(vinylidene difluoride) (PVDF, Arkema) binder were uniformly dispersed in *N*-methyl 2-pyrrolidone in a weight ratio of 90:5:5. The well-mixed slurry was cast onto tantalum foil (99.95%, Thermo Fisher) and spread by using the doctor blade technique. The cast electrodes were dried under vacuum at 80 °C for 24 hours, and the average loading of PQ alone was 1 mg cm⁻². The mass content of PQ in AC(PQ) was evaluated using TGA, and the value was 48 wt%. The electrochemical performance was characterized by preparing 2032 coin-type cells for LIBs or modified Swagelok-type cells for AIBs. The entire cell assembly process was carried out inside an argon-filled glove box. Cyclic voltammetry and galvanostatic measurements were performed using a battery cycler (WBCS3000L, Wonatech) at 25 °C. In the case of the AIB cells, galvanostatic measurements were carried out after 50 CV cycles to activate the AC(PQ). The respective resistance values of the individual electrochemical processes were determined by using electrochemical impedance spectroscopy (VSP, Bio-Logic) in the frequency range of 0.01 to 10⁶ Hz in the temperature range 25–55 °C.

5.4.3 Characterization

The morphologies of the AC, PQ, and AC(PQ) were characterized by using the field-emission scanning electron microscopy (SEM, JSM-7800F Prime, JEOL, Japan) and high-resolution transmission electron microscopy (TEM, JEM-3010, JEOL, Japan) instruments at the National Center for Inter-University Research Facilities (NCIRF) at Seoul National University. All the electrode samples subject to *ex-situ* characterizations were washed with 1,2-dimethoxyethane, followed by drying under vacuum for 3 hrs. The functional groups of AC, PQ, and AC(PQ) were analyzed by Fourier-transform infrared spectroscopy (FTIR, JASCO FT/IR-6700). The X-ray diffraction profiles were obtained using an X-ray diffractometer (SmartLab, Rigaku) based on Cu-K α ($\lambda=0.15406$ nm) radiation. The specific surface areas (SSAs) and pore size distributions were obtained from N₂ adsorption-desorption measurements by using a porosity analyzer (Micromeritics, 3FLEX) operating at 87 K. The chemical compositions were analyzed by XPS (Sigma Probe, thermo VG Scientific, England) with an Mg K α line as an X-ray source. ESR (EMXmicro, Bruker) analysis was performed at room temperature to detect the radical anion for the discharged AC(PQ).

5.4.4 DFT calculation

Geometrical optimizations and energy calculations were performed without symmetry restriction using the B3LYP hybrid density functional implemented in the GAUSSIAN 09 software package. The 6-31+G(d, p) basis sets were adopted for all the atoms. Frequency calculations at the same basis sets were performed to determine the nature of a stationary point as a true local minimum. For the potential calculations of PQ-1Li, PQ-2Li-1, PQ-2Li-2, and PQ-2Li-3, the polarization continuum model (PCM) with the ethanol parameter and dielectric constant ($\epsilon=24.6$) was used to implicitly take included solvent molecules into consideration. We calculated the potentials based on the following equation:

$$E \text{ (vs. Li/Li}^+\text{)} = \frac{\Delta G}{-nF} - 1.4$$

, where E is the formal potential, ΔG is the free energy of reaction, n is the number of electrons transferred in the reaction, and F is Faraday's constant. The reference

potential of Li/Li^+ was determined by subtracting 1.4 V from the formal potential, because the SHE is -4.4 V vs. vacuum and the potential of Li/Li^+ is -3.0 V vs. SHE. The desolvation energies were obtained by using the explicit solvation model in the gas phase to compare the trends between electrolytes.

Chapter 6. Summary and Conclusions

In *Chapter 2*, it was demonstrated that toluene can be a useful co-solvent for carbonate-based electrolyte solutions for Li metal batteries. The preceded reductive decomposition of toluene prior to that of carbonate solvents commonly used in LIB electrolytes results in a more uniform and rigid SEI layer. The electron donating nature of the methyl group in toluene allows the preceded decomposition and resulting facile radical polymerization with uniform surface passivation. Furthermore, the polymerization process of toluene induces the uniform distribution of LiF and thus enables the ‘high concentration’ effect even with 3 M of LiFSI, leading to relatively decent average Coulombic efficiency of 97.2% over 350 cycles for carbonate electrolytes. The addition of toluene also considerably improves the cycling performance of a full-cell in pairing with $\text{LiNi}_{0.5}\text{Co}_{0.2}\text{Mn}_{0.3}\text{O}_2$ cathode. The present investigation provides a useful guideline in designing carbonate-based electrolytes for Li metal anodes, that is, the addition of aromatic compounds that induces a more stable and rigid SEI layer based on the tuning of the electron density in the benzene ring.

In *Chapter 3*, a localized high concentration electrolyte (LHCE) and LiF-rich SEI composition for Li metal anodes was realized by utilizing fluorinated aromatic solvents. Among them 1,2-dfBen is remarkable as it realizes both the high-concentration effect and a LiF-rich SEI layer simultaneously. In fact, 1,2-dfBen is the first non-HFE diluent solvent for LHCEs and thus unfolds the promise of fluorinated aromatic compounds in relation to their LUMO energy levels, binding affinity with the Li ion, and fluorine-donating power. It was also identified that an optimal triple salt composition that assists with the formation of a LiF-rich SEI layer and prevents the corrosion of the aluminum current collector while maintaining the high-concentration effect even at a relatively low salt concentration of 2.02 M. The present investigation heightens the possibility of achieving the highly beneficial yet economically feasible high-concentration effect for emerging LMBs.

In *Chapter 4*, three phenanthrenequinone derivatives—a monomer, a linear trimer, and a molecular triangle—were prepared as active materials for emerging ALBs

and explored to identify their structure-performance relationships. Although all three compounds based on quinone functional groups exhibit similar redox potentials, the triangular disposition of the redox-active units influences very strongly the accessibility of chloroaluminate ions, as well as the solubility of the triangular molecules. Most remarkably, the rigid triangular macrocycle improves the specific capacity and the cyclability dramatically. In addition, fabricating the hybrid electrode with graphite flakes overcomes the inherently low electronic conductivity and limited areal loading of conventional organic electrodes, enabling the bipolar storage of anions and cations to increase the specific capacity. In the future development of affordable large-scale energy storage systems, other redox-active organic molecules with well-defined geometries will find use as active materials in ALBs.

In *Chapter 5*, phenanthrenequinone (PQ) melt-infused activated carbon (AC(PQ)) exhibited outstanding rate and cycling performance as an active material for AIBs even when viscous IL electrolytes with bulky aluminum-chloride complex ions were used. The long-term structural and electrochemical stability of PQ in AIBs originated from its reduced effective charge upon coordination with AlCl_2^+ , which suppresses its dissolution into the electrolyte. On the other hand, the fast storage kinetics resulted from fast charge transfer enabled by the facile transitions of aluminum-chloride complex ions at the interface without separate desolvation being necessary. In contrast, the performance of PQ in the LIB electrolytes including a liquid-based electrolyte was far inferior as a result of unstable Li-PQ coordination in both reduced states (the coordination of both one and two Li^+ ions). This investigation provides useful information in that Al-coordinated structures and the behavior of Al complex ions at the interface play a critical role in the overall performance of AIBs.

Bibliography

1. V. Etacheri, R. Marom, R. Elazari, G. Salitra and D. Aurbach, *Energy Environ. Sci.*, **2011**, *4*, 3243-3262.
2. N. Nitta, F. Wu, J. T. Lee and G. Yushin, *Mater. Today*, **2015**, *18*, 252-264.
3. R. Marom, S. F. Amalraj, N. Leifer, D. Jacob and D. Aurbach, *J. Mater. Chem.*, **2011**, *21*, 9938-9954.
4. J. W. Choi and D. Aurbach, *Nat. Rev. Mater.*, **2016**, *1*, 16013.
5. P. Albertus, S. Babinec, S. Litzelman and A. Newman, *Nat. Energy*, **2018**, *3*, 16-21.
6. P. Bai, J. Li, F. R. Brushett and M. Z. Bazant, *Energy Environ. Sci.*, **2016**, *9*, 3221-3229.
7. W. Guo, S. Liu, X. Guan, X. Zhang, X. Liu and J. Luo, *Adv. Energy Mater.*, **2019**, *9*, 1900193.
8. S. Liu, X. Ji, J. Yue, S. Hou, P. Wang, C. Cui, J. Chen, B. Shao, J. Li, F. Han, J. Tu and C. Wang, *J. Am. Chem. Soc.*, **2020**, *142*, 2438-2447.
9. M.-C. Lin, M. Gong, B. Lu, Y. Wu, D.-Y. Wang, M. Guan, M. Angell, C. Chen, J. Yang, B.-J. Hwang and H. Dai, *Nature*, **2015**, *520*, 324-328.
10. J. Muldoon, C. B. Bucur and T. Gregory, *Chem. Rev.*, **2014**, *114*, 11683-11720.
11. G. A. Elia, K. Marquardt, K. Hoepfner, S. Fantini, R. Lin, E. Knipping, W. Peters, J.-F. Drillet, S. Passerini and R. Hahn, *Adv. Mater.*, **2016**, *28*, 7564-7579.
12. D.-J. Yoo, S. Yang, Y. S. Yun, J. H. Choi, D. Yoo, K. J. Kim and J. W. Choi, *Adv. Energy Mater.*, **2018**, *8*, 1802365.
13. D.-J. Yoo, S. Yang, K. J. Kim and J. W. Choi, *Angew. Chem. Int. Ed.*, **2020**, Accepted Author Manuscript. doi:10.1002/anie.202003663.
14. D. J. Kim, D.-J. Yoo, M. T. Otle, A. Prokofjevs, C. Pezzato, M. Owczarek, S. J. Lee, J. W. Choi and J. F. Stoddart, *Nat. Energy*, **2019**, *4*, 51-59.
15. D.-J. Yoo and J. W. Choi, *J. Phys. Chem. Lett.*, **2020**, *11*, 2384-2392.
16. B. Dunn, H. Kamath and J.-M. Tarascon, *Science*, **2011**, *334*, 928-935.
17. S. Li, M. Jiang, Y. Xie, H. Xu, J. Jia and J. Li, *Adv. Mater.*, **2018**, *30*, 1706375.
18. D. Lin, Y. Liu and Y. Cui, *Nat. Nanotechnol.*, **2017**, *12*, 194.
19. C. Brissot, M. Rosso, J.-N. Chazalviel and S. Lascaud, *J. Power Sources*, **1999**, *81*, 925-929.
20. K.-H. Chen, K. N. Wood, E. Kazyak, W. S. LePage, A. L. Davis, A. J. Sanchez and N. P. Dasgupta, *J. Mater. Chem. A*, **2017**, *5*, 11671-11681.
21. Y. Gu, W.-W. Wang, Y.-J. Li, Q.-H. Wu, S. Tang, J.-W. Yan, M.-S. Zheng, D.-Y. Wu, C.-H. Fan and W.-Q. Hu, *Nat. Commun.*, **2018**, *9*, 1339.
22. Q. Pang, X. Liang, A. Shyamsunder and L. F. Nazar, *Joule*, **2017**, *1*, 871-886.
23. J.-S. Kim, D. W. Kim, H. T. Jung and J. W. Choi, *Chem. Mater.*, **2015**, *27*, 2780-2787.

24. X. Liang, Q. Pang, I. R. Kochetkov, M. S. Sempere, H. Huang, X. Sun and L. F. Nazar, *Nat. Energy*, **2017**, *2*, 17119.
25. Z. Tu, S. Choudhury, M. J. Zachman, S. Wei, K. Zhang, L. F. Kourkoutis and L. A. Archer, *Nat. Energy*, **2018**, *3*, 310.
26. L. Wang, L. Zhang, Q. Wang, W. Li, B. Wu, W. Jia, Y. Wang, J. Li and H. Li, *Energy Storage Mater.*, **2018**, *10*, 16-23.
27. C. Yan, X. B. Cheng, Y. Tian, X. Chen, X. Q. Zhang, W. J. Li, J. Q. Huang and Q. Zhang, *Adv. Mater.*, **2018**, 1707629.
28. J. S. Kim, T. H. Hwang, B. G. Kim, J. Min and J. W. Choi, *Adv. Funct. Mater.*, **2014**, *24*, 5359-5367.
29. J. S. Kim, D. J. Yoo, J. Min, R. A. Shakoor, R. Kahraman and J. W. Choi, *ChemNanoMat*, **2015**, *1*, 240-245.
30. X. Q. Zhang, X. Chen, X. B. Cheng, B. Q. Li, X. Shen, C. Yan, J. Q. Huang and Q. Zhang, *Angew. Chem. Int. Ed.*, **2018**, *57*, 5301-5305.
31. D. Aurbach, K. Gamolsky, B. Markovsky, Y. Gofer, M. Schmidt and U. Heider, *Electrochim. Acta*, **2002**, *47*, 1423-1439.
32. J. Burns, R. Petibon, K. Nelson, N. Sinha, A. Kassam, B. Way and J. Dahn, *J. Electrochem. Soc.*, **2013**, *160*, A1668-A1674.
33. Z. Hu, S. Zhang, S. Dong, Q. Li, G. Cui and L. Chen, *Chem. Mater.*, **2018**, *30*, 4039-4047.
34. L. El Ouatani, R. Dedryvère, C. Siret, P. Biensan, S. Reynaud, P. Iratçabal and D. Gonbeau, *J. Electrochem. Soc.*, **2009**, *156*, A103-A113.
35. W. Yao, Z. Zhang, J. Gao, J. Li, J. Xu, Z. Wang and Y. Yang, *Energy Environ. Sci.*, **2009**, *2*, 1102-1108.
36. E. Markevich, G. Salitra, F. Chesneau, M. Schmidt and D. Aurbach, *ACS Energy Lett.*, **2017**, *2*, 1321-1326.
37. X. Ren, Y. Zhang, M. H. Engelhard, Q. Li, J.-G. Zhang and W. Xu, *ACS Energy Lett.*, **2017**, *3*, 14-19.
38. X. Q. Zhang, X. B. Cheng, X. Chen, C. Yan and Q. Zhang, *Adv. Funct. Mater.*, **2017**, *27*, 1605989.
39. S. Choudhury, D. Vu, A. Warren, M. D. Tikekar, Z. Tu and L. A. Archer, *Proc. Natl. Acad. Sci. USA*, **2018**, 201803385.
40. S. Stalin, S. Choudhury, K. Zhang and L. A. Archer, *Chem. Mater.*, **2018**, *30*, 2058-2066.
41. Z. Tu, S. Choudhury, M. J. Zachman, S. Wei, K. Zhang, L. F. Kourkoutis and L. A. Archer, *Joule*, **2017**, *1*, 394-406.
42. S. Wei, Z. Cheng, P. Nath, M. D. Tikekar, G. Li and L. A. Archer, *Sci. Adv.*, **2018**, *4*, eaao6243.
43. C.-Z. Zhao, X.-Q. Zhang, X.-B. Cheng, R. Zhang, R. Xu, P.-Y. Chen, H.-J. Peng, J.-Q. Huang and Q. Zhang, *Proc. Natl. Acad. Sci. USA*, **2017**, *114*, 11069-11074.
44. S. Chen, J. Zheng, D. Mei, K. S. Han, M. H. Engelhard, W. Zhao, W. Xu, J. Liu

- and J. G. Zhang, *Adv. Mater.*, **2018**, *30*, 1706102.
45. S. Chen, J. Zheng, L. Yu, X. Ren, M. H. Engelhard, C. Niu, H. Lee, W. Xu, J. Xiao and J. Liu, *Joule*, **2018**, *2*, 1-11.
 46. X. Fan, L. Chen, X. Ji, T. Deng, S. Hou, J. Chen, J. Zheng, F. Wang, J. Jiang and K. Xu, *Chem*, **2018**, *4*, 174-185.
 47. J. Qian, W. A. Henderson, W. Xu, P. Bhattacharya, M. Engelhard, O. Borodin and J.-G. Zhang, *Nat. Commun.*, **2015**, *6*, 6362.
 48. L. Suo, Y.-S. Hu, H. Li, M. Armand and L. Chen, *Nat. Commun.*, **2013**, *4*, 1481.
 49. L. Suo, W. Xue, M. Gobet, S. G. Greenbaum, C. Wang, Y. Chen, W. Yang, Y. Li and J. Li, *Proc. Natl. Acad. Sci. USA*, **2018**, 201712895.
 50. J. Wang, Y. Yamada, K. Sodeyama, C. H. Chiang, Y. Tateyama and A. Yamada, *Nat. Commun.*, **2016**, *7*, 12032.
 51. E. M. Erickson, E. Markevich, G. Salitra, D. Sharon, D. Hirshberg, E. de la Llave, I. Shterenberg, A. Rosenman, A. Frimer and D. Aurbach, *J. Electrochem. Soc.*, **2015**, *162*, A2424-A2438.
 52. M. S. Park, S. B. Ma, D. J. Lee, D. Im, S.-G. Doo and O. Yamamoto, *Sci. Rep.*, **2014**, *4*, 3815.
 53. I. A. Shkrob, T. W. Marin, Y. Zhu and D. P. Abraham, *J. Phys. Chem. C*, **2014**, *118*, 19661-19671.
 54. P. C. Andrikopoulos, D. R. Armstrong, D. V. Graham, E. Hevia, A. R. Kennedy, R. E. Mulvey, C. T. O'Hara and C. Talmard, *Angew. Chem. Int. Ed.*, **2005**, *117*, 3525-3528.
 55. R. Atkinson, S. M. Aschmann, J. Arey and W. P. Carter, *Int. J. Chem. Kinet.*, **1989**, *21*, 801-827.
 56. S. Scheiner, *Int. J. Quantum Chem.*, **2012**, *112*, 1879-1886.
 57. Y. Dong-Joo, K. K. Jae and C. J. Wook, *Adv. Energy Mater.*, **2018**, *8*, 1702744.
 58. H. Kim, F. Wu, J. T. Lee, N. Nitta, H. T. Lin, M. Oschatz, W. I. Cho, S. Kaskel, O. Borodin and G. Yushin, *Adv. Energy Mater.*, **2015**, *5*, 1401792.
 59. M. W. Schmidt, K. K. Baldridge, J. A. Boatz, S. T. Elbert, M. S. Gordon, J. H. Jensen, S. Koseki, N. Matsunaga, K. A. Nguyen and S. Su, *J. Comput. Chem.*, **1993**, *14*, 1347-1363.
 60. W. Xu, J. Wang, F. Ding, X. Chen, E. Nasybulin, Y. Zhang and J.-G. Zhang, *Energy Environ. Sci.*, **2014**, *7*, 513-537.
 61. J. W. Choi and D. Aurbach, *Nat. Rev. Mater.*, **2016**, *1*, 1-16.
 62. X. Sun, X. Zhang, Q. Ma, X. Guan, W. Wang and J. Luo, *Angew. Chem. Int. Ed.*, 2020, Accepted Author Manuscript. doi:10.1002/anie.201912217.
 63. J. Liu, Z. Bao, Y. Cui, E. J. Dufek, J. B. Goodenough, P. Khalifah, Q. Li, B. Y. Liaw, P. Liu and A. Manthiram, *Nat. Energy*, **2019**, *4*, 180-186.
 64. D. Lu, Y. Shao, T. Lozano, W. D. Bennett, G. L. Graff, B. Polzin, J. Zhang, M. H. Engelhard, N. T. Saenz, W. A. Henderson, P. Bhattacharya, J. Liu and J. Xiao, *Adv. Energy Mater.*, **2015**, *5*, 1400993.

65. M. Rosso, C. Brissot, A. Teyssot, M. Dollé, L. Sannier, J.-M. Tarascon, R. Bouchet and S. Lascaud, *Electrochim. Acta*, **2006**, *51*, 5334-5340.
66. X. Wang, M. Zhang, J. Alvarado, S. Wang, M. Sina, B. Lu, J. Bouwer, W. Xu, J. Xiao and J.-G. Zhang, *Nano Lett.*, **2017**, *17*, 7606-7612.
67. Y. Li, Y. Li, A. Pei, K. Yan, Y. Sun, C.-L. Wu, L.-M. Joubert, R. Chin, A. L. Koh and Y. Yu, *Science*, **2017**, *358*, 506-510.
68. Z. Yu, D. G. Mackanic, W. Michaels, M. Lee, A. Pei, D. Feng, Q. Zhang, Y. Tsao, C. V. Amanchukwu and X. Yan, *Joule*, **2019**, *3*, 2761-2776.
69. Y. Zhao, X. He, X. Liu, Q. Han, P. Zhang and X. Song, *Angew. Chem. Int. Ed.*, **2020**, *59*, 2-11.
70. Y.-T. Weng, H.-W. Liu, A. Pei, F. Shi, H. Wang, C.-Y. Lin, S.-S. Huang, L.-Y. Su, J.-P. Hsu and C.-C. Fang, *Nat. Commun.*, **2019**, *10*, 1-10.
71. G. Li, Z. Liu, D. Wang, X. He, S. Liu, Y. Gao, A. AlZahrani, S. H. Kim, L. Q. Chen and D. Wang, *Adv. Energy Mater.*, **2019**, *9*, 1900704.
72. D. J. Yoo, A. Elabd, S. Choi, Y. Cho, J. Kim, S. J. Lee, S. H. Choi, T. w. Kwon, K. Char and K. J. Kim, *Adv. Mater.*, **2019**, *31*, 1901645.
73. D. Lin, Y. Liu, Z. Liang, H.-W. Lee, J. Sun, H. Wang, K. Yan, J. Xie and Y. Cui, *Nat. Nanotechnol.*, **2016**, *11*, 626-632.
74. M. Wan, S. Kang, L. Wang, H.-W. Lee, G. W. Zheng, Y. Cui and Y. Sun, *Nat. Commun.*, **2020**, *11*, 1-10.
75. K. Lin, X. Qin, M. Liu, X. Xu, G. Liang, J. Wu, F. Kang, G. Chen and B. Li, *Adv. Funct. Mater.*, **2019**, *29*, 1903229.
76. H. Zhao, D. Lei, Y.-B. He, Y. Yuan, Q. Yun, B. Ni, W. Lv, B. Li, Q.-H. Yang, F. Kang and J. Lu, *Adv. Energy Mater.*, **2018**, *8*, 1800266.
77. C. Yan, Y. X. Yao, X. Chen, X. B. Cheng, X. Q. Zhang, J. Q. Huang and Q. Zhang, *Angew. Chem. Int. Ed.*, **2018**, *57*, 14055-14059.
78. D. J. Yoo, K. J. Kim and J. W. Choi, *Adv. Energy Mater.*, **2018**, *8*, 1702744.
79. D. J. Yoo, S. Yang, Y. S. Yun, J. H. Choi, D. Yoo, K. J. Kim and J. W. Choi, *Adv. Energy Mater.*, **2018**, *8*, 1802365.
80. J. Duan, W. Wu, A. M. Nolan, T. Wang, J. Wen, C. Hu, Y. Mo, W. Luo and Y. Huang, *Adv. Mater.*, **2019**, *31*, 1807243.
81. A. Li, X. Liao, H. Zhang, L. Shi, P. Wang, Q. Cheng, J. Borovilas, Z. Li, W. Huang and Z. Fu, *Adv. Mater.*, **2020**, *32*, 1905517.
82. N. Wu, Y. R. Shi, S. Y. Lang, J. M. Zhou, J. Y. Liang, W. Wang, S. J. Tan, Y. X. Yin, R. Wen and Y. G. Guo, *Angew. Chem. Int. Ed.*, **2019**, *58*, 18146-18149.
83. Z. Jiang, S. Wang, X. Chen, W. Yang, X. Yao, X. Hu, Q. Han and H. Wang, *Adv. Mater.*, **2020**, *32*, 1906221.
84. N. von Aspern, G. V. Röschenthaler, M. Winter and I. Cekic-Laskovic, *Angew. Chem. Int. Ed.*, **2019**, *58*, 15978-16000.
85. M. He, R. Guo, G. M. Hobold, H. Gao and B. M. Gallant, *Proc. Natl. Acad. Sci. USA*, **2020**, *117*, 73-79.

86. X. Zhang, S. Jiao, J. Tu, W.-L. Song, X. Xiao, S. Li, M. Wang, H. Lei, D. Tian, H. Chen and D. Fang, *Energy Environ. Sci.*, **2019**, *12*, 1918-1927.
87. X. Q. Zhang, T. Li, B. Q. Li, R. Zhang, P. Shi, C. Yan, J. Q. Huang and Q. Zhang, *Angew. Chem. Int. Ed.*, **2020**.
88. Y. Li, W. Huang, Y. Li, A. Pei, D. T. Boyle and Y. Cui, *Joule*, **2018**, *2*, 2167-2177.
89. S. Jiao, X. Ren, R. Cao, M. H. Engelhard, Y. Liu, D. Hu, D. Mei, J. Zheng, W. Zhao and Q. Li, *Nat. Energy*, **2018**, *3*, 739-746.
90. X. Ren, S. Chen, H. Lee, D. Mei, M. H. Engelhard, S. D. Burton, W. Zhao, J. Zheng, Q. Li and M. S. Ding, *Chem*, **2018**, *4*, 1877-1892.
91. X. Cao, X. Ren, L. Zou, M. H. Engelhard, W. Huang, H. Wang, B. E. Matthews, H. Lee, C. Niu and B. W. Arey, *Nat. Energy*, **2019**, *4*, 796-805.
92. Y. Zheng, F. A. Soto, V. Ponce, J. M. Seminario, X. Cao, J.-G. Zhang and P. B. Balbuena, *J. Mater. Chem. A*, **2019**, *7*, 25047-25055.
93. L. Yu, S. Chen, H. Lee, L. Zhang, M. H. Engelhard, Q. Li, S. Jiao, J. Liu, W. Xu and J.-G. Zhang, *ACS Energy Lett.*, **2018**, *3*, 2059-2067.
94. P. L. Coe, A. J. Waring and T. D. Yarwood, *J. Chem. Soc. Perkin Trans. 1*, **1995**, DOI: 10.1039/P19950002729, 2729-2737.
95. S. H. Kim, C. H. Kim, W. J. Choi, T. G. Lee, S. K. Cho, Y. S. Yang, J. H. Lee and S.-J. Lee, *Sci. Rep.*, **2017**, *7*, 1-10.
96. P. Gong, J. Wang, W. Sun, D. Wu, Z. Wang, Z. Fan, H. Wang, X. Han and S. Yang, *Nanoscale*, **2014**, *6*, 3316-3324.
97. L. Cheng, S. Jandhyala, G. Mordi, A. T. Lucero, J. Huang, A. Azcatl, R. Addou, R. M. Wallace, L. Colombo and J. Kim, *ACS Appl. Mater. Interfaces*, **2016**, *8*, 5002-5008.
98. J. M. Mallan and R. L. Bebb, *Chem. Rev.*, **1969**, *69*, 693-755.
99. D. J. Ramón and M. Yus, *Eur. J. Org. Chem.*, **2000**, *2000*, 225-237.
100. K. Kimura, J. Motomatsu and Y. Tominaga, *J. Phys. Chem. C*, **2016**, *120*, 12385-12391.
101. J. Wang, Y. Yamada, K. Sodeyama, C. H. Chiang, Y. Tateyama and A. Yamada, *Nat. Commun.*, **2016**, *7*, 1-9.
102. P. Shi, H. Zheng, X. Liang, Y. Sun, S. Cheng, C. Chen and H. Xiang, *Chem. Commun.*, **2018**, *54*, 4453-4456.
103. J. Alvarado, M. A. Schroeder, T. P. Pollard, X. Wang, J. Z. Lee, M. Zhang, T. Wynn, M. Ding, O. Borodin and Y. S. Meng, *Energy Environ. Sci.*, **2019**, *12*, 780-794.
104. J. Zheng, M. H. Engelhard, D. Mei, S. Jiao, B. J. Polzin, J.-G. Zhang and W. Xu, *Nat. Energy*, **2017**, *2*, 1-8.
105. X. Shangguan, G. Jia, F. Li, Q. Wang and B. Bai, *J. Electrochem. Soc.*, **2016**, *163*, A2797-A2802.
106. W. Kohn and L. J. Sham, *Phys. Rev.*, **1965**, *140*, A1133-A1138.

107. S. Chu, Y. Cui and N. Liu, *Nat. Mater.*, **2017**, *16*, 16-22.
108. J. M. Tarascon and M. Armand, *Nature*, **2001**, *414*, 359-367.
109. J. B. Goodenough and K.-S. Park, *J. Am. Chem. Soc.*, **2013**, *135*, 1167-1176.
110. M. Armand and J. M. Tarascon, *Nature*, **2008**, *451*, 652-657.
111. P. Canepa, G. Sai Gautam, D. C. Hannah, R. Malik, M. Liu, K. G. Gallagher, K. A. Persson and G. Ceder, *Chem. Rev.*, **2017**, *117*, 4287-4341.
112. D.-J. Yoo, J.-S. Kim, J. Shin, K. J. Kim and J. W. Choi, *ChemElectroChem*, **2017**, *4*, 2345-2351.
113. S. Dagorne and D. A. Atwood, *Chem. Rev.*, **2008**, *108*, 4037-4071.
114. D. A. Atwood, *Coord. Chem. Rev.*, **1998**, *176*, 407-430.
115. R. M. Buchanan and C. G. Pierpont, *J. Am. Chem. Soc.*, **1980**, *102*, 4951-4957.
116. N. G. Connelly and W. E. Geiger, *Chem. Rev.*, **1996**, *96*, 877-910.
117. E. S. Klimov, A. V. Lobanov and G. A. Abakumov, *Russ. Chem. Bull.*, **1981**, *30*, 1664-1666.
118. P. E. Barker, A. Hudson and R. A. Jackson, *J. Organomet. Chem.*, **1981**, *208*, C1-C2.
119. D. Aurbach, Z. Lu, A. Schechter, Y. Gofer, H. Gizbar, R. Turgeman, Y. Cohen, M. Moshkovich and E. Levi, *Nature*, **2000**, *407*, 724-727.
120. N. S. Hudak, *J. Phys. Chem. C*, **2014**, *118*, 5203-5215.
121. N. Jayaprakash, S. K. Das and L. A. Archer, *Chem. Commun.*, **2011**, *47*, 12610-12612.
122. J. Zhang, X. Wang, Q. Su, L. Zhi, A. Thomas, X. Feng, D. S. Su, R. Schlögl and K. Müllen, *J. Am. Chem. Soc.*, **2009**, *131*, 11296-11297.
123. L. Tang, Y. Wang, Y. Li, H. Feng, J. Lu and J. Li, *Adv. Funct. Mater.*, **2009**, *19*, 2782-2789.
124. A. K. Geim and K. S. Novoselov, *Nat. Mater.*, **2007**, *6*, 183-191.
125. M. G. Schwab, M. Takase, A. Mavrinsky, W. Pisula, X. Feng, J. A. Gámez, W. Thiel, K. S. Mali, S. de Feyter and K. Müllen, *Chem. Eur. J.*, **2015**, *21*, 8426-8434.
126. S. Wang, K. V. Kravchyk, A. N. Filippin, U. Müller, A. N. Tiwari, S. Buecheler, M. I. Bodnarchuk and M. V. Kovalenko, *Adv. Sci.*, **2018**, *5*, 1700712.
127. F. M. Hassan, R. Batmaz, J. Li, X. Wang, X. Xiao, A. Yu and Z. Chen, *Nat. Commun.*, **2015**, *6*, 8597.
128. W. Kaim, *Acc. Chem. Res.*, **1985**, *18*, 160-166.
129. G. Van Koten, J. T. B. H. Jastrzebski and K. Vrieze, *J. Organomet. Chem.*, **1983**, *250*, 49-61.
130. G. A. Razuvaev, G. A. Abakumov, E. S. Klimov, E. N. Gladyshev and P. Y. Bayushkin, *Russ. Chem. Bull.*, **1977**, *26*, 1034-1037.
131. K. V. Kravchyk, S. Wang, L. Piveteau and M. V. Kovalenko, *Chem. Mater.*, **2017**, *29*, 4484-4492.
132. D. J. Kim, K. R. Hermann, A. Prokofjevs, M. T. Otley, C. Pezzato, M. Owczarek

- and J. F. Stoddart, *J. Am. Chem. Soc.*, **2017**, *139*, 6635-6643.
133. M. Armand, S. Grugeon, H. Vezin, S. Laruelle, P. Ribière, P. Poizot and J. M. Tarascon, *Nat. Mater.*, **2009**, *8*, 120-125.
 134. Y. Morita, S. Nishida, T. Murata, M. Moriguchi, A. Ueda, M. Satoh, K. Arifuku, K. Sato and T. Takui, *Nat. Mater.*, **2011**, *10*, 947-951.
 135. M. Lee, J. Hong, H. Kim, H.-D. Lim, S. B. Cho, K. Kang and C. B. Park, *Adv. Mater.*, **2014**, *26*, 2558-2565.
 136. Y. Liang, Z. Tao and J. Chen, *Adv. Energy Mater.*, **2012**, *2*, 742-769.
 137. Z. Zhang, H. Yoshikawa and K. Awaga, *Chem. Mater.*, **2016**, *28*, 1298-1303.
 138. C. Fang, Y. Huang, L. Yuan, Y. Liu, W. Chen, Y. Huang, K. Chen, J. Han, Q. Liu and Y. Huang, *Angew. Chem. Int. Ed.*, **2017**, *56*, 6793-6797.
 139. D.-Y. Wang, C.-Y. Wei, M.-C. Lin, C.-J. Pan, H.-L. Chou, H.-A. Chen, M. Gong, Y. Wu, C. Yuan, M. Angell, Y.-J. Hsieh, Y.-H. Chen, C.-Y. Wen, C.-W. Chen, B.-J. Hwang, C.-C. Chen and H. Dai, *Nat. Commun.*, **2017**, *8*, 14283.
 140. C. Chen, Y. Zhang, Y. Li, Y. Kuang, J. Song, W. Luo, Y. Wang, Y. Yao, G. Pastel, J. Xie and L. Hu, *Adv. Energy Mater.*, **2017**, *7*, 1700595.
 141. J. H. Lee, N. Park, B. G. Kim, D. S. Jung, K. Im, J. Hur and J. W. Choi, *ACS Nano*, **2013**, *7*, 9366-9374.
 142. K.-H. Wu, D.-W. Wang and I. R. Gentle, *Carbon*, **2014**, *73*, 234-243.
 143. G. A. Elia, K. Marquardt, K. Hoepfner, S. Fantini, R. Lin, E. Knipping, W. Peters, J. F. Drillet, S. Passerini and R. Hahn, *Adv. Mater.*, **2016**, *28*, 7564-7579.
 144. J. Deng, C. Bae, J. Marcicki, A. Masias and T. Miller, *Nat. Energy*, **2018**, *3*, 261.
 145. M. Armand, F. Endres, D. R. MacFarlane, H. Ohno and B. Scrosati, *Nat. Mater.*, **2009**, *8*, 621-629.
 146. Q. Li and N. J. Bjerrum, *J. Power Sources*, **2002**, *110*, 1-10.
 147. F. Ambroz, T. J. Macdonald and T. Nann, *Adv. Energy Mater.*, **2017**, *7*, 1602093.
 148. X. Wen, Y. Liu, A. Jadhav, J. Zhang, D. Borchardt, J. Shi, B. M. Wong, B. Sanyal, R. J. Messinger and J. Guo, *Chem. Mater.*, **2019**, *31*, 7238-7247.
 149. H. Chen, F. Guo, Y. Liu, T. Huang, B. Zheng, N. Ananth, Z. Xu, W. Gao and C. Gao, *Adv. Mater.*, **2017**, *29*, 1605958.
 150. Y. Wu, M. Gong, M. C. Lin, C. Yuan, M. Angell, L. Huang, D. Y. Wang, X. Zhang, J. Yang and B. J. Hwang, *Adv. Mater.*, **2016**, *28*, 9218-9222.
 151. D.-Y. Wang, C.-Y. Wei, M.-C. Lin, C.-J. Pan, H.-L. Chou, H.-A. Chen, M. Gong, Y. Wu, C. Yuan and M. Angell, *Nat. Commun.*, **2017**, *8*, 14283.
 152. M.-C. Lin, M. Gong, B. Lu, Y. Wu, D.-Y. Wang, M. Guan, M. Angell, C. Chen, J. Yang, B.-J. Hwang and H. Dai, *Nature*, **2015**, *520*, 324.
 153. M. Chiku, H. Takeda, S. Matsumura, E. Higuchi and H. Inoue, *ACS Appl. Mater. Interfaces*, **2015**, *7*, 24385-24389.
 154. N. Jayaprakash, S. Das and L. Archer, *Chem. Commun.*, **2011**, *47*, 12610-12612.
 155. X. Zhang, G. Zhang, S. Wang, S. Li and S. Jiao, *J. Mater. Chem. A*, **2018**, *6*, 3084-3090.

156. C. Wu, S. Gu, Q. Zhang, Y. Bai, M. Li, Y. Yuan, H. Wang, X. Liu, Y. Yuan and N. Zhu, *Nat. Commun.*, **2019**, *10*, 73.
157. T. Koketsu, J. Ma, B. J. Morgan, M. Body, C. Legein, W. Dachraoui, M. Giannini, A. Demortière, M. Salanne and F. Dardoize, *Nat. Mater.*, **2017**, *16*, 1142.
158. S. Wang, S. Jiao, J. Wang, H.-S. Chen, D. Tian, H. Lei and D.-N. Fang, *ACS Nano*, **2017**, *11*, 469-477.
159. Y. Hu, D. Ye, B. Luo, H. Hu, X. Zhu, S. Wang, L. Li, S. Peng and L. Wang, *Adv. Mater.*, **2018**, *30*, 1703824.
160. L. Geng, J. P. Scheifers, J. Zhang, K. N. Bozhilov, B. P. Fokwa and J. Guo, *Chem. Mater.*, **2018**, *30*, 8420-8425.
161. H. Li, H. Yang, Z. Sun, Y. Shi, H.-M. Cheng and F. Li, *Nano Energy*, **2019**, *56*, 100-108.
162. Y. Hu, B. Luo, D. Ye, X. Zhu, M. Lyu and L. Wang, *Adv. Mater.*, **2017**, *29*, 1606132.
163. X. Yu and A. Manthiram, *Adv. Energy Mater.*, **2017**, *7*, 1700561.
164. H. Yang, L. Yin, J. Liang, Z. Sun, Y. Wang, H. Li, K. He, L. Ma, Z. Peng, S. Qiu, C. Sun, H.-M. Cheng and F. Li, *Angew. Chem. Int. Ed.*, **2018**, *57*, 1898-1902.
165. C. Ferrara, V. Dall'Asta, V. Berbenni, E. Quartarone and P. Mustarelli, *J. Phys. Chem. C*, **2017**, *121*, 26607-26614.
166. D. J. Kim, D.-J. Yoo, M. T. Otley, A. Prokofjevs, C. Pezzato, M. Owczarek, S. J. Lee, J. W. Choi and J. F. Stoddart, *Nat. Energy*, **2019**, *4*, 51.
167. Z. Li, Z. Jian, X. Wang, I. A. Rodríguez-Pérez, C. Bommier and X. Ji, *Chem. Commun.*, **2017**, *53*, 2610-2613.
168. M.-S. Kwon, A. Choi, Y. Park, J. Y. Cheon, H. Kang, Y. N. Jo, Y.-J. Kim, S. Y. Hong, S. H. Joo and C. Yang, *Sci. Rep.*, **2014**, *4*, 7404.
169. K. Zhang, C. Guo, Q. Zhao, Z. Niu and J. Chen, *Adv. Sci.*, **2015**, *2*, 1500018.
170. Z. Song, Y. Qian, M. L. Gordin, D. Tang, T. Xu, M. Otani, H. Zhan, H. Zhou and D. Wang, *Angew. Chem. Int. Ed.*, **2015**, *54*, 13947-13951.
171. Z. Song, Y. Qian, X. Liu, T. Zhang, Y. Zhu, H. Yu, M. Otani and H. Zhou, *Energy Environ. Sci.*, **2014**, *7*, 4077-4086.
172. Y. Liang, Y. Jing, S. Gheyhani, K.-Y. Lee, P. Liu, A. Facchetti and Y. Yao, *Nat. Mater.*, **2017**, *16*, 841.
173. M. Galiński, A. Lewandowski and I. Stępnia, *Electrochim. Acta*, **2006**, *51*, 5567-5580.
174. J. Wang, J. Polleux, J. Lim and B. Dunn, *J. Phys. Chem. C*, **2007**, *111*, 14925-14931.
175. K. Li, J. Zhang, D. Lin, D.-W. Wang, B. Li, W. Lv, S. Sun, Y.-B. He, F. Kang, Q.-H. Yang, L. Zhou and T.-Y. Zhang, *Nat. Commun.*, **2019**, *10*, 725.
176. Y. Wang, S. Nakamura, M. Ue and P. B. Balbuena, *J. Am. Chem. Soc.*, **2001**,

123, 11708-11718.

177. M. L. Agiorgousis, Y.-Y. Sun and S. Zhang, *ACS Energy Lett.*, **2017**, 2, 689-693.
178. C. Zhang, Y. Ding, L. Zhang, X. Wang, Y. Zhao, X. Zhang and G. Yu, *Angew. Chem. Int. Ed.*, **2017**, 56, 7454-7459.
179. M. R. Busche, T. Drossel, T. Leichtweiss, D. A. Weber, M. Falk, M. Schneider, M.-L. Reich, H. Sommer, P. Adelhelm and J. Janek, *Nat. Chem.*, **2016**, 8, 426-434.

국문 초록

리튬 산화물 양극 및 흑연 음극으로 구성된 리튬 이온 전지는 높은 에너지 밀도를 보유하여 대부분의 이동식 전자기기의 에너지 저장 장치로 사용되고 있다. 하지만, 리튬 이온 전지의 상용화 이후 드론 및 전기차와 같은 이동식 전자기기의 상용화에 따라, 사용 시간과 주행 거리를 늘리기 위해 더 높은 에너지 밀도를 보유하는 전지 개발에 대한 요구가 높아지고 있다. 산업계인 이차 전지 공급사들의 수십년 간 노력으로 리튬 이온 전지의 실제적인 에너지 밀도는 활물질이 지니는 이론적인 수치에 다다르고 있는 실정이다.

에너지 밀도의 급격한 상승을 위해서는 기존의 삽/탈리 메커니즘을 벗어나 새로운 산화/환원 화학 반응을 필요로 한다. 이러한 산화/환원 반응은 기존 반응 물질과 다른 거동을 보이며, 특히 제어가 어려운 부반응과 짧은 수명 특성을 동반하게 된다. 낮은 가역성을 보이는 주요 인자는 전극/전해질 계면에서의 불안정성이다. 이는 전극 물질이 에너지를 저장하는 동안 전해질과의 계면에서 끊임없이 부반응을 일으키고 있음을 의미하며, 이를 제어하기 위한 연구들이 지속되어 왔다. 본 학위 논문에서는 리튬 금속 전지와 알루미늄 전지를 위한 새로운 유기 물질의 개발과 분석 원리에 대해 다루고자 한다.

제 2장에서는 리튬 금속 음극 계면에서 카보네이트 기반 전해질 내에서 톨루엔의 역할을 규명하였다. 톨루엔의 메틸 그룹은 벤젠링 내에 전자를 제공하여 환원 포텐셜을 앞당기는 역할을 한다. 이는 기존에 사용되는 카보네이트 용매보다 환원 포텐셜이 낮아, 전해질 내에서 톨루엔이 먼저 환원되어 균일한 전극/전해질 계면을 형성할 수 있다. 더욱이, 톨루엔의 환원-고분자 과정에서 생성되는 라디칼은 염에 포함된 음이온의 분해를 가속화하여, 수지상 성장을 억제하는 플루오린화 리튬 (lithium fluoride, LiF)의 균일한 분포를 가능하게 한다. 본 연구는 안정적인 전극/전해질 계면 형성에서의 방향족 용매의 활용 가능성을 제시하였으며, 특히 방향족 용매의 벤

젠링에 전자를 제공하는 작용기가 환원 포텐셜을 조절할 수 있음을 밝혔다.

제 3장에서는 고농도 전해질 효과를 가능하게 하는 불소화 방향족 용매에 대해 다루고 있다. 국소적 고농도 효과는 음이온의 분해를 가속화하여, 리튬 금속 계면을 안정화하는 효과를 지니고 있다. 본 연구에서 제안된 불소화 방향족 용매는 리튬 이온과의 결합력이 낮아, 공용매로 사용될 시에 국지적 고농도 효과를 부여할 수 있는 특징이 있다. 더욱이, 특정 불소화 방향족 용매 (1,2-difluorobenzene)는 리튬 금속과 접촉 시 화학 반응을 통한 LiF를 형성하는 특성을 보유하여, 리튬 금속 전지의 성능을 대폭 향상시킬 수 있었다. 본 연구는 리튬 금속 음극을 제어하기 위한 국지적 고농도 전해질 개발의 디자인 원리를 제시한다.

제 4장에서는 알루미늄 전지 용 양극 활물질 개발을 다루고 있다. 3가의 알루미늄 이온은 전통적인 산화물, 황화물-기반 물질의 구조를 무너뜨려 낮은 가역성을 가지는 문제를 보유한다. 이를 해결하기 위해서, 알루미늄 착이온이 가역적으로 산화/환원하는 유기 분자 구조를 규명하고, 나아가 삼각형의 매크로사이클 분자를 디자인하여 고체 상태에서의 가역성을 극대화하였다. 또한, 유기 분자의 내재적 문제점인 낮은 전자전도성을 판상형 흑연과의 복합화를 통하여 높은 로딩의 전극에서의 고성능을 달성하였다. 본 연구는 알루미늄 전지 양극으로 사용될 수 있는 유기 분자의 작용기 및 구조 디자인의 원리를 제시한다.

제 5장에서는 알루미늄 착이온이 가역적으로 반응하는 특정 유기 분자 (phenanthrenequinone, PQ)의 우수한 전기화학 특성의 원인을 밝히고 있다. PQ 분자는 리튬 이온과 반응할 시 열역학적으로 불안정한 거동을 보여주며 낮은 가역성을 가지는 반면, 알루미늄 착이온과 반응할 시 연이은 카르보닐 작용기와 착이온의 강한 결합력을 통하여 안정적인 거동을 하는 것을 확인하였다. 환원된 PQ-AlCl₃ 복합체에서 알루미늄 원자는 음전하를 띤 작용기에 둘러싸여 있어 낮은 유효 전하를 가지는 것으로 나타났다. 또한, 리튬 전해질과 비교하여 알루미늄 전해질에서 알루미늄 착이온을 생성하는 반응이 상대적 높은 키네틱을 보유하여 우수한 전기화학 유효성을 보여주

었다. 본 연구는 알루미늄 착이온의 배위 환경에 따른 안정성 및 이온 생성의 키네틱이 전기화학적 성능을 결정하는 것을 밝혔다.

주요어: 유기 소재, 차세대 이차 전지, 전해질, 리튬 금속 전지, 알루미늄 전지

학번: 2018-38876

List of publications

International Publications

International Peer-Reviewed Journals (First Author)

1. **D.-J. Yoo**, S. Yang, K. J. Kim*, J. W. Choi*, “Fluorinated Aromatic Diluent for High-Performance Lithium Metal Batteries”, *Angew. Chem. Int. Ed.*, just accepted
2. S. Eder†, **D.-J. Yoo**†, W. Nogala, M. Pletzer, A. S. Bonilla, A. White, K. Jelfs, M. Heeney, J. W. Choi*, F. Glocklhofer*, “Switching between local and global aromaticity in a conjugated macrocycle enables high-performance organic sodium-ion battery anodes”, *Angew. Chem. Int. Ed.*, 2020, 59, 2-9
3. **D.-J. Yoo**, J. W. Choi*, “Elucidating the Extraordinary Rate and Cycling Performance of Phenanthrenequinone in Aluminum Complex-Ion Batteries”, *J. Phys. Chem. Lett.*, 2020, 11, 2384-2392
4. **D.-J. Yoo**†, A. Elabd†, S. Choi†, Y. Cho, J. Kim, S. J. Lee, S. H. Choi, T.-w. Kwon, K. Char, K. J. Kim*, A. Coskun*, J. W. Choi*, “Highly Elastic Polyrotaxane Binders for Mechanically Stable Lithium Hosts in Lithium Metal Batteries”, *Adv. Mater.*, 2019, 190164
5. D. J. Kim†, **D.-J. Yoo**†, M. T. Otley, A. Prokofjevs, C. Pezzato, M. Owczarek, S. J. Lee, J. W. Choi*, J. F. Stoddart*, “Rechargeable Aluminium Organic Batteries”, *Nat. Energy*, 2019, 4, 51-59
6. **D.-J. Yoo**†, S. Yang†, Y. S. Yun, J. H. Choi, D. Yoo, K. J. Kim*, J. W. Choi*, “Tuning the Electron Density of Aromatic Solvent for Stable Solid-Electrolyte-Interphase Layer in Carbonate-based Lithium Metal Batteries”, *Adv. Energy Mater.*, 2018, 8, 1802365
7. **D.-J. Yoo**, K. J. Kim*, J. W. Choi*, “The Synergistic Effect of Cation and Anion of an Ionic Liquid Additive for Lithium Metal Anodes”, *Adv. Energy Mater.*, 2018, 8, 1702744
8. **D.-J. Yoo**†, J.-S. Kim†, J. Shin, K. J. Kim, J. W. Choi*, “Stable Performance of Aluminum Metal Battery by Incorporating Lithium Ion Chemistry”, *ChemElectroChem*, 2017, 4, 2345-2351

International Peer-Reviewed Journals (Co-author)

1. S. H. Choi†, S. J. Lee†, **D.-J. Yoo**, J. H. Park, J.-H Park, Y. N. Ko, J. Park, Y.-E. Sung, S.-Y. Chung*, H. Kim*, J. W. Choi*, “Marginal Magnesium Doping for High Performance Lithium Metal Batteries”, *Adv. Energy Mater.*, 2019, 1902278
2. B. Lee, J. Choi, S. Na, **D.-J. Yoo**, J. H. Kim, B. W. Cho, Y.-T. Kim, T. Yim*, J. W. Choi*, S. H. Oh*, “Critical role of elemental copper for enhancing conversion kinetics of sulphur cathodes in rechargeable magnesium batteries”, *Appl. Surf. Sci.*, 2019, 484, 933
3. S. C. Jung, Y.-J. Kang, **D.-J. Yoo**, J. W. Choi*, Y.-K. Han*, “Flexible Few-Layered Graphene for the Ultrafast Rechargeable Aluminum-Ion Battery”, *J. Phys. Chem. C*, 2016, 120, 13384-13389
4. J.-S. Kim, **D.-J. Yoo**, J. Min, R. A. Shakoor, R. Kahraman*, J. W. Choi*, “Poreless Separator and Electrolyte Additive for Lithium-Sulfur Batteries with High Areal Energy Densities”, *ChemNanoMat*, 2015, 1, 240-245
5. J.-S. Kim, D. Ko, **D.-J. Yoo**, D. S. Jung, C. T. Yavuz, N.-I. Kim, I.-S. Choi, J. Y. Song*, J. W. Choi*, “A Half Millimeter Thick Co-planar Flexible Battery with Wireless Recharging Capability”, *Nano Lett.*, 2015, 15, 2350-2357

Conferences Presentation

1. **D.-J. Yoo**, J. W. Choi*, “Highly Elastic Polyrotaxane Binders for Mechanically Stable Lithium Hosts in Lithium-Metal Batteries”, 2020. 01. 17. NCC (Nano Convergence Conference), Gangwon, Korea (poster)
2. **D.-J. Yoo**, J. W. Choi*, “Rechargeable Aluminium Organic Batteries”, 2019. 12. 3. MRS (Materials Research Society), Boston, USA (poster)
3. **D.-J. Yoo**, J. W. Choi*, “Highly Elastic Polyrotaxane Binders for Mechanically Stable Lithium Hosts in Lithium-Metal Batteries”, 2019. 10. 17. KCS (Korean Chemical Society), Changwon, Korea (poster)
4. **D.-J. Yoo**, J. W. Choi*, “Rechargeable Aluminium Organic Batteries”, 2019. 4. 17. KCS (Korean Chemical Society), Suwon, Korea (oral)
5. **D.-J. Yoo**, J. W. Choi*, “Tuning the Electron Density of Aromatic Solvent for Stable Solid-Electrolyte-Interphase Layer in Lithium Metal Batteries”, 2018. 10. 18. KCS (Korean Chemical Society), Daegu, Korea (oral)
6. **D.-J. Yoo**, J. W. Choi*, “The Synergistic Effect of Cation and Anion of an Ionic Liquid Additive for Lithium Metal Anodes”, 2018. 6. 20. IMLB (International Meeting on Lithium Batteries), Kyoto, Japan (Poster)
7. **D.-J. Yoo**, J. W. Choi*, “The Synergistic Effect of Cation and Anion of an Ionic Liquid Additive for Lithium Metal Anodes”, 2018. 4. 26. KICHE (Korean Institute of Chemical Engineers), Changwon, Korea (Poster)
8. **D.-J. Yoo**, J. W. Choi*, “The Synergistic Effect of Cation and Anion of an Ionic Liquid Additive for Lithium Metal Anodes”, 2018. 1. 11. NCC (Nano Convergence Conference), Seoul, Korea (Poster)
9. **D.-J. Yoo**, J. W. Choi*, “Stable Performance of Aluminum Metal Batteries by Incorporating Lithium Ion Chemistry”, 2017. 4. 21. KCS (Korean Chemical Society), Goyang, Korea (Poster)